

Development of an angular selective electron gun for the KATRIN main spectrometer

Daniel Winzen

Diploma Thesis

Institut für Kernphysik
Mathematisch-Naturwissenschaftliche Fakultät
Westfälische Wilhelms-Universität Münster

March 2014



Ich versichere, dass ich die Arbeit selbstständig verfasst und keine anderen als die angegebenen Quellen und Hilfsmittel benutzt, sowie Zitate kenntlich gemacht habe.

Referent: Prof. Dr. C. Weinheimer
Korreferent: Prof. Dr. A. Khoukaz

Contents

1	Introduction	5
2	Neutrino Physics	7
2.1	Introduction	7
2.2	Discovery of neutrinos	7
2.3	Evidence for neutrino mass	8
2.3.1	Neutrinos in the standard model of particle physics	8
2.3.2	The solar neutrino problem	8
2.3.3	Neutrino oscillation	9
2.4	Current neutrino mass experiments	12
3	The KATRIN experiment	17
3.1	The Mac-E filter principle	17
3.1.1	Working principle	17
3.1.2	Energy resolution	18
3.1.3	Transmission function	20
3.2	Setup	22
3.2.1	Rear section (RS)	22
3.2.2	Windowless gaseous tritium source (WGTS)	22
3.2.3	Transport section (DPS and CPS)	23
3.2.4	Pre-spectrometer (PS)	24
3.2.5	Main spectrometer (MS)	24
3.2.6	Monitor spectrometer (MoS)	25
3.2.7	Focal plane detector (FPD)	25
4	Electron source principles	27
4.1	Calibration source requirements	27
4.2	Working principle	29
4.2.1	Electron creation	29
4.2.2	Electron acceleration	30
4.2.3	Predecessor electron gun	32
5	Electron gun components	35
5.1	Light sources	35
5.2	Optical light guides	37
5.3	Cathode materials	39
5.3.1	Matching cathode materials	39

Contents

5.3.2	Work function of metals	41
5.4	Electron gun positioning	45
5.5	Electron gun assembly	48
6	Simulations	51
6.1	Simulation tools	51
6.2	Simulation results	52
7	Electron gun test measurements	57
7.1	Test setup	57
7.1.1	Principle	57
7.1.2	Hardware	58
7.2	Test measurements with front illuminated cathode	60
7.2.1	Electron spectra	61
7.2.2	Electron rate measurements	62
7.2.3	Work function measurements	64
7.2.4	Transmission function measurements	68
7.2.5	Stray light issues and conclusion	70
7.3	Test measurements with back illuminated silver substrate	73
7.3.1	Electron rate measurements	73
7.3.2	Work function measurements	75
7.3.3	Transmission function measurements	79
7.3.4	Conclusion	79
8	Summary	81

1 Introduction

Since Wolfgang Pauli postulated the existence of the neutrino in 1930, it has been one of the most investigated particles in particle physics [Pau30]. After the first direct detection in 1956 there still were many open questions left about the nature of the neutrino. One major aspect up to nowadays is the exact mass value of the neutrino. It has already been proven that the mass is not zero by observing neutrino oscillations in 1998 [Kam]. Despite discovering upper mass level limits¹ of $2.3 \text{ eV}/c^2$ and $2.05 \text{ eV}/c^2$ at 95% confidence level for the electron anti-neutrino mass, the exact value will play an important role in cosmology and particle physics.

The **K**ARlsruhe **T**RItium **N**eutrino Experiment (KATRIN) aims to determine the electron anti-neutrino mass by measuring the endpoint region of the tritium beta decay. In conclusion KATRIN will either measure a neutrino mass larger than $0.35 \text{ eV}/c^2$ ($0.30 \text{ eV}/c^2$) with 5σ (3σ) significance or set a new upper limit of $0.2 \text{ eV}/c^2$ with a 90% confidence level. For such a precision measurement a high resolution spectrometer (MAC-E filter) is needed in order to analyze the β -electrons. The precision of the electric and magnetic fields inside the MAC-E filter is a crucial factor to reach the aimed sensitivity. Thus a calibration source is needed to secure the precision of the electromagnetic fields inside the filter. This thesis will focus on the hardware development of an angular selective electron gun, which is supposed to operate as such a source. [KAT04]

This thesis will have the following structure:

- Chapter 2 will give a short overview about neutrino physics and its current mass research state. It will also give further insight into the challenges that are related with neutrino research in general.
- In Chapter 3 the KATRIN experiment will be explained, beginning with the theoretical concept of the MAC-E filter technology. The MAC-E filter will be explained in detail considering its significance for understanding the need for a calibration source and its requirements. The second part of the chapter will be about the hardware setup of the KATRIN experiment.
- Chapter 4 will be about the requirements a calibration source for the main spectrometer has to fulfill and the working principle that is used for the electron. The chapter will conclude with the previously developed prototype electron gun, which already proved the working principle of the electron gun introduced in this thesis.

¹Results by the Mainz and Troitsk neutrino mass experiments.

1 Introduction

- In chapter 5 the hardware components that are used for the electron gun setup and the hardware realization of the electron gun will be described.
- Chapter 6 focuses on the simulations conducted in the design process of the electron gun. The simulation tools necessary for obtaining the specifications of the electron gun will also shortly be introduced.
- In Chapter 7 the test measurements in Münster with two evolutions of the electron gun will be presented. The chapter will conclude with the final properties of the electron gun.
- Chapter 8 will summarize the results of this thesis and give a short outlook on the status and the future of the electron gun project in the KATRIN experiment.

2 Neutrino Physics

2.1 Introduction

Nowadays neutrinos play a large role in several disciplines of physics. They are for example used as probes to observe supernovae, processes in the sun or possibly the core of the milky way via neutrino telescopes. This is possible because of the elusive nature of the neutrinos. Participating only in the weak and gravitational interactions, their cross section is very small, when it comes to interacting with matter. Where other radiation can hardly pass through dense matter, neutrinos can pass with very few interactions. On the other hand this fact makes them very difficult to detect.

This chapter shall give insight into the research history of the neutrino and the current state of neutrino physics.

2.2 Discovery of neutrinos

Wolfgang Pauli postulated the neutrino in order to explain the results of β -decay measurements at that time. The continuous spectrum of the β -decay was fundamentally different to the line spectra of α - and γ -decays that were already well understood at that time. By introducing a new particle to the decay, the continuity of the spectrum could be explained through a three-body decay.

The theoretical basis of the β -decay was published in 1934 by Enrico Fermi [Fer34]. In his paper he also gave the neutrino its name, since Pauli's originally proposed name "neutron" had already been used for another particle in the mean time. Despite having a theoretical understanding of the β -decay and the knowledge that there must be a particle such as the neutrino, it still needed 22 more years to gain experimental evidence for the neutrino. This fact already gives a hint of why it is so complicated to measure neutrinos and their properties: The very low cross-section is the main obstacle when trying to detect neutrinos.

Frederick Reines¹ and Clyde L. Cowan solved the problem by using the Savannah River Reactor as a high flux neutrino source ($5 \cdot 10^{13}$ neutrinos per second) [Rei59]. To detect the neutrinos two tanks containing water and cadmium chloride were sandwiched between three scintillator layers which contained 127 mm photomultiplier tubes. The tanks were shielded from cosmic rays by placing them in 12 m underground about 11 m from

¹Frederick Reines was honored with the Nobel Prize in 1995 for the discovery of the neutrino

2 Neutrino Physics

the reactor core itself. Incoming electron anti-neutrinos interacted with the protons of the water thus creating neutrons and positrons.



The positrons then annihilated with electrons creating gamma rays, which were detected with the scintillation detectors.

The cadmium chloride was placed in the tank in order to reach a higher certainty for the results. Cadmium is a highly effective neutron absorber and was used to detect the neutrons created in the neutrino capture process by the following reaction:



The gamma ray from the cadmium would be detected approximately $5 \mu\text{s}$ after the gamma rays from the positron annihilation process.

It took several month to accumulate enough data to announce the discovery. To show that indeed neutrinos from the reactor have been measured, the down time of the reactor was used to measure the difference in the number of events.

2.3 Evidence for neutrino mass

2.3.1 Neutrinos in the standard model of particle physics

For decades, after discovering the neutrino, the mass of the particle was assumed to be zero. This assumption was also consistent with the standard model of particle physics as it contains no mechanism to give mass to the neutrinos if the fermion number is conserved [Rab97]. The standard model features three generations of fermions in the first three columns, the force carriers (gauge bosons) in the 4th column and the Higgs boson in the fifth column (fig. 2.1).

The leptons are grouped into three doublets with three different flavors of neutrinos ν_e , ν_μ and ν_τ named after their partner leptons. All neutrinos carry an electrical charge of zero, hence they do not interact in electromagnetic interactions. Being leptons neutrinos also do not interact via the strong interaction. This leaves the weak interaction and gravity, leading to the very low cross section in interactions with matter.

2.3.2 The solar neutrino problem

In the late 1960s the Homestake experiment was the first to measure neutrinos originating in the sun. These solar neutrinos are produced in the following net fusion reaction [Zub04]:

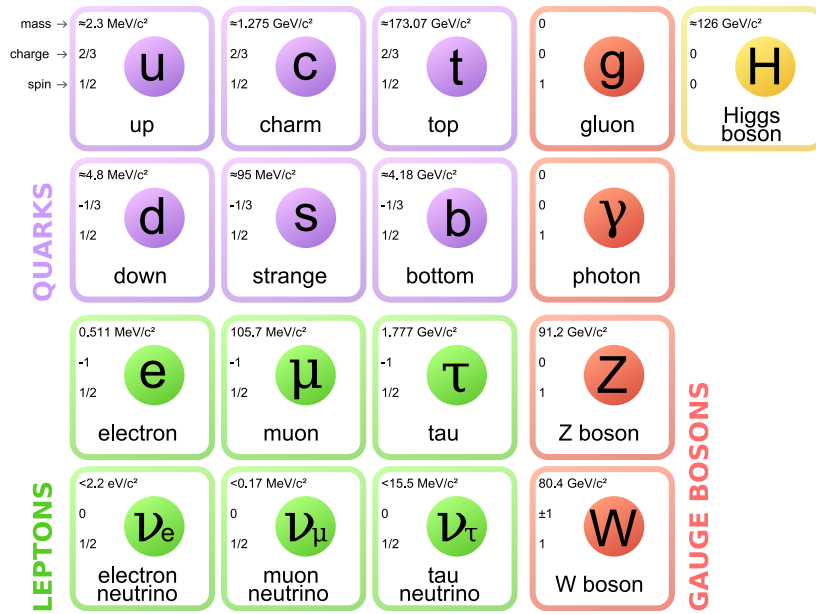
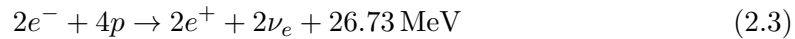


Figure 2.1: The standard model of particle physics. [Wik]



The goal was to measure a solar neutrino flux consistent with theoretical calculations conducted by John N. Bahcall. The experiment itself took place in an abandoned gold mine near Lead, South Dakota. In 1478 meters underground a tank of 380 cubic meters perchloroethylene (C_2Cl_4) was placed. Upon the collision between a neutrino and a chlorine atom, the chloride atom is transformed into argon:



By detecting the amount of created argon atoms, the neutrino capture rate could be deduced.

In conclusion only 1/3 of the predicted neutrino flux could be measured. This discrepancy became known as the solar neutrino problem. The Homestake experiment then led to many confirmation experiments (e.g. Gallex, SAGE, Kamiokande and Super-Kamiokande) that could indeed confirm the result.

2.3.3 Neutrino oscillation

A solution to the solar neutrino problem was later given through the theory of neutrino oscillation. This means that a neutrino has a probability to periodically change its flavor while moving. The basic assumption of this concept is that, in contradiction to

2 Neutrino Physics

the standard model, neutrinos have mass eigenstates ν_i ($i = 1, 2, 3$) and therefore mass. These eigenstates are not identical to the flavor eigenstates ν_α ($\alpha = e, \mu, \tau$).

$$|\nu_\alpha\rangle = \sum_i U_{\alpha i} |\nu_i\rangle \quad (2.5)$$

$$|\nu_i\rangle = \sum_\alpha U_{\alpha i}^* |\nu_\alpha\rangle \quad (2.6)$$

The connection between the eigenstates can be made with the PMNS-matrix analog to the CKM-matrix in the quark sector [Les06]:

$$U = \begin{pmatrix} c_{12}c_{13} & c_{12}c_{13} & s_{13}e^{-i\delta} \\ -s_{12}c_{23} - c_{12}s_{23}s_{13}e^{i\delta} & c_{12}c_{23} - s_{12}s_{23}s_{13}e^{i\delta} & s_{23}c_{13} \\ s_{12}s_{23} - c_{12}c_{23}s_{13}e^{i\delta} & -c_{12}s_{23} - s_{12}c_{23}s_{13}e^{i\delta} & c_{23}c_{13} \end{pmatrix} \quad (2.7)$$

θ_{ij} :	mixing angles
δ :	phase factor
$e^{i\delta}$:	CP-violating phase

with $c_{ij} = \cos\theta_{ij}$ and $s_{ij} = \sin\theta_{ij}$. The phase factor δ is only non-zero if neutrino oscillations violate CP-symmetry.

In order to understand the outcome of experiments like Homestake, it is needed to obtain the time development of a mass eigenstate. Hence the Schrödinger equation is applied using $\hbar = c = 1$:

$$|\nu_i(t)\rangle = e^{iE_i t} |\nu_i\rangle \quad (2.8)$$

whereas the neutrino energy E_i is:

$$E_i = \sqrt{p_i^2 c^2 + m_i^2 c^4} \approx E + \frac{m_i^2 c^4}{2E} \quad \text{if } p \gg m_i \quad (2.9)$$

After propagating for the time t , the former pure eigenstate becomes:

$$|\nu(t)\rangle = \sum_i U_{\alpha i} e^{iE_i t} |\nu_i\rangle = \sum_{i,\beta} U_{\alpha i} U_{\beta i}^* e^{iE_i t} |\nu_\beta\rangle \quad (2.10)$$

Due to their different masses, the mass eigenstates propagate with different phase velocities. Since the mass eigenstates are combinations of flavor eigenstates, the neutrino has a probability to change its flavor during its propagation. The probability to observe a neutrino of flavor α transforming into one of flavor β can be expressed as

$$\begin{aligned}
 P_{\alpha \rightarrow \beta} &= |\langle \nu_\beta | \nu_\alpha(t) \rangle|^2 = \delta_{\alpha\beta} \\
 &\quad - 4 \sum_{i>j} \text{Re}(U_{\alpha i}^* U_{\beta i} U_{\alpha j} U_{\beta j}^*) \sin^2(\Delta m_{ij}^2 \frac{L}{4E}) \\
 &\quad + 2 \sum_{i>j} \text{Im}(U_{\alpha i}^* U_{\beta i} U_{\alpha j} U_{\beta j}^*) \sin^2(\Delta m_{ij}^2 \frac{L}{4E})
 \end{aligned} \tag{2.11}$$

with L being the traveled distance of the neutrino and E the starting energy of the particle.

In the simplified case of only two neutrino flavors only one angle θ and one mass difference $\Delta m^2 = |m_1^2 - m_2^2|$ exist leading to:

$$P_{\alpha \rightarrow \beta} = \sin^2(2\theta) \sin^2\left(\frac{\Delta m^2 L}{4E}\right) \tag{2.12}$$

In many cases (e.g. solar and atmospheric) the formula is appropriate. For instance in the atmospheric case of $\nu_\mu \rightarrow \nu_\tau$ the electron neutrino hardly plays a role. This is also viable in the solar case ($\nu_e \rightarrow \nu_x$), whereas ν_x is a superposition of ν_μ and ν_τ .

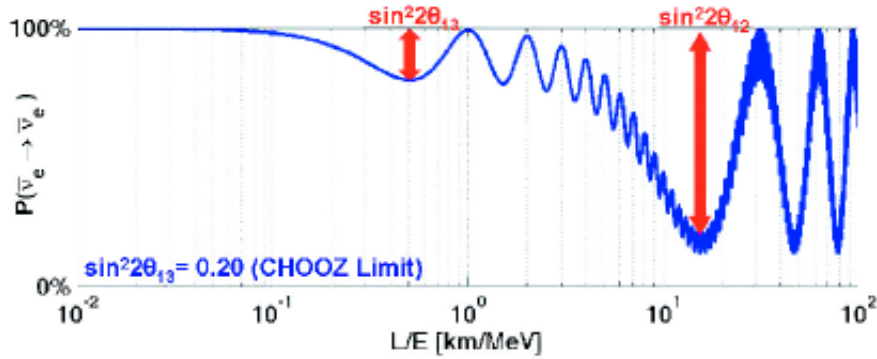


Figure 2.2: **The transition probability of the $\bar{\nu}_e \rightarrow \bar{\nu}_e$ process:** For low path lengths L/E the probability to transition is extremely unlikely ($P \approx 1$). As the values for L/E become higher, the probability starts to oscillate, thus strongly favoring transitions for specific L/E values. [KAT06]

First evidence for neutrino oscillation was found in 1998 by the Super-Kamiokande experiment under mount Kamioka, Japan. The neutrino detection was performed in a 50,000 ton ultra-pure water Cherenkov detector 1000 m underground. Incoming neutrinos could interact with the electron or the nuclei of the water, creating charged particles that move faster than the speed of light in water. Hence Cherenkov radiation is produced which can be detected by photomultiplier tubes in the tank. Super-Kamiokande was the first experiment with the ability to distinguish between electron neutrino events and muon neutrino events. By determining the ratio between both events and comparing it to Monte-Carlo simulations the evidence for neutrino oscillation was found. [Kam]

2 Neutrino Physics

Not only could Super-Kamiokande prove the existence of neutrino oscillation, they could also determine the atmospheric parameters like $\Delta m_{32}^2 = (2.43 \pm 0.13) \cdot 10^{-3} \text{ eV}^2$ and $\theta_{23} = 45^\circ \pm 7.1^\circ$. The solar mixing angle $\theta_{12} = 34.06^{+1.16}_{-0.84}^\circ$ as well as the solar mass difference $\Delta m_{21}^2 = (7.59^{+0.20}_{-0.21}) \cdot 10^{-5} \text{ eV}^2$ have been determined by experiments like SNO combined with Kamland. Further measurements in experiments like Daya Bay, Double Chooz and RENO could also measure the last mixing angle $\sin^2(2\theta_{13}) = 0.092 \pm 0.017$.

Despite all the progress that has been made with the neutrino oscillation experiments, they all lack the ability to measure the absolute neutrino mass, since they can only measure the squared mass differences Δm^2 between the three mass eigenstates.

2.4 Current neutrino mass experiments

Today there are basically three approaches to measure the neutrino mass. One indirect and two direct approaches are currently being used.

Observations conducted with instruments such as WMAP² and Planck or telescopes like the Hubble Space Telescope are trying to measure the sum of the three neutrino masses. Data on cosmic structure formation is used to extract information about neutrino properties. Several upper limits could already be derived by combining data from the different measurements. E.g. an upper limit obtained from WiggleZ³, WMAP, Hubble Space Telescope and *baobab*⁴ amounts to $\Sigma m_\nu < 0.29 \text{ eV}$ [Wig12]. However the conclusions derived from this information are heavily model dependent which leaves significant uncertainty in the results.

Another approach by several experiments is the attempted measurement of the neutrinoless double β decay ($0\nu\beta\beta$) shown in figure 2.3. This process can only happen if the neutrino is a Majorana particle (meaning it is its own anti particle), which is currently unknown. The other requirement, that the electron neutrino must have a mass greater than zero, is already established.

Essentially two β -decays take place at the same time in the same nucleus. The neutrino emitted by one nucleon is then absorbed by the nucleon of the second decay.

The decay rate of this process is given by

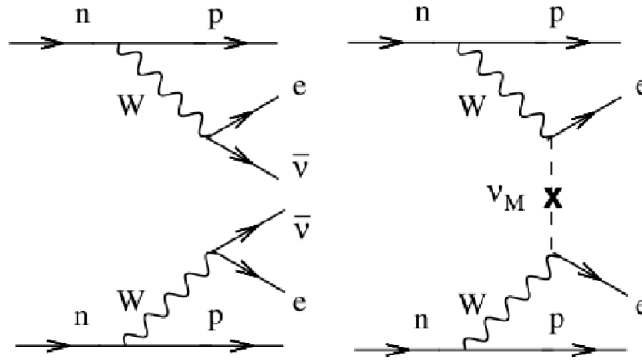
$$\Gamma = G |M|^2 |m_{ee}|^2 \quad (2.13)$$

G :	two-body phase-space factor
M :	nuclear matrix element
m_{ee} :	effective Majorana neutrino mass

²Wilkinson Microwave Anisotropy Probe

³WiggleZ Dark Energy Survey

⁴barion acoustic oscillations


 Figure 2.3: Feynman diagrams of the $2\nu\beta\beta$ - and the $0\nu\beta\beta$ -decay. [Avi07]

Hence, by measuring the decay rate, it would be possible to directly measure the so called effective Majorana mass:

$$m_{ee} = \left| \sum_i U_{ei}^2 \cdot m_{\nu_i} \right| \quad (2.14)$$

The GERDA collaboration found a lower limit for the half life of the decay of approx. $2.1 \cdot 10^{25}$ years.

No conclusive evidence of a $0\nu\beta\beta$ -decay has been found up to now. The very high half life shows how difficult it is to observe such a decay, because of the very low count rates that are to be expected.

The third approach presented, is the measurement of β -decay kinematics. The observable in such experiments is the weighted sum over the squared neutrino mass eigenvalues, according to equation 2.7:

$$m_{\bar{\nu}_e}^2 = \sum_{i=1}^3 |U_{ei}|^2 m_{\nu_i}^2 \quad (2.15)$$

In the KATRIN experiment and its predecessor experiments at Troitsk and Mainz the endpoint region of the Tritium beta decay is investigated.

As shown in figure 2.4 the Tritium atom decays into a Helium atom, an electron and an electron anti-neutrino $\bar{\nu}_e$. The decay energy is shared by the daughter nucleus, the electron and the electron anti-neutrino. Considering the high mass of the daughter nucleus compared to the electron and the anti-neutrino, the recoil energy of the nucleus can be neglected.

Applying Fermi's Golden Rule leads to the electron's energy spectrum.

$$\frac{d\dot{N}}{dE} = R(E) \cdot \sqrt{(E_0 - E) - m_{\bar{\nu}_e}^2 c^4} \cdot \theta(E_0 - E - m_{\bar{\nu}_e}^2 c^2) \quad (2.16)$$

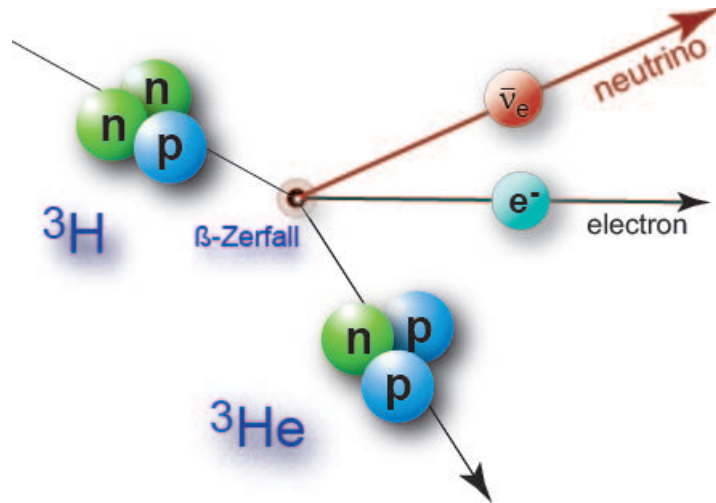


Figure 2.4: Schematic of the Tritium beta decay [KAT]

$$R(E) = \frac{G_F^2}{2\pi^3 \hbar^7} \cos^2(\theta_C) \cdot |M|^2 F(Z, E) \cdot p(E + m_e c^2) (E_0 - E) \quad (2.17)$$

G_F :	Fermi coupling constant
θ_C :	Cabibbo angle
$M(E)$:	nuclear matrix element for the transition
$F(Z, E)$:	Fermi function
p :	electron momentum
E :	kinetic energy of the electron
E_0 :	endpoint energy of the β -spectrum
m_e :	mass of the electron
$m_{\bar{\nu}_e}$:	mass of the electron anti-neutrino
$m_e c^2$:	rest energy of the electron
$m_{\bar{\nu}_e} c^2$:	rest energy of the electron anti-neutrino

In this simplified formula the final state distribution of the decay has been neglected. A non-zero electron anti-neutrino mass $m_{\bar{\nu}_e} \neq 0$ changes the shape of the β -spectrum in the endpoint region (figure 2.5).

By measuring the endpoint energy E_0 , the mass of the electron anti-neutrino mass $m_{\bar{\nu}_e}$ could be directly derived as a consequence of energy conservation:

$$E_{\max} = E_0 - m_{\bar{\nu}_e} c^2 \quad (2.18)$$

But as the count rate at the endpoint E_0 is very low, it will be covered by a considerable background. Therefore the region below the endpoint is measured. The anti-neutrino mass $m_{\bar{\nu}_e}$ can be extracted from the measured shape of the β -spectrum as one of four

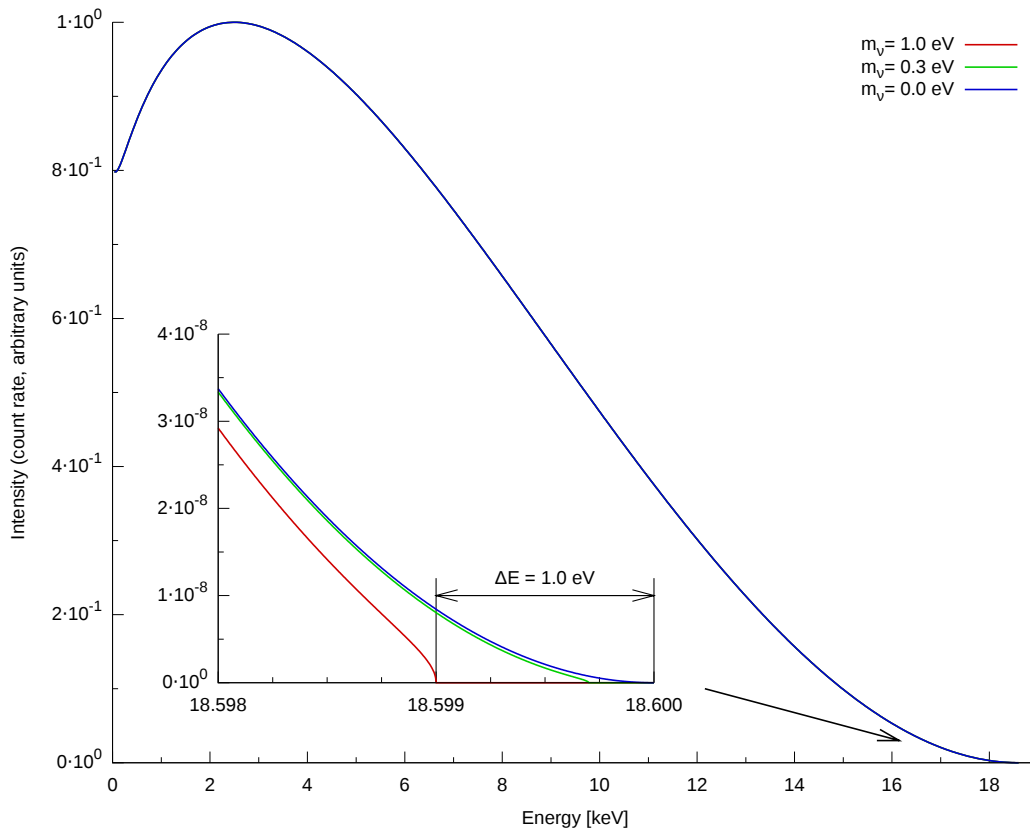


Figure 2.5: **Energy spectrum of the Tritium beta decay:** For a massless neutrino the endpoint lies at 18.6 keV. Deviations for $m_\nu = 1$ eV and $m_\nu = 0.3$ eV are also illustrated. In the end point region the differences can be distinguished best. [Beh12]

free parameters being the signal rate s , the background rate b , the endpoint energy E_0 and the electron anti-neutrino mass square $m_{\bar{\nu}_e}^2$.

In conclusion the shape of the energy spectrum is directly dependent on the electron anti-neutrino mass $m_{\bar{\nu}_e}$. Especially the endpoint region is of interest, as the sensitivity to the neutrino mass is highest there.

In principle this kind of measurement would work with any kind of β -decay though there are several reasons why Tritium has been chosen for the KATRIN experiment.

- Tritium has an endpoint energy of 18.6 keV which is the second lowest in nature. Low endpoint energies are favorable because statistically more events will fall into the endpoint region compared to decays with higher endpoint energies. This raises statistics and/or reduces measurement time.
- Tritium has a rather low half life of 12.3 a, making it simple to construct high luminosity β -decay sources.
- As a super-allowed transition the nuclear matrix element in the tritium β -decay is energy independent.

2 Neutrino Physics

- Atomic corrections for Tritium and its daughter nucleus ${}^3\text{He}^+$ can be calculated precisely, due to the simple atomic structure of both.
- Tritium has a low nuclear charge which leads to a small amount of inelastic scattering of decay electrons inside the source

3 The KATRIN experiment

This chapter will give an overview of the KATRIN experimental setup. The setup will be explained with special focus on the main spectrometer (MAC-E filter), for which the electron gun is designed. The MAC-E filter technology has already successfully been used in the predecessor experiments in Mainz and Troitsk. However in order to reach the much higher sensitivity ($\sim 100x$) than the predecessor experiments, the technology had to be developed further. One result of the development are the much larger scales of the experimental components in terms of pure size and complexity as seen in the following sections.

3.1 The Mac-E filter principle

The spectrometer parts of KATRIN (main spectrometer, pre-spectrometer and monitor spectrometer) are all based on the **M**agnetic **A**diabatic **C**ollimation and **E**lectrostatic (MAC-E) filter technology.

Despite using a high intensity tritium source, count rates in the endpoint region of the tritium beta decay are expected to be low (only $10^{-12} - 10^{-13}$ of all decays fall into the interval of 1 eV below the endpoint of the tritium β -spectrum). However as discussed in section 2.4 the endpoint region contains most of the information on the neutrino mass. Hence a spectrometer with an energy resolution in the order of 1 eV at the endpoint energy $E_0 \approx 18.6$ keV and a large angular acceptance is needed. These requirements are fulfilled by the KATRIN main spectrometer technology.

3.1.1 Working principle

The working principle of a MAC-E filter on the example of the KATRIN main spectrometer is shown in figure 3.1. The spectrometer entrance and exit ports are equipped with superconducting solenoids that create the magnetic field. Electrons entering the spectrometer are guided adiabatically on cyclotron tracks through the spectrometer to the detector. This means that the magnetic moment of the electron is preserved. Therefore most of the transverse energy E_{\perp} of the electrons is transformed into longitudinal energy E_{\parallel} in the analyzing plane. The adiabatic motion is accomplished by slowly decreasing the magnetic field strength B_{\max} from a maximum of 6 T at the pinch magnet at the spectrometer exit, to a minimum $B_{\text{ana}} = 3 \cdot 10^{-4}$ T in the analyzing plane. In the analyzing plane the electric and magnetic field lines are parallel so that only electrons with enough longitudinal energies E_{\parallel} can pass the spectrometer. The adiabatic transformation ensures that also electrons with high incident angles can be analyzed.

3 The KATRIN experiment

The main spectrometer works as a high-pass filter. An integrated beta spectrum is measured by scanning over different energy filter settings, determined by the applied retarding potential.

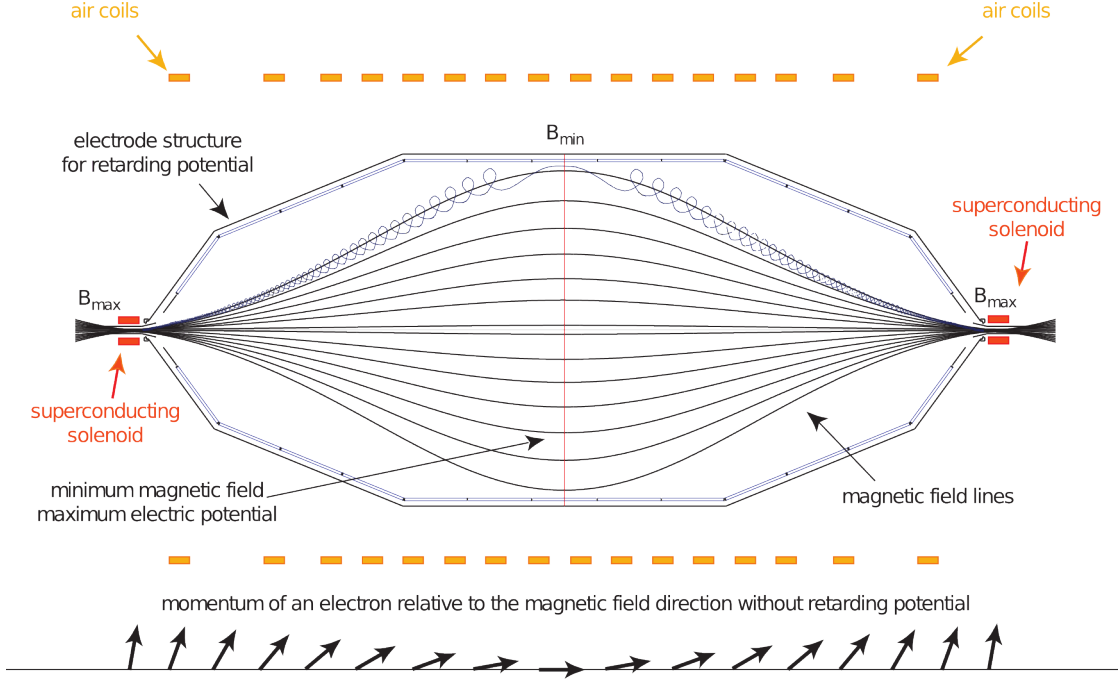


Figure 3.1: **Schematic of the KATRIN MAC-E filter:** Electrons are guided adiabatically through the main spectrometer in cyclotron motions (blue) around the magnetic field lines (black). The magnetic fields are generated by superconducting solenoids at both sides of the spectrometer and air coils around the spectrometer. In the analyzing plane (red line) at the center of the spectrometer, the electric field has its maximum and the magnetic field its minimum. The resulting momentum direction of an exemplary electron passing the spectrometer are shown at the bottom. [Hug08]

3.1.2 Energy resolution

The energy resolution is one of the key values that characterizes the quality of a MAC-E filter. In order to calculate the theoretical achievable energy resolution of an ideal MAC-E filter, the kinematics of electrons in the MAC-E filter will be investigated.

The kinetic energy of an electron entering the spectrometer can be expressed as the sum of longitudinal and transverse energy relative to the magnetic field line as follows:

$$\begin{aligned} E_{\text{kin}} &= E_{\parallel} + E_{\perp} \\ &= E_{\text{kin}} \cos^2 \theta + E_{\text{kin}} \sin^2 \theta \end{aligned} \quad (3.1)$$

Whereas θ is the angle between the electron momentum vector and the vector of the magnetic field line. In this case E_{\perp} is the energy of the cyclotron motion.

3.1 The Mac-E filter principle

As the magnetic and electric field strengths are only slightly changed over a cyclotron period, the motion is adiabatic. This means that the magnetic flux $\Phi = \int B dA$ enclosed by the gyration trajectory is constant. As a consequence the magnetic moment μ of the electrons keeps constant:

$$\gamma\mu = \text{const.} \quad (3.2)$$

Considering the maximum electron energies of the tritium beta decay, a non-relativistic approximation can be used:

$$\gamma_{\text{max}} = \frac{1}{\sqrt{1 - \frac{v^2}{c^2}}} = 1.04 \approx 1 \quad (3.3)$$

The magnetic moment can then be expressed as:

$$\mu = |\vec{\mu}| = \frac{e}{2m_e} |\vec{l}| = \frac{E_{\perp}}{B} = \text{const.} \quad (3.4)$$

The energy resolution ΔE of the MAC-E filter can be derived from that relation. It is assumed that the electron has all kinetic energy E_{kin} stored in the transverse component $E_{\perp, \text{start}}$ in the maximum magnetic field B_{max} at the center of the pinch solenoid. In the analyzing plane the magnetic field strength drops to a minimum B_{min} , at which point the electron has a minimum of transverse energy $E_{\perp, \text{ana}}$ left, as most of the energy is transformed into the longitudinal component. The transverse energy $E_{\perp, \text{ana}}$ in the analyzing plane is defined by the magnetic field strength B_{min} :

$$\mu = \frac{E_{\perp, \text{start}}}{B_{\text{max}}} = \frac{E_{\perp, \text{ana}}}{B_{\text{min}}} = \text{const.} \quad (3.5)$$

The remaining transverse energy $E_{\perp, \text{ana}}$, that is not transformed into longitudinal energy, can not be analyzed. This confines the energy resolution ΔE of the MAC-E filter and therefore identifies with the energy resolution of an ideal MAC-E filter:

$$\Delta E = E_{\perp, \text{ana}} = E_{\perp, \text{start}} \cdot \frac{B_{\text{min}}}{B_{\text{max}}} \quad (3.6)$$

For the KATRIN main spectrometer, the magnetic field strength drops from $B_{\text{max}} = 6 \text{ T}$ at the pinch magnet to $B_{\text{min}} = 3 \cdot 10^{-4} \text{ T}$ in the analyzing plane. The maximum kinetic energy of the tritium beta decay is approx. $E_0 \approx 18.6 \text{ keV}$. The resulting energy resolution is:

$$\Delta E = E_0 \cdot \frac{B_{\text{min}}}{B_{\text{max}}} = 18.6 \text{ keV} \cdot \frac{3 \cdot 10^{-4} \text{ T}}{6 \text{ T}} = 0.93 \text{ eV} \quad (3.7)$$

The corresponding relative energy resolution is:

$$\frac{\Delta E}{E_0} = 5 \cdot 10^{-5} \quad (3.8)$$

3.1.3 Transmission function

In this section the transmission function of the main spectrometer will be shortly discussed, as this characterizes the spectrometer and it is planned to measure this function with the electron gun described in this thesis. As stated in the previous section, the transverse energy of an electron is not fully transformed into longitudinal energy. Though only the longitudinal energy can be analyzed by a MAC-E filter. All electrons with a forward momentum ($\theta_{\text{solenoid}} < 90^\circ$) can enter the spectrometer and are analyzed. Therefore electrons with the same starting energy but different starting angles θ_{solenoid} (angle relative to the magnetic field at the center of the entrance solenoid), entering the spectrometer, have different transverse energies and hence different longitudinal energies $E_{\parallel, \text{ana}}$ in the analyzing plane. Thus the retardation potential U_0 at which electrons can pass the filter is directly dependent on the starting angle θ_{solenoid} :

$$\begin{aligned} E_{\parallel, \text{ana}} &= E_{\text{kin, ana}} - E_{\perp, \text{ana}} \\ &= E_{\text{kin, ana}} - E_{\perp, \text{start}} \cdot \frac{B_{\text{min}}}{B_{\text{max}}} \\ &= (E_{\text{kin, start}} - qU_0) - E_{\text{kin, start}} \sin^2 \theta_{\text{solenoid}} \cdot \frac{B_{\text{min}}}{B_{\text{max}}} \end{aligned} \quad (3.9)$$

With the condition, that electrons need to have a longitudinal energy greater than zero ($E_{\parallel, \text{ana}} > 0$) in the analyzing plane, in order to overcome the retarding potential U_0 , a transmission condition can be expressed:

$$\theta_{\text{solenoid}} \leq \theta_{\text{max}} = \arcsin \sqrt{\frac{E_{\text{kin, start}} - qU_0}{E_{\text{kin, start}}} \frac{B_{\text{max}}}{B_{\text{min}}}} \quad (3.10)$$

Only electrons below θ_{max} can overcome the retarding potential U_0 and pass the MAC-E filter. Therefore the relation from the accepted solid angle $\Delta\Omega$ and the theoretical 2π -acceptance is given by:

$$\frac{\Delta\Omega}{2\pi} = 1 - \cos \theta_{\text{max}} \quad (3.11)$$

With (3.10) and $E_{\text{kin, start}} = E$ the transmission function is:

$$T(E, U_0) = \begin{cases} 0 & , E \leq qU_0 \\ 1 - \sqrt{1 - \frac{E - qU_0}{E} \frac{B_{\text{max}}}{B_{\text{min}}}} & , qU_0 < E < qU_0 + \Delta E \\ 1 & , qU_0 + \Delta E \leq E \end{cases} \quad (3.12)$$

3.1 The Mac-E filter principle

The width of the transmission function is determined by the magnetic field ratio $\frac{B_{\max}}{B_{\min}}$.

However an additional effect on the transmission function that reduces the number of electrons passing the filter has to be taken into account. Decay electrons from the source transition from a magnetic field $B_{\text{source}} = 3.6 \text{ T}$ into a region of higher magnetic field $B_{\max} = 6 \text{ T}$ at the pinch magnet in the detector region. Hence all electrons higher than a critical angle are magnetically reflected:

$$\theta_{\text{mirror}} = \arcsin \sqrt{\frac{B_{\text{source}}}{B_{\max}}} \approx 50.77^\circ \quad (3.13)$$

This has the effect of background reduction since electrons with higher starting angles also have a higher path length in the WGTS, because of their larger cyclotron radii, which results in a larger probability for scattering processes. By including this effect, the transmission function of (3.12) has to be rewritten:

$$T(E, U_0) = \begin{cases} 0 & , E \leq qU_0 \\ \frac{1 - \sqrt{1 - \frac{E - qU_0}{E} \frac{B_{\text{source}}}{B_{\min}}}}{1 - \sqrt{1 - \frac{\Delta E}{E} \frac{B_{\text{source}}}{B_{\max}}}} & , qU_0 < E < \Delta E \\ 1 & , \Delta E \leq E \end{cases} \quad (3.14)$$

Equation (3.14) is visualized in figure 3.2.

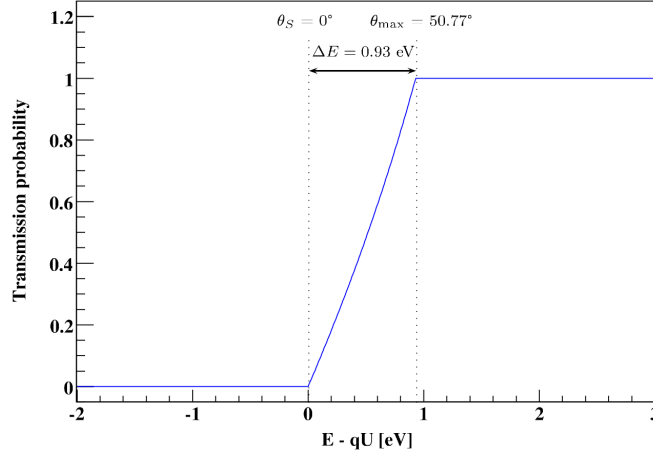


Figure 3.2: **The analytic transmission function of the KATRIN MAC-E filter:** The transmission function has been normalized to 1 in the region of maximum transition. The width of the transmission function is determined by the maximum starting angle θ . The figure was taken from [Wol08].

3.2 Setup

The KATRIN setup consists of seven different sections (figure 3.3), that each will be addressed in this section.

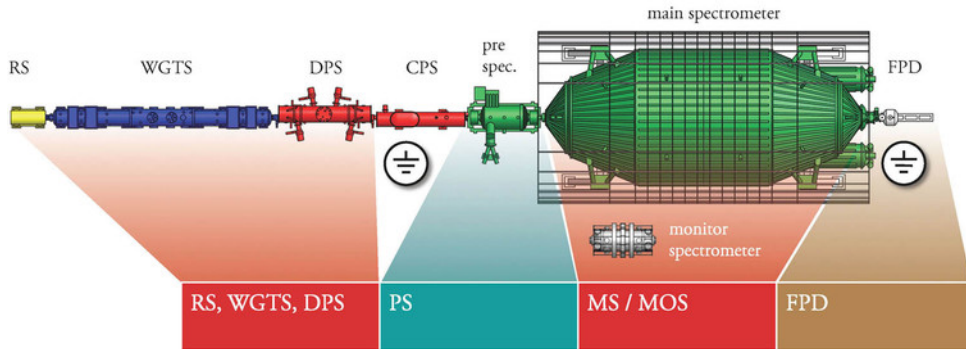


Figure 3.3: **Setup of the KATRIN experiment:** RS: rear section; WGTS: windowless gaseous tritium source; DPS/CPS: transport sections; PS: pre-spectrometer; MS: main spectrometer; MoS: monitor spectrometer; FPD: focal plane detector [KAT]

3.2.1 Rear section (RS)

The rear section (RS) will be used to close the KATRIN setup mechanically and electrically. It is also equipped with an electron gun to measure the column density of the source and a detector to measure the source activity.

3.2.2 Windowless gaseous tritium source (WGTS)

The windowless gaseous tritium source (WGTS) is the source of the β -electrons that will be analyzed. The source consists of a 10 m long tube with an inner diameter of 90 mm. It has to provide a stable flow of electrons as well as a high intensity of about 10^{11} Bq. The source is windowless, since a window would alter the energy of the electrons, leading to systematic errors in the measurements. As a consequence tritium can diffuse into the main spectrometer and create background there through the beta decays. One measure to reduce the tritium flow is to mount two turbo molecular pumps that remove tritium at both ends of the source, whereas in the center the tritium is injected. After removal, the tritium is repurified and then reinjected into the source (figure 3.4).

Reaching a timely and spatially constant gas column requires a constant temperature as well as a constant pressure in the tube. Furthermore the absolute temperature has to be around 30 K so that electron energy corrections, that have to be taken into account, do not become too large. The stability of the temperature has to be in the permille level, which is quite challenging for a 10 m long tube. This stability requirement is also true for the pressure and the T_2 purity, making the WGTS one of the most complicated parts of the KATRIN experiment.

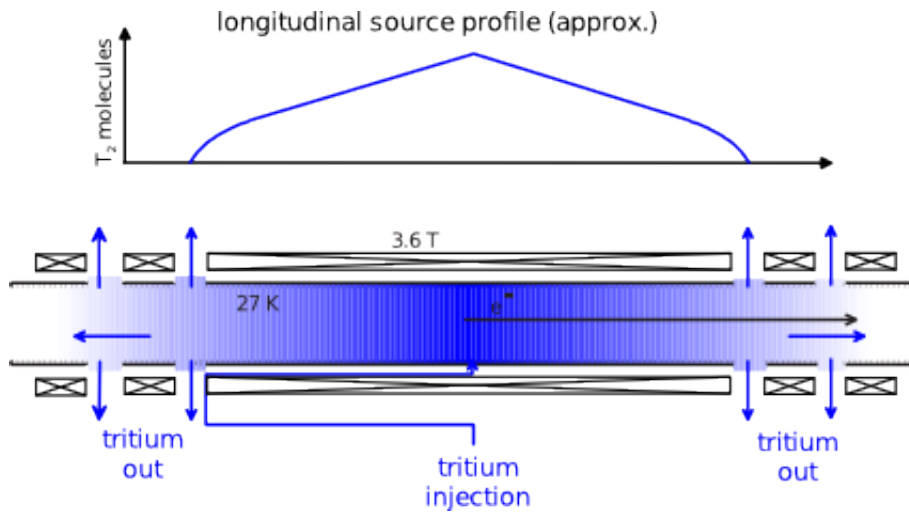


Figure 3.4: **Windowless gaseous tritium source schematic:** *Top:* density profile over source length *Bottom:* tritium gas injection into the tube and first pumping stages [KAT]

3.2.3 Transport section (DPS and CPS)

The transport section consists of the differential pumping section (DPS) and the cryogenic pumping section (CPS). Electrons coming from the source are guided adiabatically by a magnetic field through both parts of the transport section towards the spectrometer whereas the tritium flow towards the main spectrometer is reduced, in order to avoid background in any of the spectrometer parts.

The DPS contains four turbomolecular pumps, each of them positioned at one of the four bends in the tube (3.5).

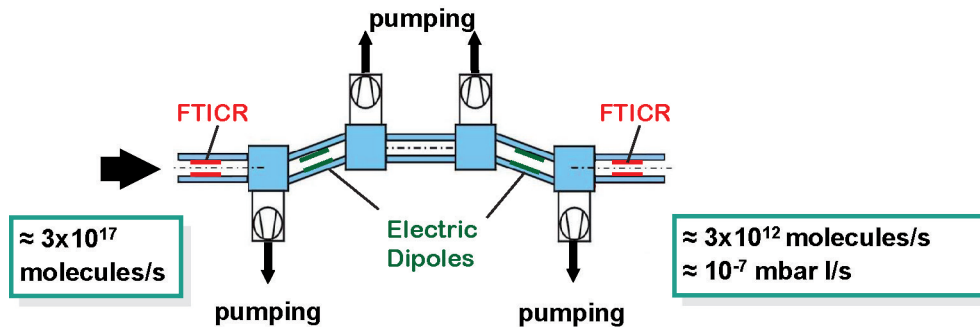


Figure 3.5: **Schematic of the differential pumping section (DPS)** [KAT]

While the electrons follow the magnetic field lines that guide them to the main spectrometer, the tritium molecules fly on straight trajectories and are removed at the bends. In that fashion the tritium flow can be reduced by a factor of approximately 10^7 .

In the CPS tritium is removed by absorbing gas molecules onto an argon frost layer that is covering the gold plated beam tube at 3 K. Same as the DPS, the beam tube is bent

3 The KATRIN experiment

in order to increase the probability for T_2 to hit the wall. This leads to a further tritium flow reduction of a factor 10^7 .

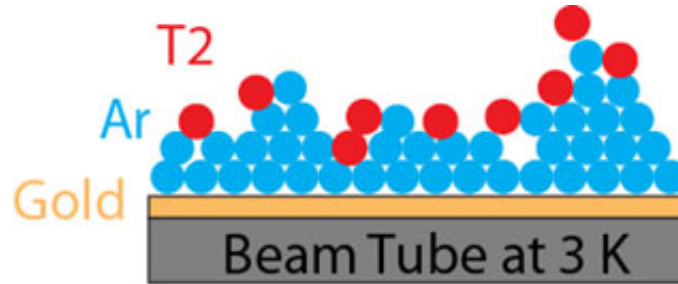


Figure 3.6: Principle of the cryo-sorption [KAT]

The total remaining tritium flow through the transport section shall thus be reduced by a factor 10^{-14} .

3.2.4 Pre-spectrometer (PS)

The pre-spectrometer (PS), like the main spectrometer and the monitor spectrometer, is based on the MAC-E filter technology, which was explained in section 3.1 with special focus on the main spectrometer. It is a cylindrical stainless steel tank with an outer diameter of 1.7 m and a total length of 3.38 m. The pressure in the tank will be at about 10^{-11} mbar. The energy resolution of the pre-spectrometer is in the order of 100 eV, which is sufficient for a pre-filter.

The pre-spectrometer's main purpose is to filter electrons with energies up to 18.3 keV to reject unwanted low energy electrons. The rejected electrons are reflected back towards the source section. Thus the electron flux is reduced by a factor of $\sim 10^7$ so that only a flux of the order of $10^3 \frac{e^-}{s}$ remains. With less electrons reaching the main spectrometer the background level through rest gas ionization is reduced.

3.2.5 Main spectrometer (MS)

In the main spectrometer the main energy analysis of the decay electrons takes place. The spectrometer has a conical shape and is approx. 23 m long and has a center diameter of 9.8 m (see figure 3.3). It has an inner volume of 1400 m^3 and is therefore the biggest spectrometer of its kind. In order to reach a vacuum of about 10^{-11} mbar, there are three pump ports with approx. 1.7 m in diameter. The pump ports are equipped with getter material and turbomolecular pumps. The pre-vacuum is supplied by two large scroll pumps. The entrance and the exit are equipped with superconducting solenoids that can provide up to 6 T magnetic fields. Around the main spectrometer an air coil system has been built to neutralize magnetic field disturbances induced by the earth magnetic field and shape the magnetic field inside the spectrometer.

Inside the spectrometer is a dual layer wire electrode system. The wire electrodes purpose is to reduce background and shape the electric field. The background comes from inside the spectrometer hull, where radioactive decays in the stainless steel take place, as well as from cosmic muons that generate electrons in the hull through collisions. By applying two layers with a potential gradient, the background electrons will be reflected back to the hull (figure 3.7). Wires are used to minimize the mass of the electrode system. If the mass was higher, the wire electrode would become a background source itself, since decay electrons or muon induced electrons can also be emitted from there.

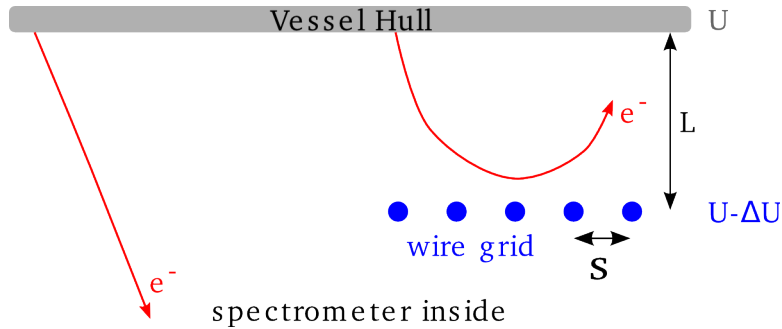


Figure 3.7: **Working principle of the wire electrode:** Electrons without the electrode can enter the spectrometer (left side). With the wire electrode present the electrons are reflected back to the hull (right side). This does only work if the wire electrode is on a lower (more negative) potential than the hull. [Zac09]

3.2.6 Monitor spectrometer (MoS)

The Monitor spectrometer (MoS) is the same spectrometer that was used for the Mainz experiment. In KATRIN it is used to monitor the high voltage of the main spectrometer and is therefore electrically connected to the main spectrometer. It will measure the energy of conversion electrons from the Kr-83m decay. These electrons always have the same well defined energy. Hence fluctuations in the high voltage can be directly observed in the transmission function that the MoS delivers.

3.2.7 Focal plane detector (FPD)

The focal plane detector (FPD) is positioned at the exit of the KATRIN main spectrometer. It is a silicon based PIN diode. The detector has an energy resolution of < 1 keV for electron energies of approximately 18.6 keV. This seems rather low considering the needed energy resolution in the order of 1 eV. However since the main spectrometer acts as a very precise high-pass filter, the detector only needs to count electrons. The < 1 keV resolution is mainly desired to be able to distinguish between background electrons and signal electrons.

One important feature of the detector is that it is segmented into 148 pixels of equal area size (fig. 3.8). This spatial resolution is crucial for test measurements with the

3 The KATRIN experiment

electron gun in order to measure inhomogeneities of the electromagnetic fields in the analysis plane of the main spectrometer.

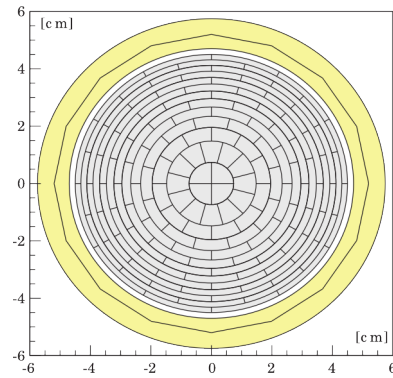


Figure 3.8: **The KATRIN detector:** The detector is subdivided into radial segments. Each segment has the same size. [Val09]

4 Electron source principles

In this chapter the requirements that the electron gun has to fulfill in order to work as a calibration source for the KATRIN main spectrometer will be explained. Another focus will be on the working principle of the electron gun developed in the scope of this thesis. Furthermore the predecessor electron gun that could already prove the principle of angular selectivity, will be shortly presented.

4.1 Calibration source requirements

The sensitivity to the electron anti-neutrino mass $m_{\bar{\nu}_e}$ in the KATRIN experiment depends on the precision and stability of the electromagnetic fields inside the main spectrometer. Since the main spectrometer is not an ideal MAC-E filter as depicted in chapter 3, it shows electric field variations of $\Delta U \approx 1.2\text{ V}$ over the radius of 4.5 m in the analyzing plane [Bok13]. The magnetic field shows a variation of $\Delta B = 0.4\text{ G}$ in the analyzing plane. If these effects are not taken into account during the analysis of the tritium β -decay data, the transmission function would broaden from the ideal value $\Delta E = 0.93\text{ eV}$ to $\Delta E \approx 2\text{ eV}$ as shown in figure 4.1.

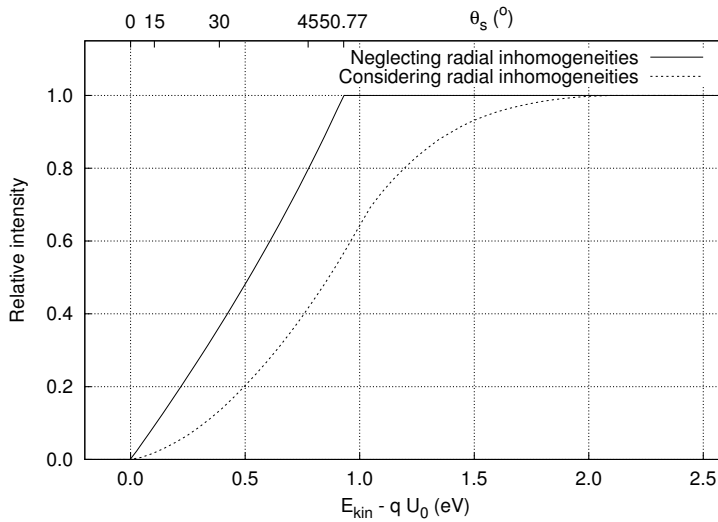


Figure 4.1: Broadening of the ideal transmission function as a result of electric and magnetic field inhomogeneities ($\Delta U \approx 1.2\text{ V}$, $\Delta B = 0.4\text{ G}$). Figure taken from [Bok13].

In order to measure these characteristics of the main spectrometer, a calibration source

is mounted to the source side spectrometer entrance. To work as such a source the electron gun has to meet the following requirements:

- **Point-like source and mobility**

As mentioned in chapter 3.2.7, the focal plane detector is radially segmented to be able to measure the impact of the field variations in the main spectrometer. Each pixel covers an area of almost constant field variation in the analyzing plane. By measuring the transmission function for each pixel, the field inhomogeneities can be taken into account. The electron gun therefore has to have a point-like emission characteristic, so that each pixel of the detector can be targeted independently. For the same reason the electron gun has to be able to move over the whole flux tube of 191 Tcm^2 and therefore reach every pixel. Simulations on the topic of flux tube coverage can be found in chapter 6.2.

Another important feature of the mobility is that the integrity of the wire electrode at the spectrometer wall can be investigated with electrons passing the spectrometer on outer trajectories. Electrode defects like disconnected modules or wires hanging down into the fluxtube would change the expected transmission function for the corresponding detector pixel, and can thus be identified.

- **Angular selectivity and small energy spread**

In chapter 3.1.3 it was explained, that one reason for the transmission function broadening ΔE of the KATRIN main spectrometer is the angular spread of electrons coming from the tritium source. Being able to set a well-defined starting angle θ with a small angular spread σ_0 for the electrons, will allow to investigate the angle dependent contributions to the transmission function width (figure 4.2). The figure illustrates, that with an angular selective electron source it is possible to scan over the transmission function for an isotropic source such as the tritium source. To this end the calibration source is also required to create electrons that cover the full angular range of $0^\circ \leq \theta_{\text{solenoid}} \leq 90^\circ$.

Setting a sharp angle requires a well defined electron starting energy with small spread $\sigma_E \rightarrow 0$. If the energy spread σ_E of the electrons is too large, it is impossible to distinguish between the effects on the transmission function coming from the field inhomogeneities or from the energy spread of the electron gun itself. Therefore the energy spread of the electron gun has to be much smaller than the ideal width of the transmission function ($\sigma_E \ll 0.93 \text{ eV}$).

- **Pulsed source**

It is also possible to investigate electromagnetic field inhomogeneities by analyzing the time of flight (TOF) spectra of the electrons. This is accomplished by comparing the measured TOF spectra to simulated spectra. To be able to measure the TOF of electrons, the electron gun has to be able to operate in a pulsed mode, so that the electron starting time can be determined. [Val09] [Ste12a]

- **Adjustable intensity**

Because of the variety of planned commissioning measurements at the main spectrometer, the electron gun needs to have an adjustable electron rate. For example transmission function measurements need high statistics, whereas in TOF mea-

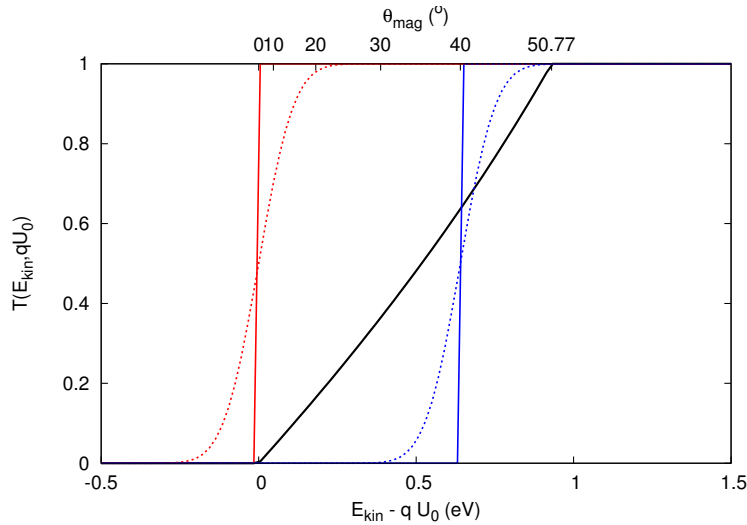


Figure 4.2: **Transmission functions for different electron sources at the KATRIN main spectrometer:** The black line is the transmission function of an isotropic electron source (such as the tritium source). The colored lines are transmission functions for angular selective electron sources (red lines for $\theta_{\text{solenoid}} = 0^\circ$, blue lines for $\theta_{\text{solenoid}} = 40^\circ$). The solid lines represent a monoenergetic source and the dashed lines a source with energy spread σ_E . [Bok13]

surements the use of single-electron emission would be preferred. Additionally adjusting the intensity allows to measure intrinsic characteristics of the FPD (e.g. pile-up).

4.2 Working principle

The electron creation and acceleration principle of the electron gun developed in the scope of this thesis will be explained in the following subsections. The working principle already proved to be successful for the predecessor electron gun developed by K. Bokeloh [Bok13], J.H. Hein [Hei10] and K. Valerius [Val09].

4.2.1 Electron creation

The electrons are created via the photoelectric effect. In the photoemission process an electron within a material absorbs the energy of an incident photon and is ejected with the energy E_{start} from the material if the photon energy $E_{\text{ph}} = \frac{h \cdot c}{\lambda}$ is greater than or equal to the work function of the material W :

$$E_{\text{start}} = \frac{h \cdot c}{\lambda} - W \quad (4.1)$$

For the electron gun to have a small electron starting energy spread σ_E , a light source and a cathode material have to be matched in a way that the electron starting energies E_{start} are minimal. If $E_{\text{ph}} \gg W$ electrons from deeper parts of the material can also be ejected. These electrons would have less surplus energies than the electrons closer to the surface since they are ejected from a lower energy level.

4.2.2 Electron acceleration

The photoelectrons are created in the cathode material which is integrated in the center of a backplate of a rotatable parallel plate capacitor (chapter 5.5). The capacitor has an adjustable absolute potential U_{start} (potential on the backplate of the capacitor), as well as adjustable potential difference ΔU (given by $U_{\text{start}} - U_{\text{front}} = \Delta U$) between front- and back plate. In a first step the electrons are accelerated along the electric field lines towards the front plate according to:

$$F = q \cdot (\vec{E} + \vec{v} \times \vec{B}) \quad (4.2)$$

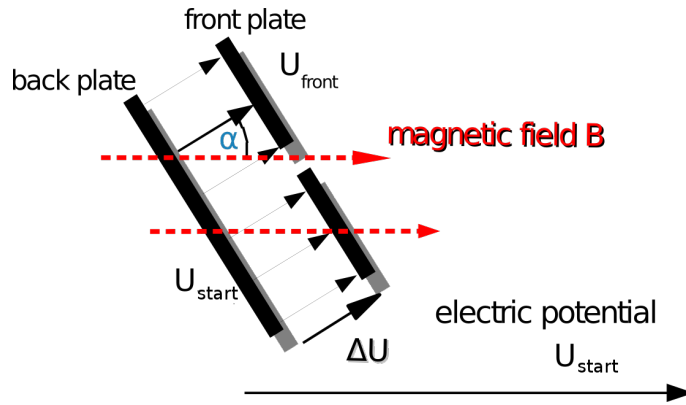


Figure 4.3: **Electron gun principle (left)**: Electrons are accelerated by the electric field between the capacitor plates. Eventually the magnetic guidance takes over and the electrons move on cyclotron motions towards the spectrometer. The transverse energy E_{\perp} is determined by the parameters ΔU and α . [Hei10]

In a second step the electrons are accelerated against the surrounding ground potential after passing the front plate. When an electron reaches the ground potential of the surrounding chamber, the total energy of the electron is proportional to the acceleration voltage ($E \sim qU_{\text{start}}$). Since the starting velocity \vec{v} of the photoelectrons is very low, the influence of the electric field is dominant at the start of the trajectory resulting in a non-adiabatic acceleration on the first few nanometers. After the initial non-adiabatic acceleration, the electrons are transitioned into an adiabatic cyclotron motion guided by the magnetic field lines. By setting an electron gun angle α between the electric and the magnetic field, the electrons will have an angle θ_{ad} with respect to the magnetic field line after transition into a region with $U \approx 0$. The angle θ_{ad} is directly monotonic dependent on the angle α and the kinetic energy $E_{\text{kin,ad}} \sim q\Delta U$ (figure 4.3).

Hence the transverse energy $E_{\perp,ad}$ is determined by the angle θ_{ad} and the kinetic energy $E_{kin,ad}$. This means, that the angle $\theta_{solenoid}$ is also determined by the parameters θ_{ad} and $E_{kin,ad}$, as can be shown by using equations (3.1) and (3.4):

$$\begin{aligned} \frac{E_{\perp,ad}}{B_{ad}} &= \frac{E_{\perp,solenoid}}{B_{solenoid}} \\ \frac{E_{kin,ad}}{B_{ad}} \cdot \sin^2 \theta_{ad} &= \frac{E_{kin,solenoid}}{B_{solenoid}} \cdot \sin^2 \theta_{solenoid} \\ \implies \sin^2 \theta_{ad} &= \frac{B_{ad}}{B_{solenoid}} \cdot \sin^2 \theta_{solenoid} \end{aligned} \quad (4.3)$$

With the starting angle α and the potential difference ΔU between the plates the parameters θ_{ad} and $E_{kin,ad}$ can be set. The two parameters α and ΔU therefore also determine the angle $\theta_{solenoid}$.

The magnetic field is much lower ($B_{ad} \approx 4 \cdot 10^{-2}$ T) at the point where the adiabatic motion starts to take over than in the center of the entrance solenoid ($B_{solenoid} = 4.5$ T). From the difference in field strength follows that the angle θ_{ad} corresponds to much larger angles $\theta_{solenoid}$, which can be seen by applying the values for B_{ad} and $B_{solenoid}$ to equation 4.3. The dependency between $\theta_{solenoid}$, α and the electron starting energy spread σ_E is shown in figure 4.4 which is a result of a Monte-Carlo simulation for the electron gun.

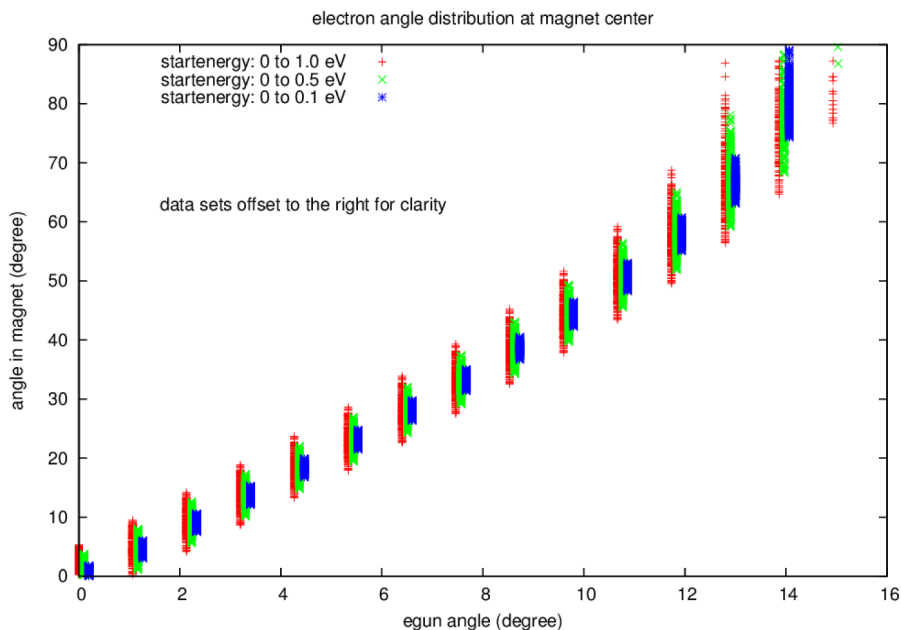


Figure 4.4: **Dependency between electron starting energy spread ΔE_{start} , e-gun angle α and electron angle $\theta_{solenoid}$ in magnet center:** This is the result of a Monte-Carlo simulation with 1000 particles per run. The electron starting energy spread ΔE_{start} has been assumed as uniformly distributed. [Zac13]

4 Electron source principles

As a result of the lower magnetic field in the electron gun region already relatively small angles α suffice to reach the maximum angle $\theta_{\text{solenoid}} = 90^\circ$.

4.2.3 Predecessor electron gun

The working principle of the electron gun has already been investigated with a prototype electron gun with the conclusions published in [Bec13]. The angular selectivity of this prototype could be validated with measurements at the former Mainz spectrometer, which now serves as monitor spectrometer at KIT.

To achieve angular selectivity a parallel plate capacitor was mounted to a ceramic rod that was connected to a manipulator. This allowed aperture-centered rotation with the ability to set α in steps of 0.1° (figure 4.5 left).

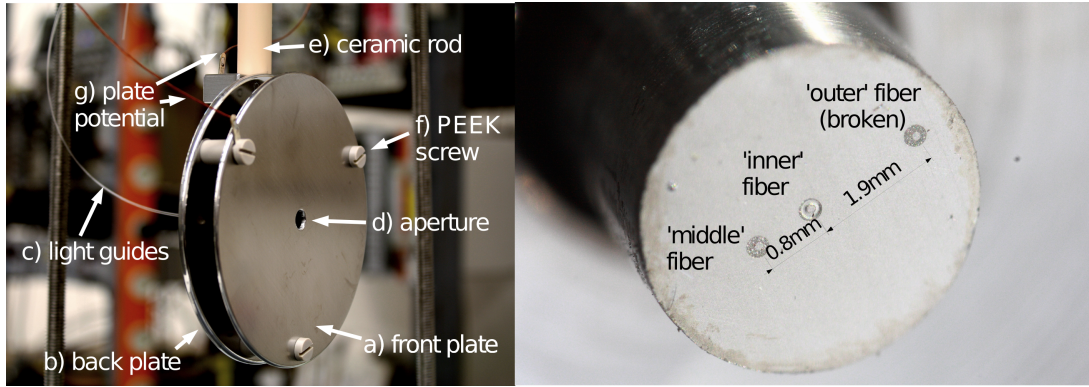


Figure 4.5: **Predecessor electron gun (left) and cylinder with three optical fibers (right):** *left:* The parallel plate capacitor is mounted to a rotatable ceramic rod *right:* The fibers were glued into the cylinder and are covered with a silver layer. (figures taken from [Hei10])

As cathode material polycrystalline silver with a work function in the range of $\Phi_{\text{Ag,poly}} \approx 4.00 \text{ eV}$ (value taken from [Eas17]) was used. A silver layer of $35(\pm 5) \frac{\mu\text{g}}{\text{cm}^2}$ density was evaporated onto three optical fibers with core diameters of $d_{\text{core}} = 15 \mu\text{m}$ which were illuminated by an UV-LED with a wavelength of $\lambda_{\text{LED}} = (265 \pm 15) \text{ nm}$ (corresponding to a theoretical maximum starting energy of $E_{\text{start,max}} = 0.68 \text{ eV}$). The fibers were glued into a cylinder with three micro boreholes at different positions on the cylinder (figure 4.5 right) to be able to test different starting positions of the created electrons.

The results of the measurements show clear evidence for the angular selectivity in the full range of $\theta_{\text{mag}} \in [0^\circ:90^\circ]$ by changing the parameters electron gun tilt angle α and potential difference ΔU between the plates. This is shown in figure 4.6.

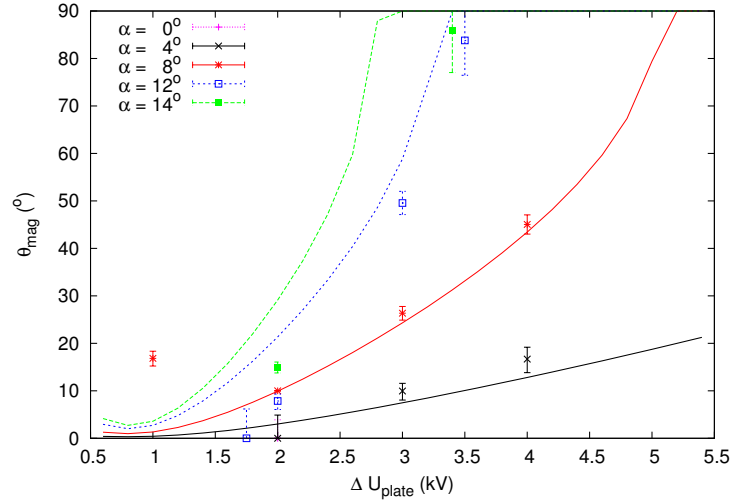
In figure 4.6a the comparison between measurement and simulation is shown. The measured dependency of the angles θ_{mag} on the source parameters α and ΔU have a similar shape to the simulated values. Indications of the impact of the energy spread σ_E can be seen in the deviations from measurement to simulation at low potential differences

ΔU . In the simulations the starting energy distribution is not taken into account, which explains the deviations.

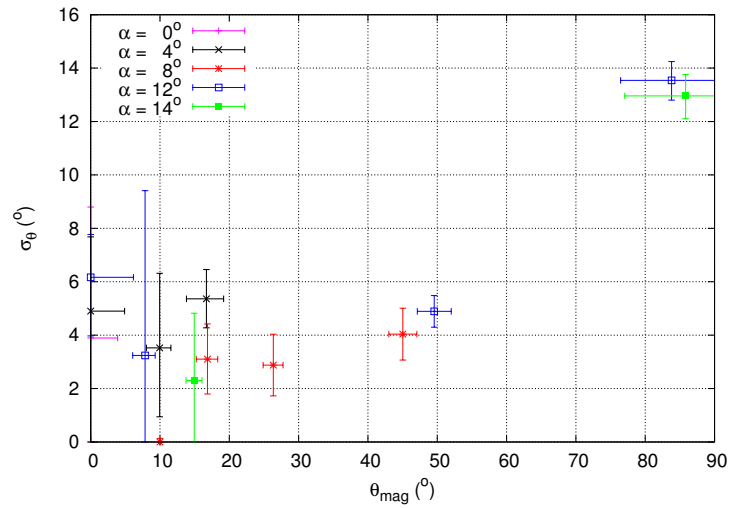
In figure 4.6b the angular width σ_θ is shown in dependency of θ_{mag} . For small angles θ_{mag} the angular width lies in the interval of $\sigma_\theta \in [2^\circ; 6^\circ]$ while for angles θ_{mag} close to 90° the angular spread is $\sigma_\theta \approx 13^\circ$.

Because of these results the working principle was adopted for the electron gun developed in the scope of this thesis. Improvements like a smaller energy spread σ_θ and therefore better angular selectivity as well as rotation of two independent axes for the e-gun setup have been investigated in the following chapters.

4 Electron source principles



(a) Dependency of the electron angle θ_{mag} in the magnet on the parameter ΔU for different electron gun tilt angles α .



(b) Dependency of the angular width σ_θ on the angular emission angle θ_{mag} .

Figure 4.6: **Predecessor e-gun measurements** [Bok13]

5 Electron gun components

In this chapter the different components used for the electron gun will be presented.

5.1 Light sources

For the electron gun two different kind of light sources are used. The first source is a laser that provides very sharp photon energies as well as high photon rates. The second kind of source are UV-LEDs that are available at different wavelengths and therefore provide adjustable electron starting energies when used in combination with a monochromator.

UV laser Using a laser has the advantage of well defined photon energies which, when matched to a suitable cathode material, minimizes the spread of the starting energies of the photoelectrons. Another advantage are the precisely timed short but strong pulses that lasers can provide. Additionally achieving high electron rates is unproblematic because of the high output powers of lasers. Having narrow, parallel beam profiles, laser beams are easy to couple into other optical components.

For those reasons a pulsed, frequency quadrupled Nd : YVO₄-laser system (type: mosquito) with a wave length of $\lambda = 266$ nm from InnoLas Holding GmbH has been used as the primary light source in the experiments presented in this thesis. The mosquito is a custom made laser system that provides much lower output powers with a maximum of $P_{\max} \approx 6.5$ mW than a standard mosquito UV laser which has output powers in the region of approx. 100 mW. For the calibration source high output powers are not necessary to create the desired electron rates. Therefore the Laser beam is not focused onto the fourth harmonic generation crystal in order to increase the lifetime of the crystal, which is usually the part in the laser that has the shortest lifetime. Additionally the relative output power can be set from 0% – 100% of the current power setting by an internal $\frac{\lambda}{2}$ -plate in combination with a beam splitter. The $\frac{\lambda}{2}$ -plate rotates the polarization direction of the linear polarized light. The beam splitter then splits the laser beam into two fractions dependent on the orientation of the polarized light. In the laser setup the reflected fraction of the beam is reflected onto a beam dump. By adjusting the angle of the $\frac{\lambda}{2}$ -plate the relative output power of the laser can be set from 0% – 100%.

With the adjustable output power suitable electron rates for the different measurements can be achieved. The laser pulse repetition frequency f_{PRF} is adjustable between 20 kHz and 100 kHz which is suitable for time of flight measurements. The output power can be adjusted by the current of the diode I_{diode} that is used for laser pumping (specified from 6 A – 8 A) and the pulse repetition frequency f_{PRF} .

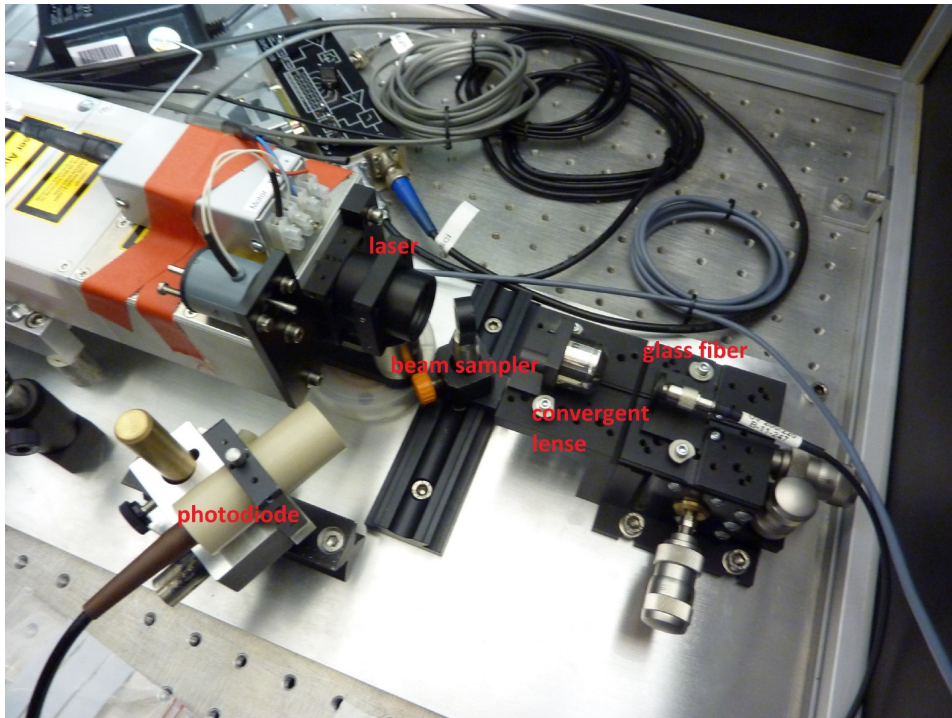


Figure 5.1: **Setup of the Nd : YVO₄– laser system at KIT:** Laser with optical bench for coupling of the laser light into the optical fiber. A beam splitter reflects a small fraction of the laser light onto a photodiode to monitor the laser stability. [**Pot13**]

The laser provides photon energies of $E_{\text{ph}} = 4.66 \text{ eV}$. For those energies several cathode material candidates have been considered, as discussed in the next section. The laser setup is shown in figure 5.1. The laser beam is focused onto the fiber by a lens (Thorlabs RMS4x193) which is mounted on a fiber launch (Thorlabs MBT613/M). The fiber launch has a three-axis positioning stage for high precision adjusting. A green filter is used to absorb the green part ($\lambda = 532 \text{ nm}$) of the laser light. The beam splitter (Thorlabs BSF05-UV) and the photodiode (OSI Optoelectronics UV-035EQ) in the picture were implemented in a later stage of the setup for the measurements at KIT. The beam splitter reflects a part of the laser light onto the photodiode to monitor the laser photon intensity.

UV-LEDs As an alternative light source UV-LEDs with different peak wavelengths (265 nm - 315 nm) were used (Roithner UVTOP260 - UVTOP310). The LEDs have a wavelength spectral range of $\approx 40 \text{ nm}$ (figure 5.2), which leads to a much broader energy spread σ_E of the photoelectrons compared to a laser. The energy spread σ_E can be limited if the cathode material is matched to the spectrum of the UV-LED in a way that only a limited spectral range of the LED provides enough photon energy to extract photoelectrons. Alternatively a monochromator is applied to limit the spectral range and set the wavelength of the UV-light so the energy spread of the photoelectrons can

be minimized. However both methods come at the cost of a much lower electron rate. Another downside of using UV-LEDs are the low maximum output powers ($\sim 800 \mu\text{W}$) and inferior beam profiles compared to a laser. Hence the UV-LEDs can only be used in measurements that do not need high electron rates.

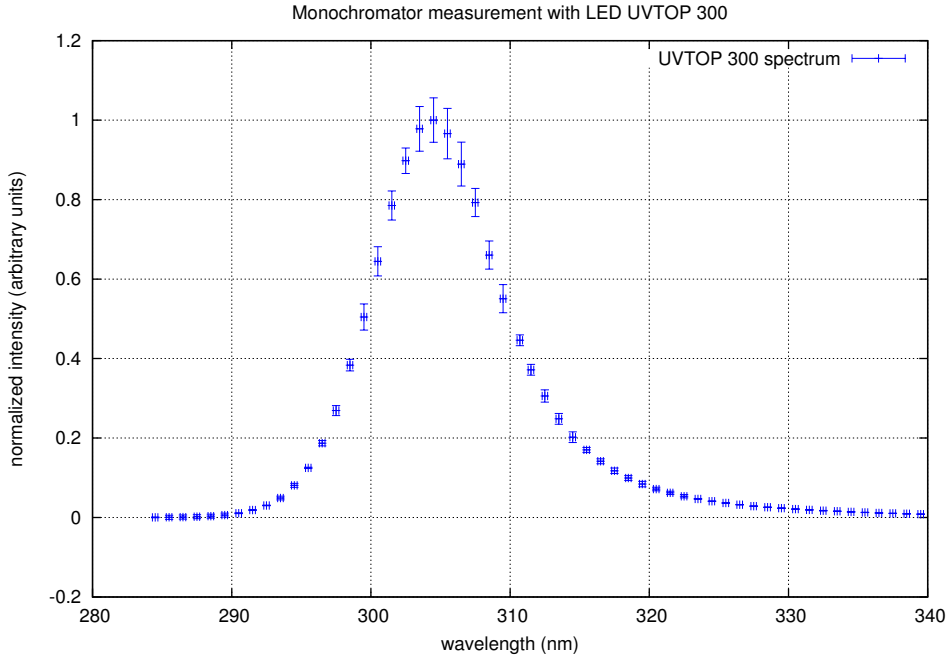


Figure 5.2: **Measured spectrum of LED UVTOP 300**

For easier coupling into other optical components the UV-LEDs were purchased with an equipped ball lens. To measure the spectra of the UV-LEDs a grating spectrometer (Horiba, model: Jobin Yvon H10) that served as a monochromator was used in combination with a Si-PIN photodiode (OSI Optoelectronics UV-035EQ).

At Münster the LEDs were mainly used for work function measurements of the cathode materials, that were tested in the scope of this thesis. For the measurements at KIT the LEDs also provided the possibility of selecting the desired surplus energies of photoelectrons, by using the monochromator to adjust the photon energies to the work function of the cathode material. A detailed discussion on the UV-LED measurements at Münster can be found in chapter 7.

5.2 Optical light guides

From the experience with the predecessor electron gun optical light guides have proven to be useful to couple the laser beam into the vacuum chamber. With the use of such fibers no complicated optical setup is necessary to guide the laser beam. Hence optical light guides (model: Optran UV) were also used for the setup of the main spectrometer

5 Electron gun components

electron gun and are provided by CeramOptec GmbH (fig. 5.3). These fibers offer a high transmittance in the ultraviolet spectral range ($\sim 90\%$ at 266 nm).

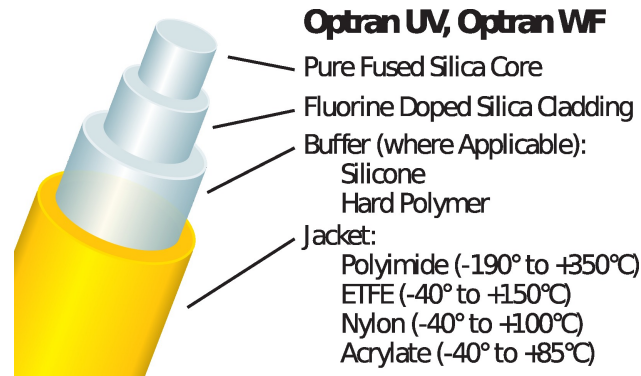


Figure 5.3: Mechanical structure of the Optran UV fiber [Cer]

The fibers are specified in a temperature range from -190°C to 350°C which makes them applicable for ultra-high vacuum (UHV) setups which generally need to be baked out. The fibers used for the test measurements have a pure fused silica core of $200\ \mu\text{m}$ diameter. The core diameter is $185\ \mu\text{m}$ larger than the diameter of the fibers used in the predecessor electron gun. The larger diameter was chosen, because the small diameter fibers broke very easily and provided only small electron rates when used with UV LED's. A larger diameter has the negative effect of broadening the angular spread σ_{θ} of the photoelectrons, because of a larger starting radius. However simulations by M. Zacher showed that the width of the angular spread of the electrons is still low enough for such core diameters [Zac14]. For the electron gun setup two different fibers are used. One fiber outside of the vacuum chamber, that guides the light from the laser to the feedthrough at the chamber and one fiber that guides the light inside the chamber. The inner fiber does not have a jacket and a buffer (fig. 5.4), that protect the fiber against mechanical stress, because the materials used for the jackets are not UHV-applicable.

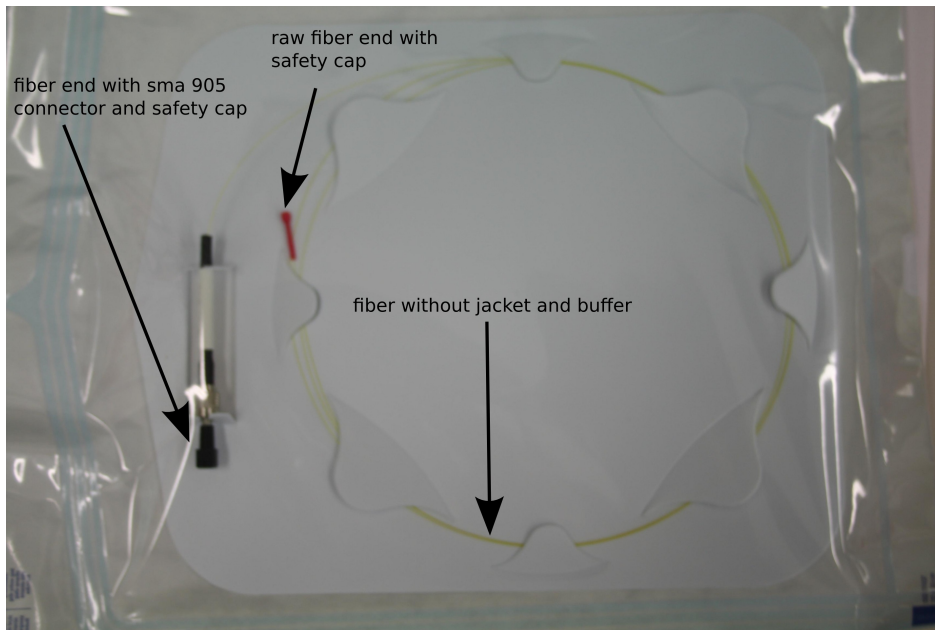


Figure 5.4: Optical light guide without jacket and buffer

5.3 Cathode materials

5.3.1 Matching cathode materials

With the laser providing photon energies of $E_{\text{ph}} = 4.66 \text{ eV}$ the work function W of the cathode material defines the electron starting-energy distribution. As cathode material only metals are possible choices because semi- or non-conducting materials would disturb the electric field of the parallel plate capacitor in an unknown manner. A list with possible cathode material candidates is shown in table 5.1.

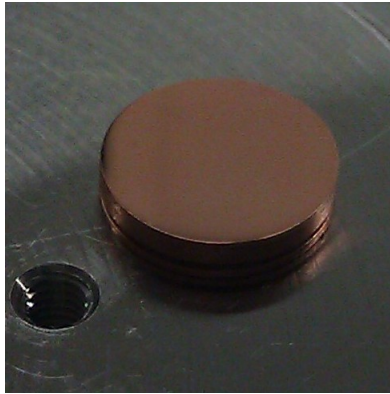
Considering the small gap ($E_{\text{ph}} - W = 0.07 \text{ eV}$) between photon energy and literature work function, a copper single crystal with surface orientation (100) from Mateck GmbH has been chosen as cathode material (figure 5.5). Using a single crystal of high purity (99.9%) and an orientation accuracy $< 2^\circ$ should secure a well defined work function, in contrast to polycrystalline materials with disordered surface orientations, that show broader work functions.

Other cathode materials such as platinum, gold and silver have also been tested in the process of this thesis, due to stray light issues in the copper single crystal setup (see 7.2). As a result the electron creation method with a back-illuminated silver vaporized fiber as used for the predecessor electron gun was successfully tested for the final setup at KIT (7.3).

5 Electron gun components

No.	material (cryst. dir.)	method	W [eV]	reference	$E_{\text{ph,laser}} - W$ [eV]
1	Au	contact pot. diff.	5.22 ± 0.05	[Hub66]	-0.56
2	Au	contact pot. diff.	4.83 ± 0.02	[And59]	-0.17
3	Au (polycryst.)	photoelectric	5.1 ± 0.1	[Eas17]	-0.44
4	Au (100)	photoelectric	5.47	[Wea81]	-0.81
5	Au (110)	photoelectric	5.37	[Wea81]	-0.71
6	Au (111)	photoelectric	5.31	[Wea81]	-0.65
8	Ag (100)	photoelectric	4.22 ± 0.04	[Che82]	0.44
9	Ag (110)	photoelectric	4.14 ± 0.04	[Che82]	0.52
10	Ag (111)	photoelectric	4.46 ± 0.02	[Che82]	0.2
11	Ag (polycryst.)	photoelectric	4.0 ± 0.15	[Eas17]	0.66
12	Cu	photoelectric	4.65 ± 0.05	[Eas17]	0.01
13	Cu (100)	photoelectric	4.59	[Wea81]	0.07
14	Cu (110)	photoelectric	4.48	[Wea81]	0.18
15	Cu (111)	photoelectric	4.94	[Wea81]	-0.28
16	Cu (112)	photoelectric	4.53	[Wea81]	0.13
17	Pt (polycryst.)	photoelectric	5.64	[Wea81]	-0.98
18	Pt (110)	field emission	5.84	[Wea81]	-1.18
19	Pt (111)	field emission	5.93	[Wea81]	-1.27
20	Pt (320)	field emission	5.22	[Wea81]	-0.56
21	Pt (331)	field emission	5.12	[Wea81]	-0.46
22	W (polycryst.)	contact pot. diff.	4.55	[Wea81]	0.11
23	W (100)	field emission	4.63	[Wea81]	0.03
24	W (110)	field emission	5.22	[Wea81]	-0.56
25	W (111)	field emission	4.45	[Wea81]	0.21
26	W (113)	field emission	4.46	[Wea81]	0.2
27	W (116)	therm. emission	4.32	[Wea81]	0.34
28	stainless steel		4.4 ± 0.2	[Pic92]	0.26
29	stainless steel	photoelectric	4.75	[Wal09]	-0.09
30	stainless steel	photoelectric	$4.35 - 4.55$	[Wal09]	$0.11 - 0.31$

Table 5.1: **Work function literature values for selected metals:** The literature values were obtained by different measurement methods, being: photoelectric, contact potential difference, thermionic emission and field emission measurements. In the last column the difference between the laser photon energy $E_{\text{ph}} = 4.66$ eV and the literature work function value is given. Highlighted are the three cathode materials that were used in the electron gun measurements.

Figure 5.5: Copper(100) single crystal ($d = 10$ mm)

5.3.2 Work function of metals

The work functions of potential cathode materials for the electron gun have a large impact on the energy distribution of the electron starting energy E_{start} (section 4.2.1). Therefore a fundamental understanding of the effects that contribute to deviations from literature work function values to work function values measured in the scope of this thesis, shall be given.

The work function W is the minimum energy needed to remove an electron from a solid. It is defined as the difference between Fermi energy E_F and vacuum level W_S :

$$W = W_S - E_F \quad (5.1)$$

The Fermi energy E_F is the highest energy that a fermion can have in a Fermi gas at 0 K. In the case of metals the Fermi gas consists of electrons. According to the Fermi-Dirac distribution, for temperatures above 0 K energy states above the Fermi energy can be occupied. The Fermi-Dirac distribution describes the probability that an energy level is occupied by a Fermion in a system in thermodynamic equilibrium:

$$f(E) = \frac{1}{\exp\left(\frac{E-\mu}{k_B T}\right) + 1} \quad (5.2)$$

Here μ is the chemical potential, E the energy for a single particle state and $k_B T$ the thermal energy. For $T = 0$ K, the chemical potential μ is equal to the Fermi energy E_F . As the absolute temperature T goes higher, states with energies $E > E_F$ are occupied (fig. 5.6). Therefore the Fermi gap gets smeared out, so already photons with energies below the work function can excite a few electrons to the vacuum. This leads to a temperature dependent broadening of the electron starting energy distribution σ_E .

An elementary theory of the effect of temperature on the work function of metals was developed by R. H. Fowler [Fow31]. The core assumption of the theory is that the number of electrons emitted per quantum of light absorbed is proportional to the number

5 Electron gun components

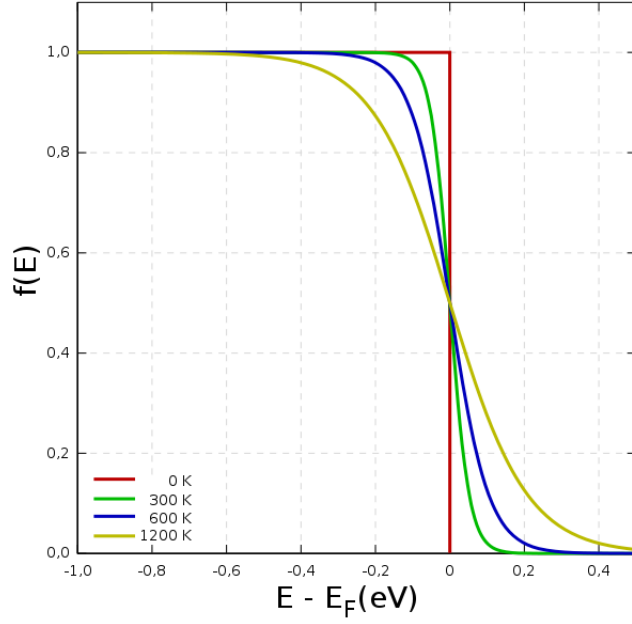


Figure 5.6: **Fermi distribution for different temperatures** Figure taken from [Wik]

of electrons per unit volume of the metal with a kinetic energy normal to the surface augmented by incident light that is sufficient to overcome the potential step at the surface. This number can be derived as follows. In a Fermi gas the density of states is given by:

$$D(E) = \frac{(2m)^{\frac{3}{2}} \cdot \sqrt{E}}{4\pi^2 \hbar^3} \quad (5.3)$$

With (5.2) the number of electrons per unit volume having velocity components in the ranges $u, u + du, v, v + dv$ and $w, w + dw$ (u normal to the surface) can be given by:

$$n(u, v, w) du dv dw = 2 \left(\frac{m}{h}\right)^3 \frac{du dv dw}{e^{\{\frac{1}{2}m(u^2+v^2+w^2)-E_F\}/k_B T}} \quad (5.4)$$

Then the number of electrons per unit volume with velocity component normal to the surface in the range of $u, u + du$ is given by:

$$\begin{aligned} \bar{n}(u) du &= 2 \left(\frac{m}{h}\right)^3 du \int_0^\infty \int_0^{2\pi} \frac{\rho d\rho d\theta}{e^{\{\frac{1}{2}m(u^2+\rho^2)-E_F\}/k_B T}} \\ &= \frac{4\pi k_B}{m} \left(\frac{m}{h}\right)^3 \ln \left\{ 1 + e^{(E_F - \frac{1}{2}mu^2)/k_B T} \right\} du \end{aligned} \quad (5.5)$$

5.3 Cathode materials

According to the core assumption only electrons with a velocity that fulfill $\frac{1}{2}mu^2 = W_s - h\nu$ can escape from the metal. Therefore the number of available electrons N_B that can escape is:

$$N_B = \int_{\frac{1}{2}mu^2=W_s-h\nu}^{\infty} \bar{n}(u)du \quad (5.6)$$

The approximate solution of the integral is given with $(h\nu - W)/k_B T = \mu$ (for details see paper):

$$\begin{aligned} N_B &= \frac{2\sqrt{2\pi m^{\frac{3}{2}}}}{h^3} \frac{k_B^2 T^2}{(W_S - h\nu)^{\frac{1}{2}}} \left[e^\mu - \frac{e^{2\mu}}{2^2} + \frac{e^{3\mu}}{3^2} + \dots \right] \text{for } \mu \leq 0 \\ N_B &= \frac{2\sqrt{2\pi m^{\frac{3}{2}}}}{h^3} \frac{k_B^2 T^2}{(W_S - h\nu)^{\frac{1}{2}}} \left[\frac{\pi^2}{6} + \frac{1}{2}\mu^2 - \left(e^{-\mu} - \frac{e^{-2\mu}}{2^2} + \frac{e^{-3\mu}}{3^2} \right) \right] \text{for } \mu \geq 0 \end{aligned} \quad (5.7)$$

From the number of available electrons N_B that can be transmitted, it is possible to derive the photoelectric current I per quantum light absorbed with the plausible assumption that $N_B \sim I$. Further assuming that $(W_S - h\nu)^{\frac{1}{2}}$ is in first approximation constant one gets:

$$\frac{I}{T^2} = A \cdot f(\mu) \quad (5.8)$$

with:

$$\begin{aligned} f(\mu) &= \left[e^\mu - \frac{e^{2\mu}}{2^2} + \frac{e^{3\mu}}{3^2} + \dots \right] \text{for } \mu \leq 0 \\ f(\mu) &= \left[\frac{\pi^2}{6} + \frac{1}{2}\mu^2 - \left(e^{-\mu} - \frac{e^{-2\mu}}{2^2} + \frac{e^{-3\mu}}{3^2} \right) \right] \text{for } \mu \geq 0 \end{aligned} \quad (5.9)$$

Whereas $f(\mu)$ is the Fowler function. Taking the logarithm of (5.8) the final expression is given by:

$$\ln \frac{I}{T^2} = B + \ln f(\mu) \quad (5.10)$$

The constant B is independent of temperature and frequency. This expression can be used to determine the temperature dependent work functions of metals.

The cause of further work function deviations from literature values can be explained by studying the contribution of W_S to the work function. The vacuum level W_S is the energy of a resting electron with enough distance to the metal surface, so that the electrostatic

force on the electron can be neglected. W_S directly depends on the charge density near the surface of the metal. For an undisturbed charge density on the crystal surface one obtains $W_S = 0$. This would only be true if the charge density near the surface would be equal to the charge density inside the crystal. But the broken symmetry of the crystal lattice at the surface leads to a non-neglectable surface electric dipole (electric double layer) at the surface (figure 5.7). [Ash13]

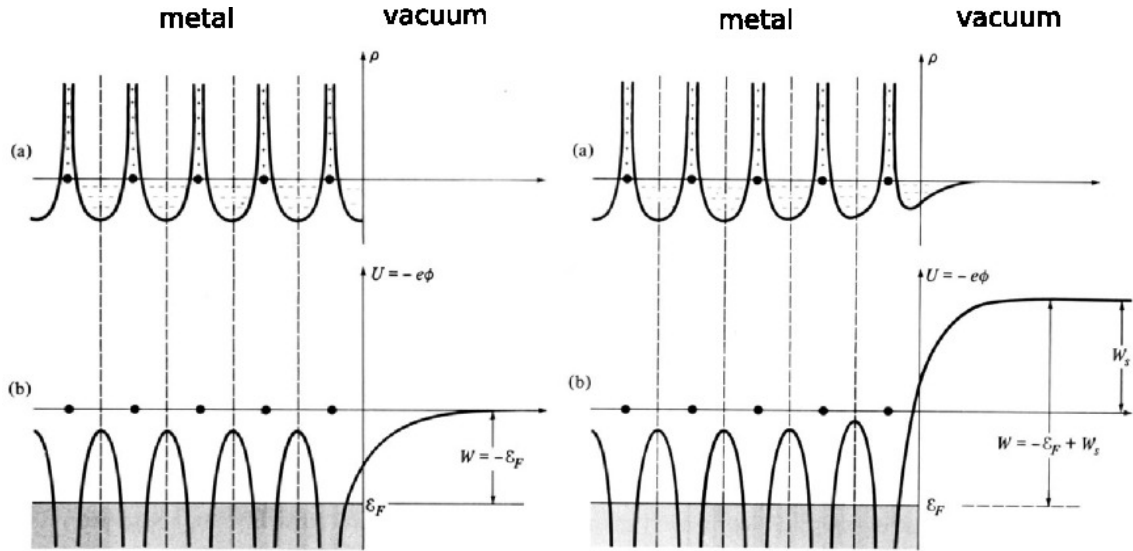


Figure 5.7: **Electric charge density and crystal potential.** On the left for the undisturbed case and on the right for the disturbed case. a) shows the progression of the charge density and b) shows the progression of the crystal potential (figure taken from [Ash13])

The asymmetry of the charge density near the surface is strongly dependent on the surface properties. This is why the work functions for various surface orientations of the same metal differ from each other.

Additional causes for asymmetries of the surface charge densities can be the presence of an adsorbate that influences the dipole layer at the crystal surface. The resulting work function shift then depends on the magnitude and the orientation of the effective dipole moment of the adsorbate. This effective dipole moment consists of a possible permanent dipole (if the adsorbate carries an own dipole) and an induced dipole (through charge transfer between adsorbate and solid). Depending on the orientation of the effective dipole moment, the work function can increase ($\Delta W > 0$) or decrease ($\Delta W < 0$) [Hen94].

For the electron gun setup the installation of the cathode material had to be conducted in atmospheric conditions. Hence adsorbates on crystal surface have to be taken into account. In our case the two most probable adsorbates to play a role in disturbing the surface charge density are oxygen (under atmospheric conditions) and hydrogen (in the residual gas of the vacuum setup).

In [She92] the changes of the work function of Pt(110) caused by the adsorption of hydrogen and oxygen has been reported. Dependent on the hydrogen dosage the work function changed from $\Delta W > 0$ (low dosage) to $\Delta W < 0$ (high dosage). In the case of oxygen the work function change was always $\Delta W > 0$. For hydrogen the maximum positive work function change amounts to 0.15 eV and the maximum negative change was -0.65 eV (both at $T = 170$ K crystal temperature).

The conditions of the electron gun setup differ from the ones in the cited paper. Nevertheless does it show that adsorbates can have a large impact on the work function of a metal. For the setup the amount of adsorbate contamination is unknown. As seen in the work function measurements and with the stray light problem, described in chapter 7, large deviations from the literature values could be observed. This is plausible since the literature values of the work functions are attained by extensive surface preparation, in order to avoid the surface effects described before.

The surface preparation in such measurements is usually done via bake out and ion bombardments. The bake out temperature for the electron gun is limited to $T = 150$ °C, which is the maximum bake out temperature of the piezo actuators used in the setup that are described in the next chapter. With this temperature limit it can not be expected to remove all adsorbates on a cathode material. For an ion bombardment the electron gun would need to be equipped with an ion source which would have been difficult to implement. Hence such surface preparations were not integrated for the electron gun setup.

5.4 Electron gun positioning

Flux tube positioning In the region of the flux tube where the electron gun will be mounted at the KATRIN main spectrometer, the magnetic field is inhomogeneous. To be able to cover the whole flux tube of 191 Tcm^2 the electron gun has to be movable to reach the outermost field lines of the flux tube.

Therefore the electron gun was mounted on the bellows of the former pre-spectrometer UHV manipulator of the KATRIN experiment (figure 5.8). The maximum bend angle of the bellows is limited to $\pm 23^\circ$ for the polar angle. Considering the limitation of $\pm 23^\circ$ it was necessary to investigate, if the angular range is sufficient to cover the whole flux tube. The simulation results on that topic can be found in section 6.2.

The exact knowledge of the electron gun position on the flux tube is a crucial prerequisite for understanding the measurement results. Therefore the manipulator has been refurbished and modified in the scope of the bachelor thesis by L. Josten [Jos13]. Thus a readout precision of approximately 0.001° for horizontal and vertical bend angle is reached. The absolute zero position of both axes can be determined with an accuracy of approximately 0.01° .

Electron gun rotation The parallel plate capacitor of the electron gun has to be rotatable in order to set the angle α between electric and magnetic field. This is done

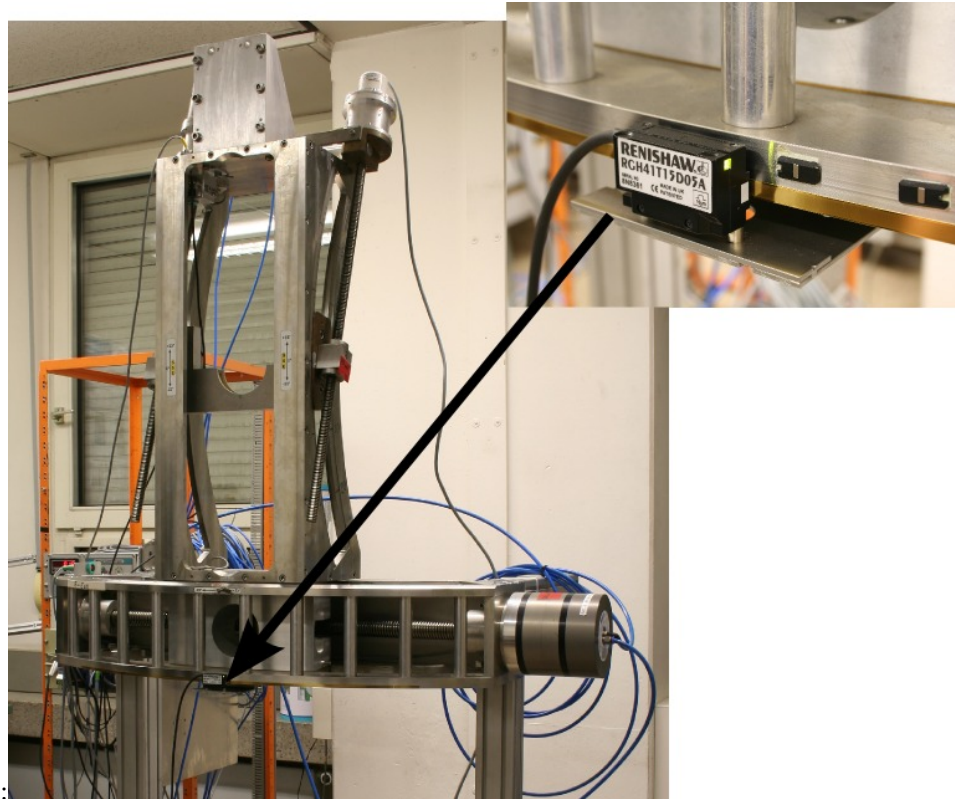


Figure 5.8: **UHV manipulator setup at Münster:** UHV manipulator with highlighted position sensor of the horizontal axis

by two piezo actuators from the company Attocube (ANR240). These special actuators can be used under UHV conditions (up to $5 \cdot 10^{-11}$ mbar) and also work undisturbed in magnetic fields. The actuators have been purchased in the version of rotators. They provide high precision positioning as well as high precision absolute position readout (resolution of 1 m° for both).

The working principle of the travel mechanism is called slip-stick motion. The table that is to be moved is clamped to a guiding rod. The guiding rod itself is connected to a piezo electric ceramic (figure 5.9). The first step in the picture shows the actuator at rest. Applying a voltage to the piezo element causes it to expand. This leads to an acceleration of the guiding rod. For the slip part of the motion (step 1-2), the voltage has to be increased to its maximum in a very short time interval (microseconds). In this manner the rod gains enough kinetic energy to overcome the static friction between the rod and the table that is clamped to it. Through its inertia the table remains nearly nondisplaced while the rod moves. In step 2-3 the stick motion takes over. The voltage applied to the piezo element is slowly decreased over time, so the piezo element slowly contracts to its initial position. The attached rod therefore also moves back to its initial position. This time the rod does not have enough kinetic energy to overcome the static friction so that the table moves along with the rod. The step is now completed.

Repeating this cycle periodically leads to a step-by-step motion of the clamped table in one direction. [Att]

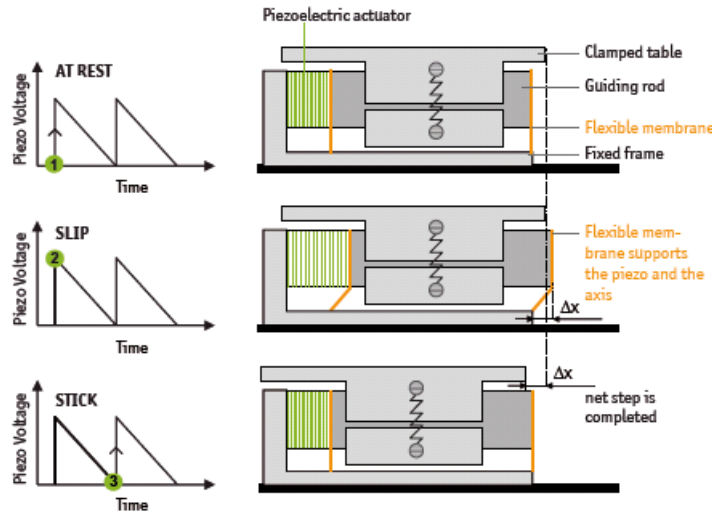


Figure 5.9: **Working principle of the piezo rotators:** From top to bottom are three different stages of one actuator step shown. On the left the corresponding voltage stages are shown. (figure taken from [Att])

The downside of using these piezo actuators is the low maximum load of 200 g and the low maximum dynamic torque of 2 Ncm. For that reason the mass of the stainless steel enclosure of the parallel plate capacitor and its interior had to be minimized. To further lower the load and the dynamic torque that is needed to rotate the enclosure, the rotators have been suspended to the center of mass of the hole enclosure. The suspension was realized with a gimbal mount on two orthogonal axes on the back lid of a stainless steel enclosure (see section 5.5). With this kind of suspension it had to be taken into account that the point of rotation should coincide with the emission point. If the rotation point would be on any other axis in the chamber, the rotation of an angle α would set the e-gun on another field line of the flux tube than the one at $\alpha = 0^\circ$ (see figure 5.10). Since different angles θ_{solenoid} on single field lines are investigated with the electron gun this effect would complicate the analysis.

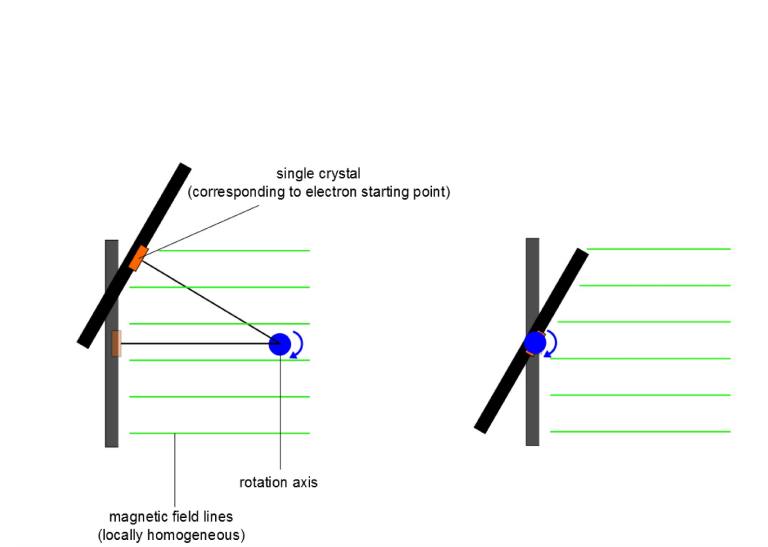


Figure 5.10: **Influence of the rotation axis position on the position in the flux tube**
left: rotation axis and substrate are not in the same plane *right:* rotation axis and substrate are in the same plane

5.5 Electron gun assembly

The parallel plate capacitor of the electron gun is mounted to the back lid of the stainless steel enclosure (figure 5.11). Around the enclosure is the gimbal mount for the piezo rotators. The whole enclosure is mounted to a CF160 flange on the back of the electron gun vacuum chamber.

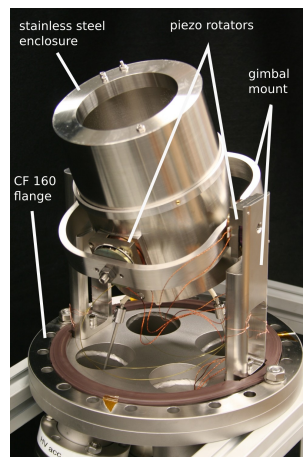


Figure 5.11: **Electron gun stainless steel enclosure mounted on the CF160 flange**

The flange features 4 feedthroughs, two for the electrical feedthroughs for the HV connection of the electrodes, one for the power supply of the piezo rotators and one optical feedthrough for the laser/LED light. As all the feedthroughs are mounted on the flange,

the electron gun can be easily accessed for maintenance and setup changes. A CAD drawing of the chamber with the enclosure is shown in figure 5.12.

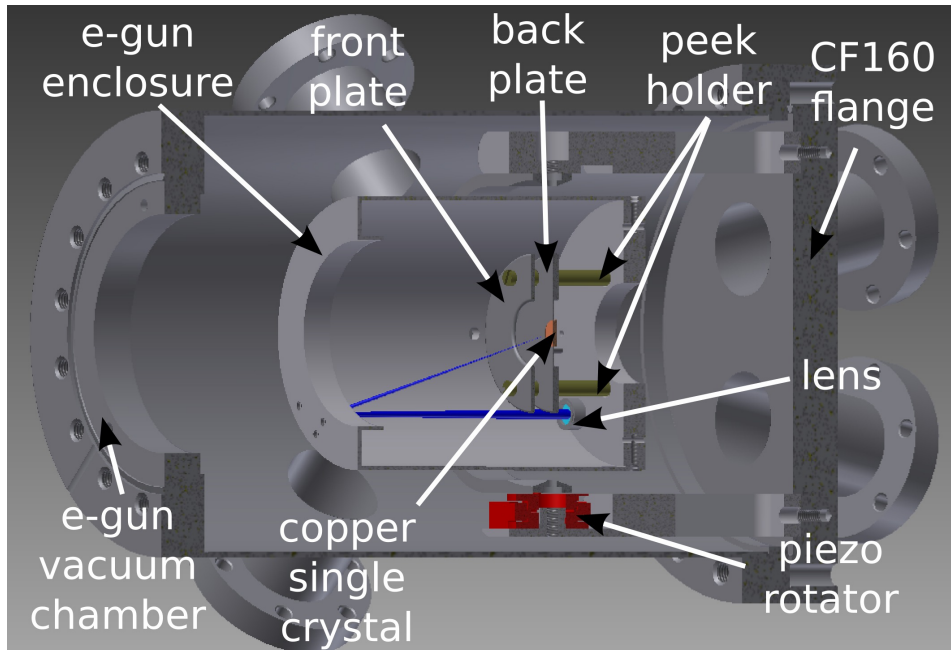


Figure 5.12: **Assembly of the electron gun in the vacuum chamber.**

The use of the stainless steel enclosure around the parallel plate capacitor ensures an invariant electric field inside the enclosure for any rotation angle α of the electron gun. The electrodes are rounded to prevent potential discharges that can occur on sharp edges. Parameters like electrode plate thickness, plate size, distance between the plates, plate distance to the surroundings and the size of the aperture of the front plate were optimized in simulations conducted by M. Zacher which will be presented in his upcoming doctoral thesis [Zac14]. The plate diameters were determined to $d = 60$ mm to provide a homogeneous electric field in the electron starting region. The electrodes are mounted to PEEK holders that insulate the plates electrically from each other and from the enclosure (figure 5.13).

The copper single crystal is mounted in the center of the back plate. To create electrons on the crystal surface the laser beam is focused onto the crystal. The optical setup inside the vacuum chamber consists of the vacuum fiber that guides the laser beam to a lens that collimates the beam and a spherical mirror that reflects and focuses the light onto the center of the single crystal. With this setup spot sizes of approx. 1 mm could be achieved.

For the alternative illumination method that was also used in the final setup, an optical fiber is then glued into the center of a small stainless steel plate. A 40 nm silver layer is then vaporized onto front of the plate with the fiber. The fiber is then mounted to the center of the back plate instead of the copper single crystal. The silver layer is illuminated from the back thus creating photoelectrons that can leave the silver layer

5 Electron gun components

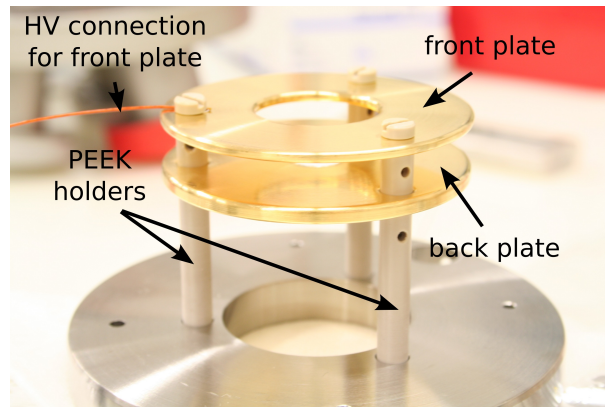


Figure 5.13: Insulated back and front plate

on the front side. The electrons are then accelerated by the potential difference between back and front plate ΔU . Besides the smaller starting radius of electrons compared to the front illumination, the centering of the electron starting position is much easier to achieve since no optical components besides the fiber have to be used inside the electron gun vacuum chamber (see figure 5.14).

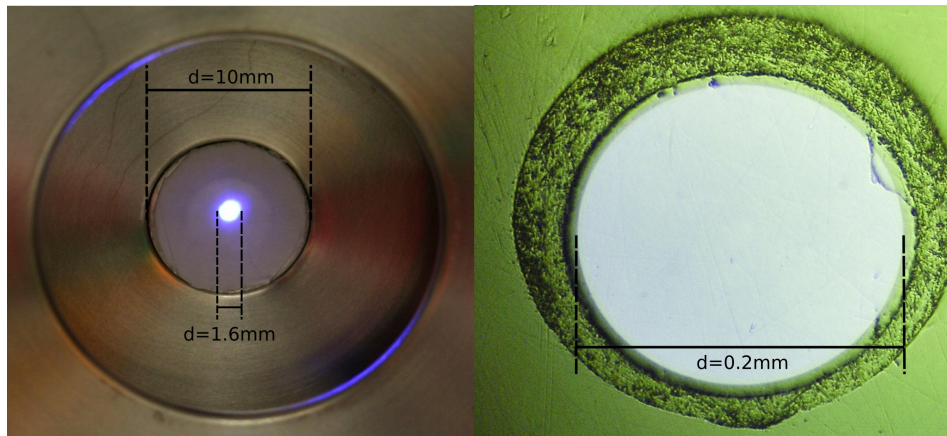


Figure 5.14: **Difference between electron starting radii:** *left:* laser spot size ($d = 1.6$ mm) and center (front illumination) *right:* back illumination of optical fiber with substrate (spot size $d = 0.2$ mm)

6 Simulations

6.1 Simulation tools

The first part of this chapter will give a short overview of the simulation tools available for the electron gun design.

Kassiopeia For electron tracking as well as simulating the electric and magnetic fields inside a static geometry, a software package called Kassiopeia was used. This simulation software was developed by the KATRIN collaboration over the last years. This tool was designed to cover all the different simulation aspects needed in the KATRIN experiment such as electromagnetic field calculations, particle trajectory calculations with machine precision, as well as various visualization techniques for analysis. The Kassiopeia code is partially based on older simulation tools used beforehand in the collaboration.

This thesis will not go into further details of the Kassiopeia software, since the electron tracking simulations were conducted by M. Zacher and are therefore part of his upcoming dissertation. For further information on the Kassiopeia software see reference [Beh12].

Magfield2 As part of this thesis several magnetic field calculations were performed to secure that the e-gun can cover the whole flux tube of the main spectrometer. For this purpose a program package called magfield2 by F. Glück was used, which later also was implemented into the Kassiopeia package.

With magfield2 magnetic fields and vector potentials of an axially symmetric coil system can be computed. This is suitable for the KATRIN main spectrometer, as it has an axially symmetric coil configuration. To calculate the magnetic fields, that are generated by the electric current in the coils, the Biot-Savart law is used:

$$d\vec{B} = \frac{\mu_0 I d\vec{l} \times \hat{r}}{4\pi r^2} \quad (6.1)$$

Magfield2 then uses two different methods for field computation:

- The first method makes use of elliptic integrals for high accuracy magnetic field calculations. However this method has rather high computation time, which is why method two is generally used to calculate magnetic fields.
- In method two the Legendre polynomial expansion is used. This method has much lower computation times at the cost of accuracy.

6 Simulations

The magfield2 program package has already been discussed in detail in references [Hug08], [Val04] and [Vöc08], wherefore it will not be discussed further in this thesis.

6.2 Simulation results

In this part, the simulation results of the magnetic field calculations are presented. As mentioned before, a crucial part of the e-gun functionality is to cover the whole flux tube of 191 Tcm^2 for the standard settings of the main spectrometer magnets (magnet center position on z-axis: $c_{\text{sol}} = -12.104 \text{ m}$; magnetic field strength $B_{\text{sol}} = 4.5 \text{ T}$). This was investigated with the following simulations.

After determining the e-gun chamber properties, as presented in the previous chapter, the distance from the electron starting position to rotation center ($b = 1.205 \text{ m}$) and the distance between rotation center to the spectrometer magnet center ($a = 0.3949 \text{ m}$) was known as shown in the CAD drawing (figure 6.1). The figure also shows a schematic

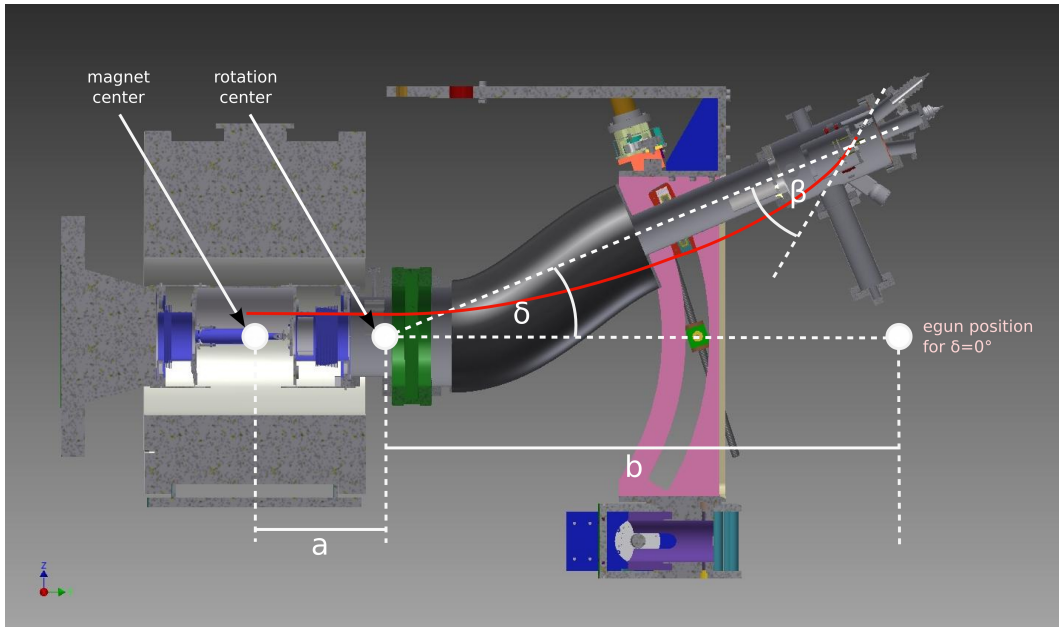


Figure 6.1: **Cad drawing of e-gun setup at the KATRIN main spectrometer:** The white sketches highlight the significant parameters for the simulations. In red an exemplary magnetic field line (not simulated) is shown for illustration purposes.

magnetic field line (red), the rotation angle $\delta = 23^\circ$ of the UHV manipulator and the angle between electric and magnetic field β at the electron starting position. In the figure it becomes clear that in an inhomogeneous magnetic field the set angle of the electron gun chamber $\alpha = 0^\circ$ is not identical with the angle β between electric and magnetic field for manipulator angles $\delta > 0^\circ$. This had to be taken into account for the setup, since the electron gun angle α is limited. The simulations are based on the assumption of a maximum electron gun angle $\alpha_{\text{max}} = \pm 10^\circ$, since the limit for the final setup of 15° was

not in the design at the time when the simulations were conducted. In the simulations it was checked if the angles $\delta_{\max} = 23^\circ$ for the UHV manipulator and the angle α_{\max} would be sufficient for this setup configuration.

The standard settings for the main spectrometer entrance magnet have been used, as it is intended in the measurement phase of the KATRIN experiment. In order to investigate if the requirements of the electron gun are met in this scenario, the outer field lines have to be investigated, since the manipulator angle δ as well as the angle between electric and magnetic field lines β are highest there. Taking the rotation symmetry into account, it is only necessary to regard the outermost field lines in one direction. Furthermore two scenarios of the flux tube coverage have been investigated. The minimum requirement of the e-gun which is covering the flux tube of 191 Tcm^2 in measurement mode of the spectrometer and the best-case scenario which is if the e-gun could also cover the most outer field lines closest to the earth and anti-penning electrodes, being the outermost possible trajectory for electrons in the main spectrometer. Figure 6.2 shows the two field lines for minimum requirement and for the best-case scenario.

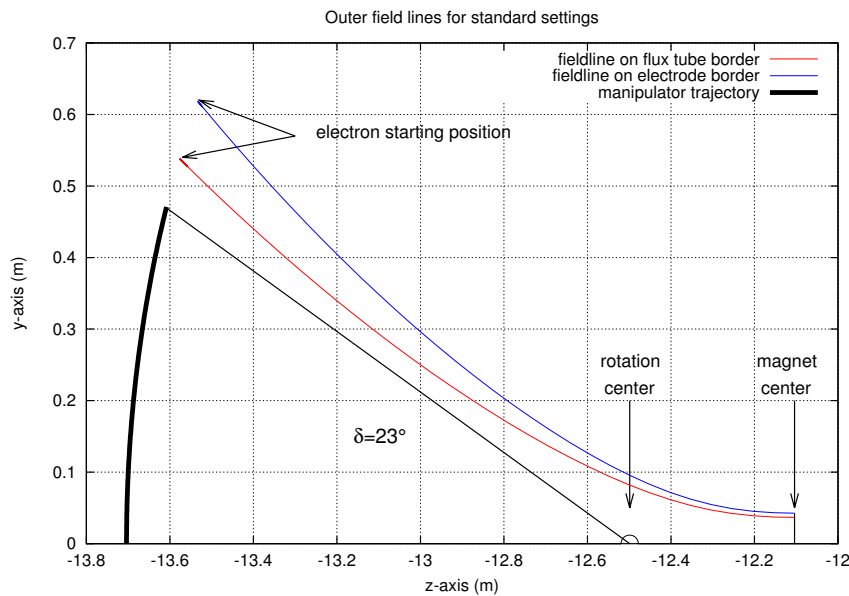


Figure 6.2: **Magnetic field lines for minimum requirement and best-case scenario:** For the simulation the standard magnet setting of 4.5 T was used. In red is the outermost field line of the flux tube of 191 Tcm^2 (minimum requirement) and in blue for the outermost trajectory of an electron in the KATRIN main spectrometer (best case scenario). The thick black line shows the manipulator trajectory up to $\delta = 23^\circ$. Also depicted are the magnet center and the rotation center positions.

In conclusion this scenario does not meet the desired flux tube coverage as the maximum manipulator angle $\delta_{\max} = 23^\circ$ is exceeded by $\Delta_{\text{flux}} = 3.54^\circ$ and $\Delta_{\text{electrode}} = 7.87^\circ$ for the investigated field lines. Hence some setup changes had to be taken into consideration so that the requirements could still be met.

First investigations focused on different distances a and b (fig. 6.1). Considering that

6 Simulations

the field lines fan out with greater distance to the magnet center only smaller distances for a and b have to be considered. In figure 6.3 the impact of various distances b is shown. For better comparability the two field line borders are also depicted in the plot.

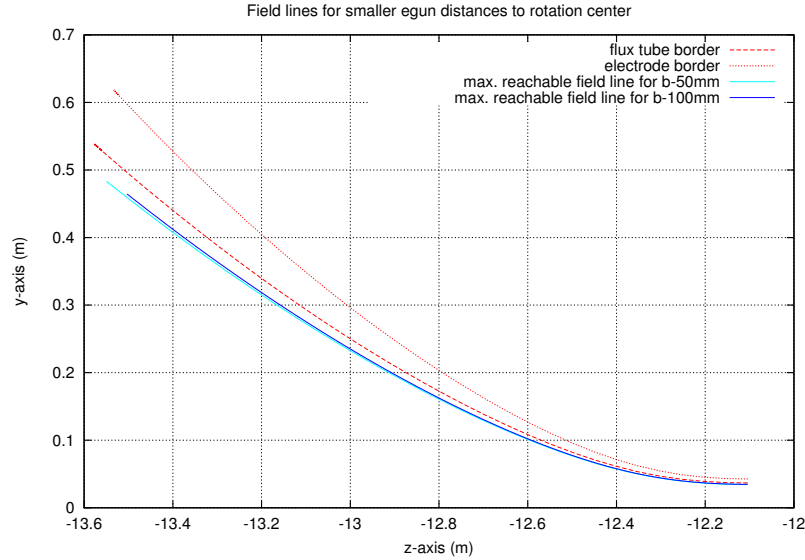


Figure 6.3: **Field lines for two different distances b :** The maximum reachable field lines are shown for two different distances b in cyan and blue (solid). The red field lines (dashed) represent the field lines the electron gun needs to reach.

The plot shows that the closer the electron starting position is to the rotation center, the smaller the maximum rotation angle of the UHV-manipulator has to be. In the two scenarios the electron gun does not reach the outer field lines. Lowering distance b brings the electron gun into a region of smaller flux tube width so that lower angles to reach the outer field lines are needed but at the same time the shortened lever arm limits the effect since the total path traveled over the angle δ is also shorter.

Lowering distance a has a much larger effect on the maximum angle δ needed to reach the outer field lines (fig. 6.4). Lowering the distance by 50 mm is sufficient to cover the whole flux tube of 191 Tcm^2 , 200 mm are sufficient to cover even the outermost field lines in the main spectrometer. However this method is difficult to realize because of the limited space between magnet center and UHV manipulator, since the parts like the valve of the main spectrometer are mounted in between. For setting up the electron closer to the magnet center it has also to be taken into account that the magnetic field strength in the electron gun region is higher with the consequence that the influence of the electric field on the angle θ_{ad} is smaller (reminder: θ_{ad} is the angle between electric and magnetic field when the adiabatic motion takes over). Hence the angular range of θ_{solenoid} up to 90° can not be reached if the electron gun is set up too close to the entrance magnet center. Detailed simulations on this topic will be presented in [Zac14]. In conclusion this method was discarded.

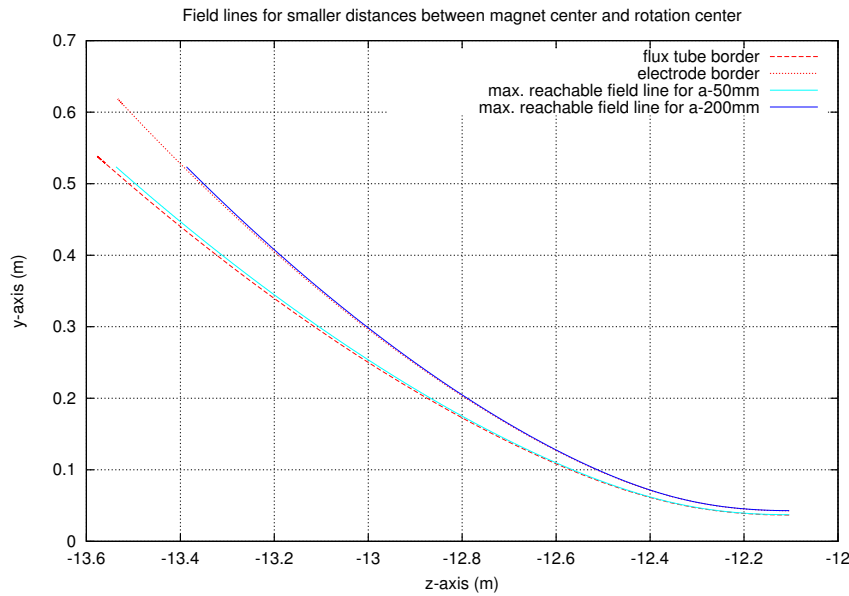


Figure 6.4: **Field lines for two different distances a :** The maximum reachable field lines are shown for two different distances a in cyan and blue (solid). The red field lines (dashed) represent the field lines the electron gun needs to reach.

Another parameter that can be modified is the shape of the magnetic field in the electron gun region. The possibility to use the pre-spectrometer magnet to shape the magnetic field has been investigated. By placing the magnet behind the electron gun setup the magnetic field is bent as shown in figure 6.5. The field line is bent down far enough for the electron gun to reach it.

In order to find optimum settings for magnetic field strength and position of the pre-spectrometer magnet further simulations have been conducted. Bending the field lines also changes the angle between electron gun and magnetic field for the different positions on the flux tube (angle β in figure 6.1). This effect has to be taken into account, as the electron gun has to be able to set angles β from 0° and 10° to cover angles θ_{solenoid} from 0° to 90° for every field line of the flux tube. If the magnetic field lines are bent too far, the angle β can be greater than 10° for an electron gun angle of $\alpha = 0^\circ$ on the outer field lines. Thus a setting of $\beta = 0^\circ$ would be impossible. In the simulations presented in figure 6.6 this has been investigated. Different pre-spectrometer magnetic field strength settings have been scanned in dependence of the pre-spectrometer magnet center distance to the main spectrometer magnet center on the same symmetry axis. The box in the figure depicts the angular limitations of the electron gun setup. Only a few settings are within the allowed region. Based on these simulations the pre-spectrometer magnet has been set up in a distance $d_{\text{prespec}} = 3.4\text{ m}$ from the main spectrometer magnet (center to center) with a proposed field strength of $B = 3\text{ T}$. With this setting the maximum rotation angle for the electron gun is $\alpha = 8.80^\circ$ and the maximum UHV-manipulator angle is $\delta = 22.78^\circ$. Taking the final limit of $\alpha_{\text{max}} = 15^\circ$ into account shows that even more settings are viable for the prespectrometer magnet.

6 Simulations

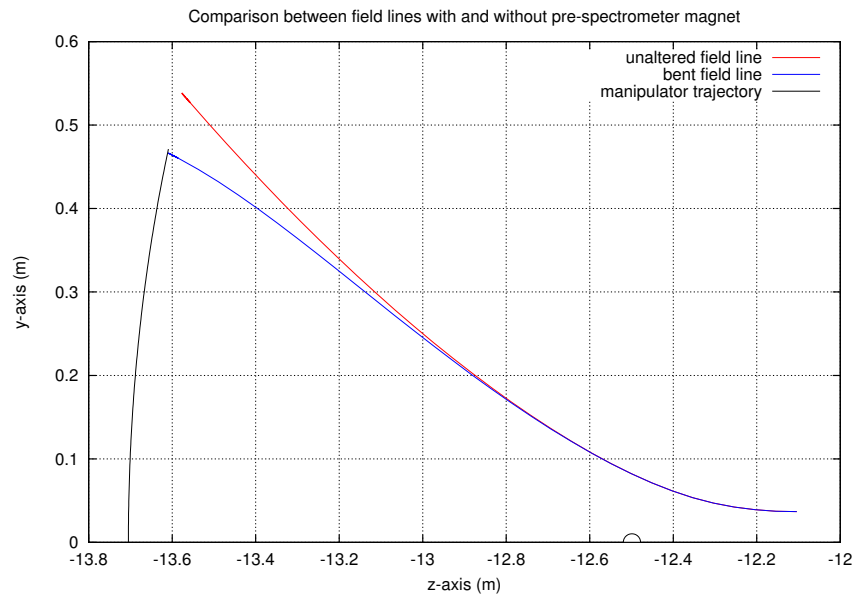


Figure 6.5: **Impact of an additional magnet behind the electron gun setup:** The field line is bent down far enough that the manipulator can reach it.

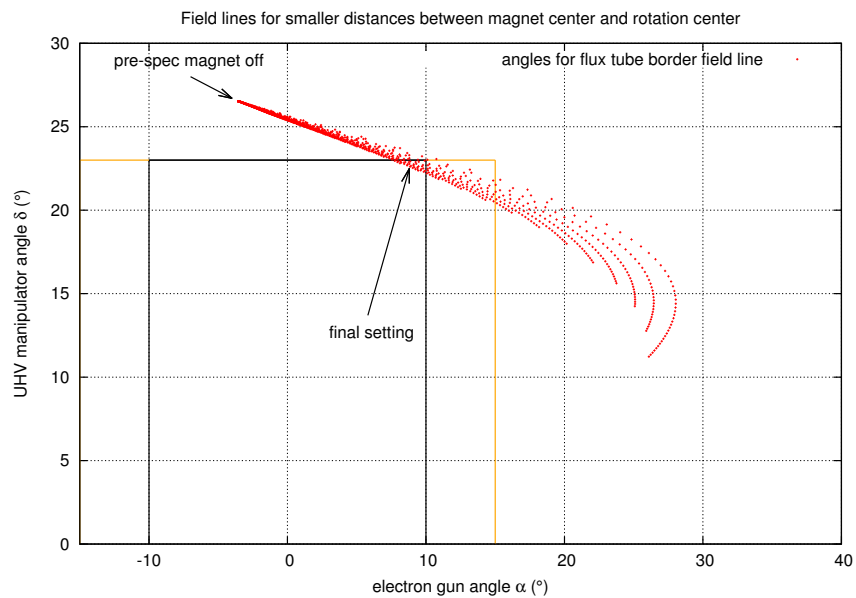


Figure 6.6: **Scan of possible pre-spectrometer settings:** The parameters distance from main spectrometer magnet d_{prespec} and magnetic field strength B have been varied. The black box shows the angular limitations of $\alpha_{\max} = 10^\circ$ and $\delta_{\max} = 23^\circ$ for the electron gun setup. Only points inside the box represent viable settings. The orange border is for the final limit of $\alpha_{\max} = 15^\circ$.

7 Electron gun test measurements

To investigate important properties of the electron gun a test setup has been constructed. The setup is based on a similar principle as the KATRIN setup, allowing to measure transmission functions and to prove angular selectivity. All of the measurements presented in this thesis were conducted together with Michael Zacher, who will also present some of the data in his doctoral thesis.

7.1 Test setup

7.1.1 Principle

The test setup features two magnets in combination with a retarding electrode proposed by B. Monreal of the KATRIN collaboration. A schematic of the setup is shown in figure 7.1.

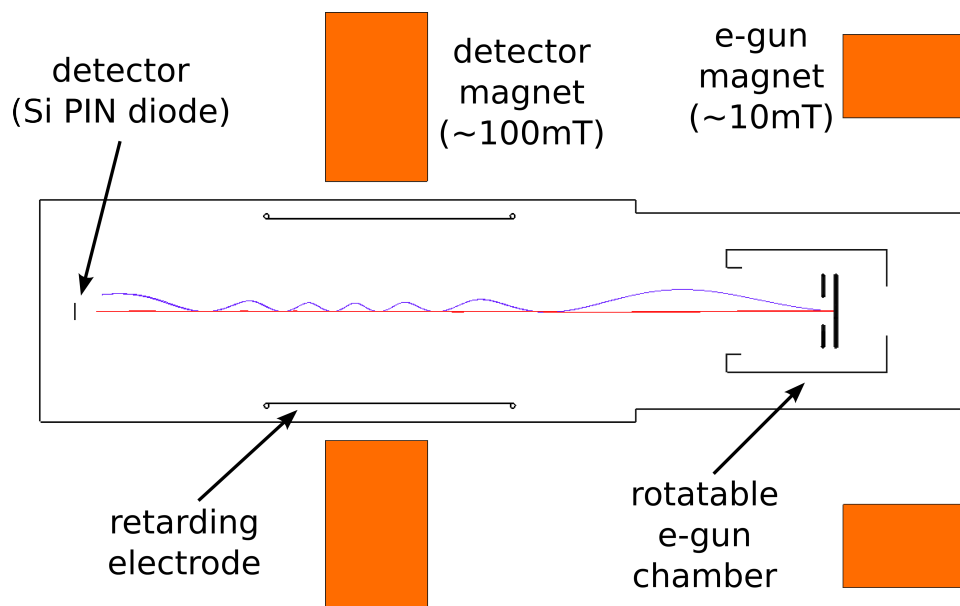


Figure 7.1: **Schematic of the Münster test setup:** The electrons are adiabatically guided from low magnetic field into higher magnetic field. With the addition of a retarding potential electrons can be magnetically mirrored in dependence of the electron gun angle α . Non rejected electrons are guided to the detector by the magnetic field of the detector magnet.

7 Electron gun test measurements

The electrons start in the magnetic field of the electron gun magnet (approx. $B_{\text{egun}} \approx 10 \text{ mT}$) and are guided adiabatically into a higher magnetic field of the detector magnet ($B_{\text{det}} \approx 100 \text{ mT}$). The transition from low magnetic field into higher magnetic field causes the angle θ_{ad} (angle when the adiabatic motion takes over) relative to the magnetic field to rise according to equation (4.3):

$$\frac{\sin^2(\theta_{\text{ad}})}{B_{\text{ad}}} = \frac{\sin^2(\theta_{\text{det}})}{B_{\text{det}}} \quad (7.1)$$

Simulations by M. Zacher showed that with the maximum rotation angle $\alpha = \pm 15^\circ$ the electrons have a maximum angle of $\theta_{\text{ad}} \approx 15^\circ$ when they reach the position of $U \approx 0$ [Zac14]. With equation (7.1) the maximum electron angle at the highest magnetic field is $\theta_{\text{det,max}} \approx 55^\circ$. With an additional retarding potential the longitudinal energies E_{\parallel} of the electrons decrease, which leads to higher angles θ_{det} . Hence magnetic reflection of electrons $\theta_{\text{det,max}} \geq 90^\circ$ can be achieved depending on the retarding potential U_{ret} . The electrons that are not rejected are guided to the detector by the magnetic field of the detector magnet.

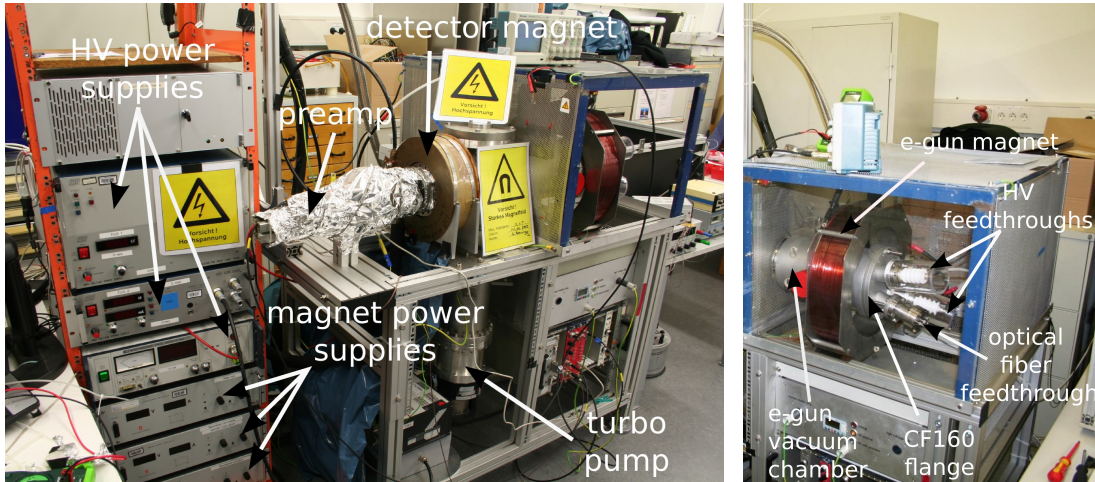
A transmission function is measured by measuring electron rates for different retarding potentials U_{ret} and fixed settings for the backplate potential U_{start} , the e-gun angle α and the potential difference ΔU between the plates. To prove angular selectivity transmission functions are measured for different starting angles α . For angular selectivity the analysis of the measured transmission functions then should result in a plot as previously shown in figure 4.2.

7.1.2 Hardware

For the test measurements the electron gun was mounted to the vacuum test stand in Münster. The whole setup can be seen in figure 7.2. The two magnets are aligned to the symmetry axis of the test setup. The pressure in the vacuum chamber was in the region of $p \approx 1 \cdot 10^{-7} \text{ mbar}$ for all measurements presented in the next section.

Data acquisition The detector used in the setup for the test measurements is a windowless 18x18mm Si-PIN diode (Hamamatsu S3204-06) mounted on a CF40 flange with a BNC feedthrough. A CoolFET preamplifier (AmpTEC A250CF) is attached to the BNC feedthrough. The main amplification is performed by a CAEN N968 spectroscopy amplifier. The amplified signal is then analyzed by a FastComTech MCA-3 ADC. The detector power is provided by an ISEG NHQ 224M power supply. The bias voltage in the presented measurements was set to $U_{\text{bias}} = 80 \text{ V}$.

High voltage supply Three different voltage power supplies provide the high-voltages for the back plate, the front plate and the retarding electrode. A FUG HCN 140M-35000 that delivers up to 35 kV is connected to the back plate. The front plate voltage is provided by a FUG HCN 35M-5000 that is isolated up to 35 kV. It is connected to



(a) The high voltage supplies and the magnet power supplies can be seen in the rack at the left. The preamp is shielded with aluminum foil. For safety reasons (HV) the electron gun is placed in a high-voltage cage. (b) View of the electron gun flanged to the vacuum chamber. The e-gun magnet is aligned to the symmetry axis of the setup.

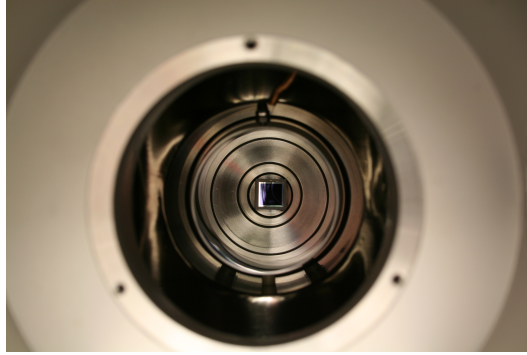
Figure 7.2: **View of the Münster test setup**

the 35 kV power supply and generates an offset voltage up to $\Delta U = 5$ kV. The retarding electrode voltage is supplied by a Knürr-Heinzinger PNC5 30000-5neg power supply that provides voltages up to 30 kV.

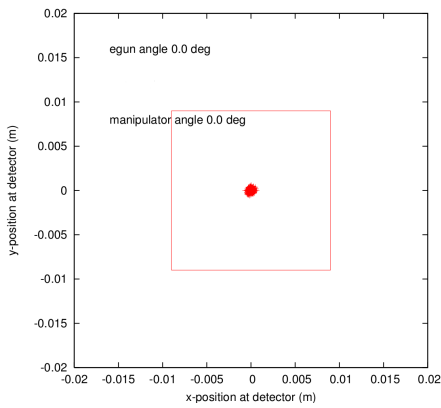
Magnets Two magnetic coils are used to provide the magnetic fields for the test setup. The detector magnet is a water-cooled coil with 120 copper-windings which can take a current up to $I_{\text{det}} = 120$ A (for short time intervals of a few minutes higher currents are possible) resulting in a field strength of $B_{\text{det}} \approx 0.1$ T. The electron gun magnet is an air coil that was used with currents up to $I_{\text{egun}} = 25$ A since it does not include water cooling. The maximum setting results in a magnetic field strength of $B_{\text{egun}} \approx 0.01$ T. The coils are powered by three Delta Elektronika power supplies (Type SM15-200D), whereas two are used for the detector coil.

Detector hit pattern In the Münster setup the relation between the two magnetic field strengths also determines the amount of electrons reaching the detector. This is also true for the electron gun angle α . Electrons reaching the detector are spatially distributed due to their different starting positions, energies and angles. The spatial distribution can directly be influenced by the relation between the two magnetic field strengths $\frac{B_{\text{egun}}}{B_{\text{det}}}$, the electron gun angle α and the acceleration potential ΔU . Because of the limited detector size in the measurements not all electrons are imaged onto the detector if the spatial distribution is too large or the electron beam is so far off the center that no electrons can reach the detector. This correlation could also be shown in the simulations by M. Zacher (fig. 7.3).

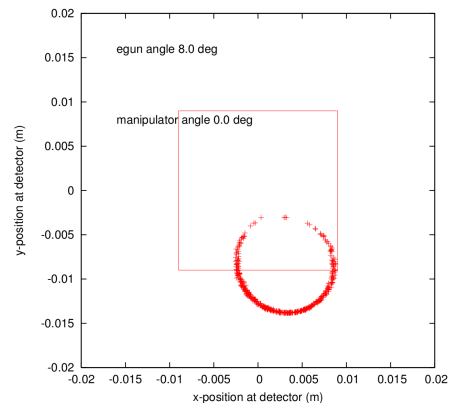
7 Electron gun test measurements



(a) Detector in the vacuum chamber.



(b) Hit pattern for $\alpha = 0^\circ$.



(c) Hit pattern for $\alpha = 8^\circ$.

Figure 7.3: **Detector and detector hit pattern for two different electron gun angles α :** The electron beam shows small spatial distribution and is fully imaged onto the detector for an electron angle of $\alpha = 0^\circ$ (b). For $\alpha = 8^\circ$ the electron beam shows a larger spatial distribution and has an offset relative to the detector. Only a fraction of the electrons is imaged onto the detector (c). [Zac13]

Hence if quantitatively comparable measurements are conducted it is crucial to use the same settings for U_{start} , ΔU , I_{egun} (magnet current for electron gun magnet) and I_{det} (magnet current for detector magnet) in each measurement.

7.2 Test measurements with front illuminated cathode

In the first test measurements the front illumination cathode method was used (as described in chapter 5.5). The tests included different cathode materials in order to evaluate the different achievable electron rates, as well as the energy spread by measuring the work functions of the tested materials. First transmission function test measurements were conducted to prove the angular selectivity of the electron gun. This section will

be divided into measurement types (e.g. electron rate measurements). The section will close with a discussion of the front illumination method in general.

7.2.1 Electron spectra

A typical electron spectrum shown with the corresponding fit is presented in figure 7.4. The detector counts electrons in dependence of the deposited energy. Each channel corresponds to a different energy. The graph consists of two electron peaks and the exponential background from electronics. The first peak is the single electron peak created by the deposited energy in the detector by single incident electrons. The second peak occurs when two electrons reach the detector in a very short time interval. Therefore the detector can not distinguish between the two signals and counts them as one with twice the energy deposited. This behavior is rate dependent and for higher rates peaks with three times and more of the single electron energy have been observed.

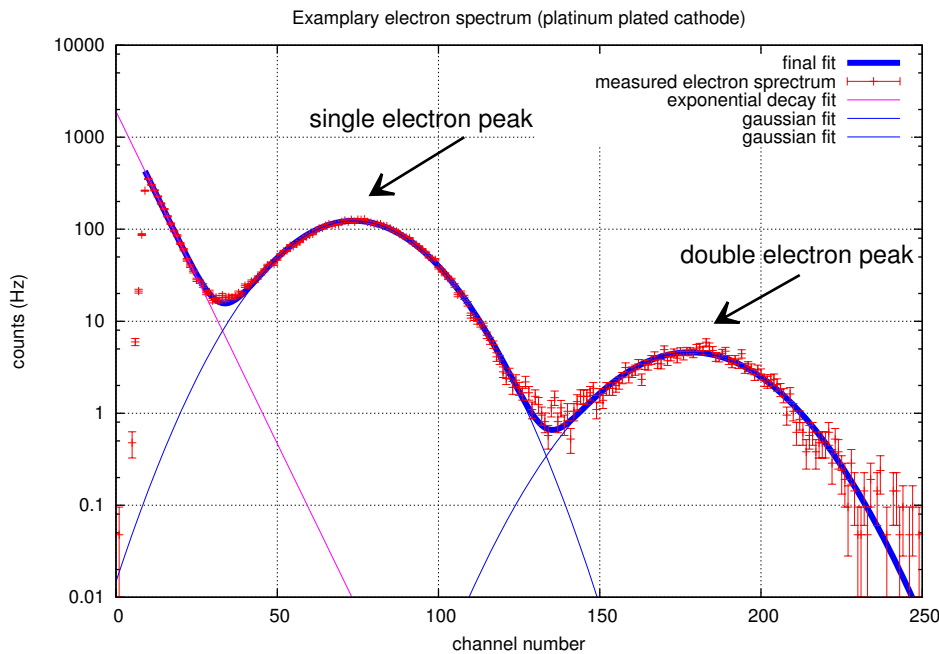


Figure 7.4: **Exemplary electron spectrum with fit:** The thin blue lines represent the Gaussian fits and the magenta line represents the exponential fit. The thick blue line is the final fit.

The data in the spectra first has to be deadtime corrected. The livetime and the realtime are logged by a software for the MCA-3 ADC called MCDWIN, so that the deadtime can be derived from these values. To extrapolate the electron rate the spectrum is fitted under the assumption that the electron energies are Gaussian distributed. In figure 7.4 the different parts of which the final fit is composed are also shown. The electron rate corresponds to the sum of the areas of the Gaussian fits, whereas the areas of the multi-electron peaks have to be multiplied with the amount of electrons detected

7 Electron gun test measurements

simultaneously (e.g. double electron peak \implies area * 2). The final fit is shown as the thick blue line in the figure. The electron spectrum fits in this thesis have been conducted with the software `fityk` (fit method: Levenberg-Marquardt algorithm).

In order to identify the electron energies for each channel an energy calibration is necessary. For that reason electron spectra for different U_{start} have been measured (fig. 7.5). Since U_{start} determines the total energy of the electrons, the linear fit of the data can be used to identify the corresponding energy for each channel. The energy calibration was conducted for every setup change that has been made in the development phase.

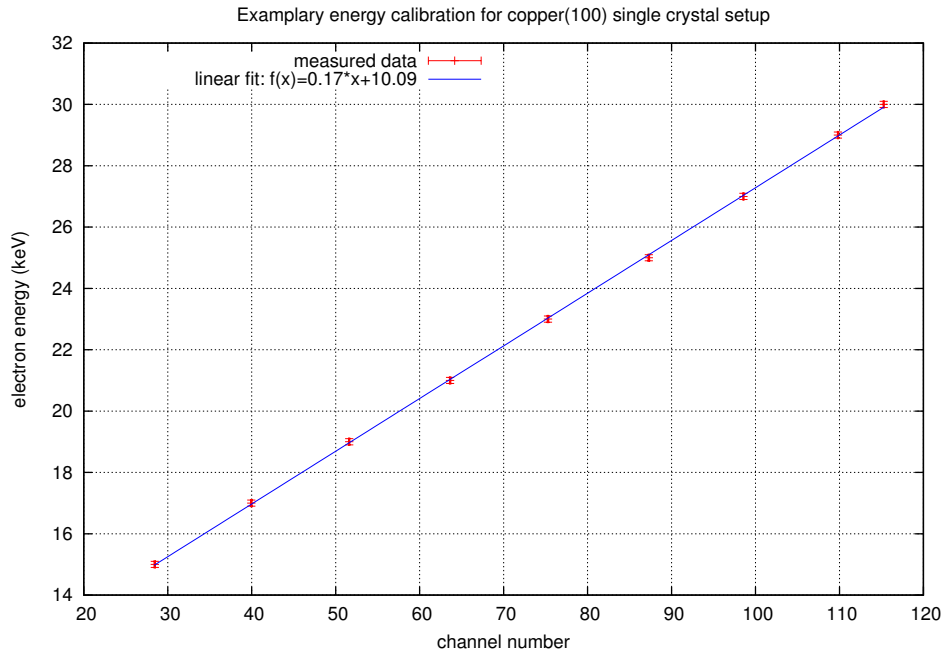


Figure 7.5: Exemplary energy calibration for the Cu(100) setup

7.2.2 Electron rate measurements

The first test measurements at Münster were conducted to prove that with the front illumination method, photoelectrons with sufficient rates of several kHz can be produced. Photoelectron production was tested for the Cu(100) single crystal, pure platinum, platinum plated stainless steel and gold plated stainless steel. All of the electron rate measurements in this section were conducted with the internal laser $\frac{\lambda}{2}$ -plate set to 30° (according to approx. 25% of the maximum output power for the particular laser setting). The settings for all the electron rate measurements in this section are shown in table 7.1.

For the copper single crystal the electron rates for different laser output powers were measured (fig. 7.6). The magnet current of the detector coil was set to $I_{\text{det}} = 120$ A. The e-gun coil was not yet implemented at that time. The maximum electron rate for

7.2 Test measurements with front illuminated cathode

U_{start}	ΔU	e-gun angle α	$\frac{\lambda}{2}$ -plate
-20 kV	5 kV	0°	30°

Table 7.1: **Electron gun settings for electron rate measurements in this section**

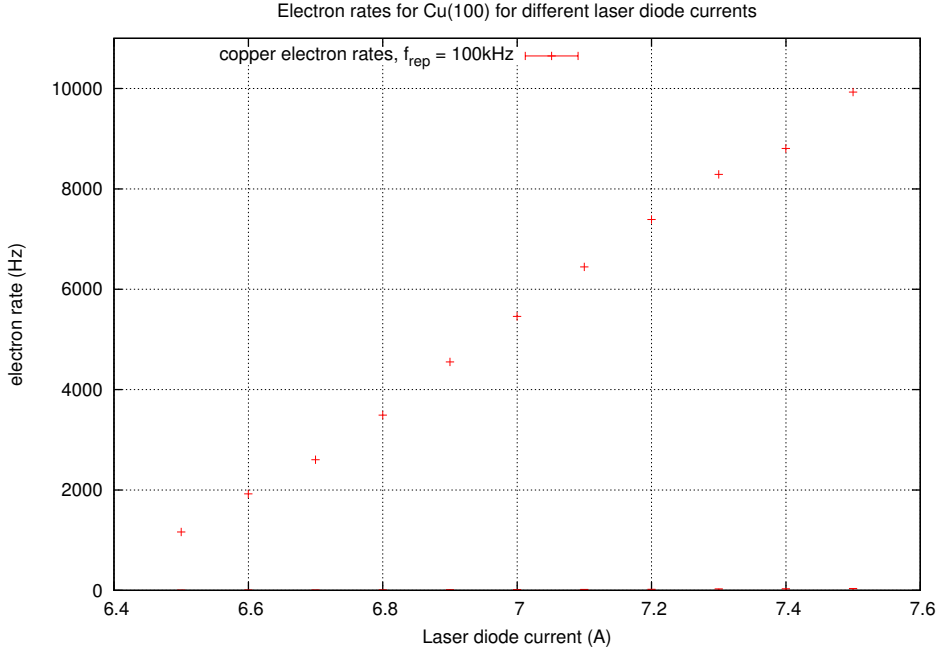


Figure 7.6: **Electron rates for the Cu(100) single crystal for varying laser diode currents**

8 A and 100 kHz is at approx. 10 kHz. Higher rates can be achieved with lower laser pulse repetition frequencies (f_{rep}) or by adjusting the $\frac{\lambda}{2}$ -plate to a higher transmission setting. Due to stray light reflections from the cathode material the electron signal is disturbed for higher output powers (see section 7.2.5).

For the metals gold and platinum no extensive rate measurements have been conducted. The measurements with these metals were conducted to show if photoelectrons can be produced despite their high literature work functions (Au = 5.1 eV; Pt = 5.64 eV). The produced rates can not be compared to the electron rates for copper since the magnetic field settings were different. The metals were tested because they were also tested as electrode coating metal. The measurements showed that photoelectrons can be produced with both metals (table 7.2). In consequence electrons can also be created on the surface of the electrodes.

7 Electron gun test measurements

Cathode material	Laser diode current I_{diode}	f_{rep}	detector coil current I_{det}	e-gun coil current I_{egun}	Electron rate
platinum plated stainless steel	6 A	100 kHz	120 A	25 A	1169 Hz
gold plated stainless steel	6.5 A	100 kHz	120 A	25 A	2315 Hz
pure platinum	6 A	100 kHz	100 A	25 A	1915 Hz
	6.5 A	100 kHz	100 A	25 A	3292 Hz

Table 7.2: Photoelectron rates for platinum and gold

7.2.3 Work function measurements

In conclusion of the electron rate measurements work function measurements for the copper single crystal and platinum plated steel have been conducted. A Hg-lamp was used in combination with the monochromator to scan through the UV spectrum up to a point where no photoelectrons are created. To determine the work functions the photoelectron yield in dependence of the wavelength has to be measured. The photoelectron yield can be derived by dividing the electron rate through the photon intensity. The resulting curve can be fitted based on the Fowler theory described in 5.3.2 (as proposed in [Ste12b]). The function used for the work function fits is equation (5.10) solved for the photoelectron yield.

$$I = e^{B + \ln f(\mu)} \cdot T^2 \quad (7.2)$$

With an approximate temperature $T \approx 291.15$ K and the known monochromator wavelength setting, the only free parameters in the function are the constant B and the work function W in $\mu = (h\nu - W)/k_{\text{B}}T$.

The spectrum of the lamp was measured with a photodiode (UV-035EQ). The optical setup as it was later used for monochromator calibration measurements is shown in figure 7.7. For the work function measurements in this section a similar assembly was used.

Directly after the photodiode measurements the fiber was mounted to the electron gun setup to measure the wavelength dependent electron rates. The electron gun settings for both electron rate measurements are shown in table 7.3.

U_{start}	ΔU	e-gun angle α	I_{det}	I_{egun}
-20 kV	5 kV	0°	120 A	25 A

Table 7.3: Electron gun settings for the work function measurements

The measured data and the fit results for both measurements with the copper single crystal and the platinum plated steel are presented in figures 7.8 and 7.9. With the

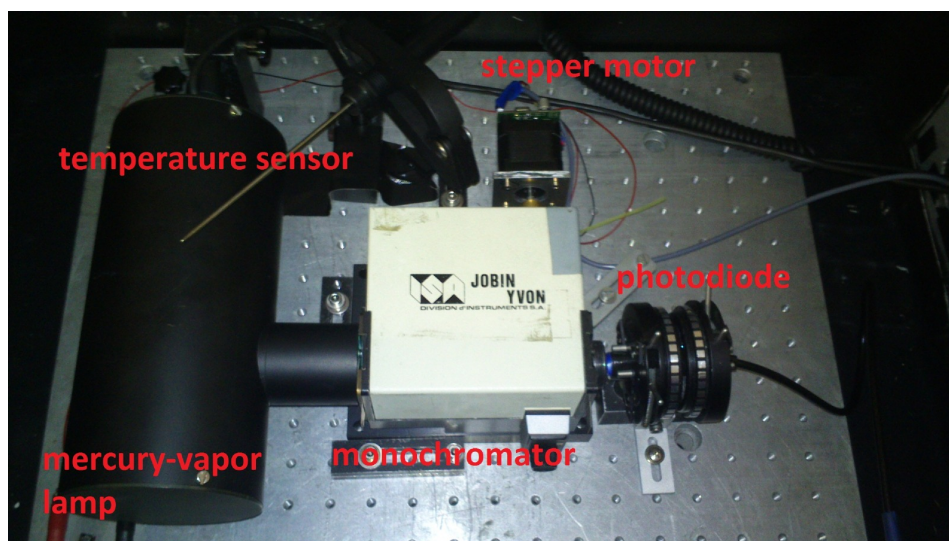


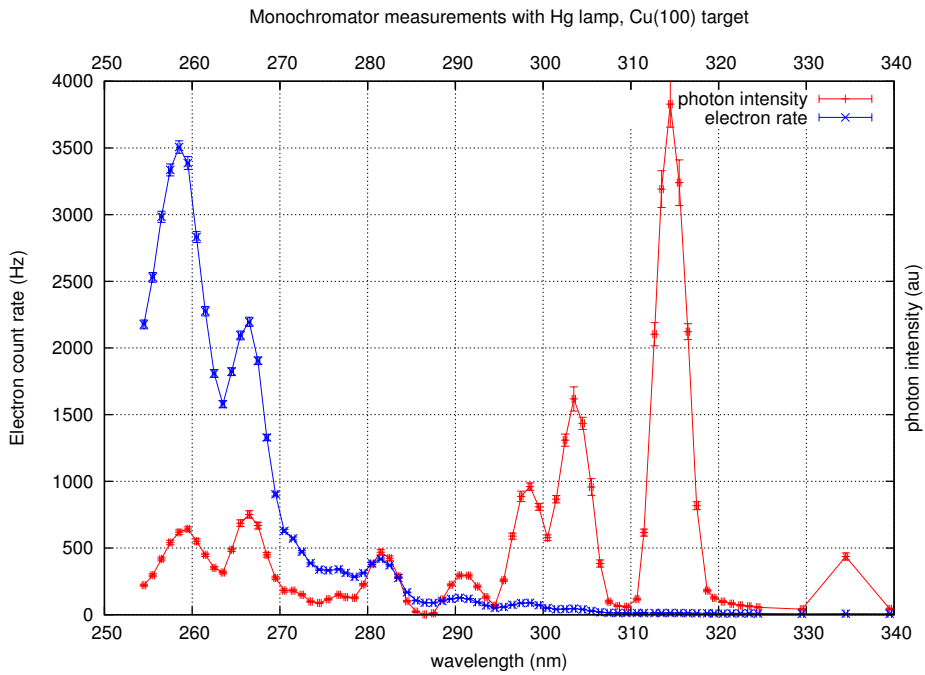
Figure 7.7: **Optical setup from monochromator calibration measurements:** For the work function measurements the casing for the Hg-lamp, the stepper motor and the temperature sensor were not used. (figure taken from [Pot13])

Fowler method the work function of Cu(100) and Pt could be determined to $W_{\text{Cu}} = (4.100 \pm 0.008) \text{ eV}$ and to $W_{\text{Pt}} = (4.082 \pm 0.006) \text{ eV}$.

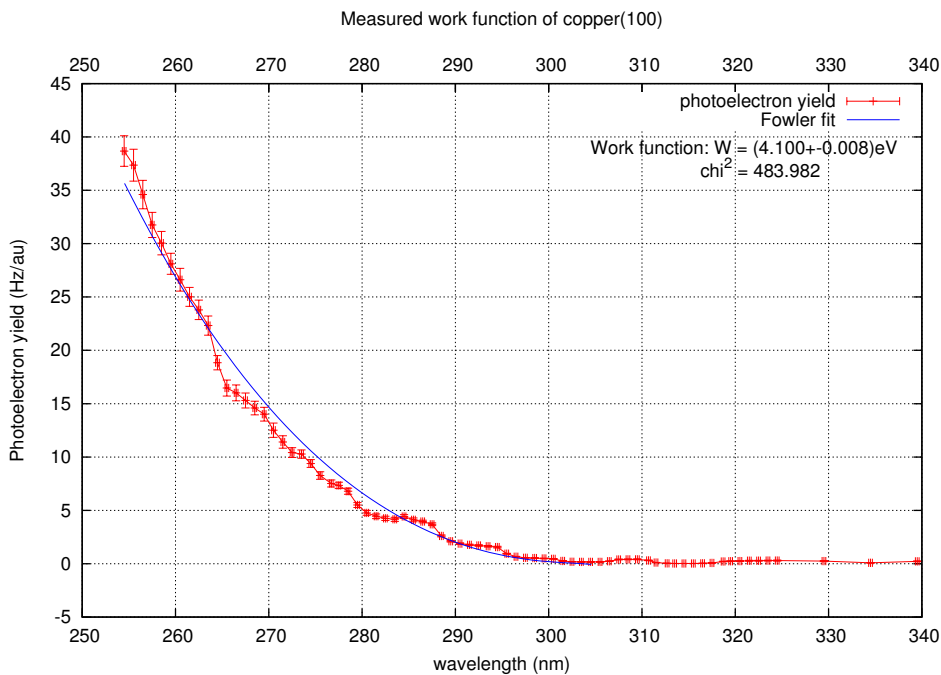
Both measurements show kinks in the photoelectron yields. The most probable cause for the kinks in the photoelectron yields is the temperature fluctuation of the Hg-lamp. At the time of the measurement no temperature sensor was applied. At later measurements it was shown that the intensity of the Hg peaks depends on the current temperature of the lamp. Since the photon intensity measurements and the electron rate measurements were not conducted simultaneously the temperature of the lamp could have been different for two corresponding measurements at the same wavelength setting.

In conclusion both metals showed large deviations from their literature work function values ($\Delta W_{\text{Cu}} = 0.49 \text{ eV}$ and $\Delta W_{\text{Pt}} = 1.56 \text{ eV}$). The work function is shifted towards lower energies. The shifts are most probably caused by adsorbates on the metal surfaces. Especially the work function shift for platinum is very large. A possible explanation for the large shift is that platinum is a very good catalyst and therefore more susceptible to surface alterations caused by adsorbates in comparison to other metals.

7 Electron gun test measurements



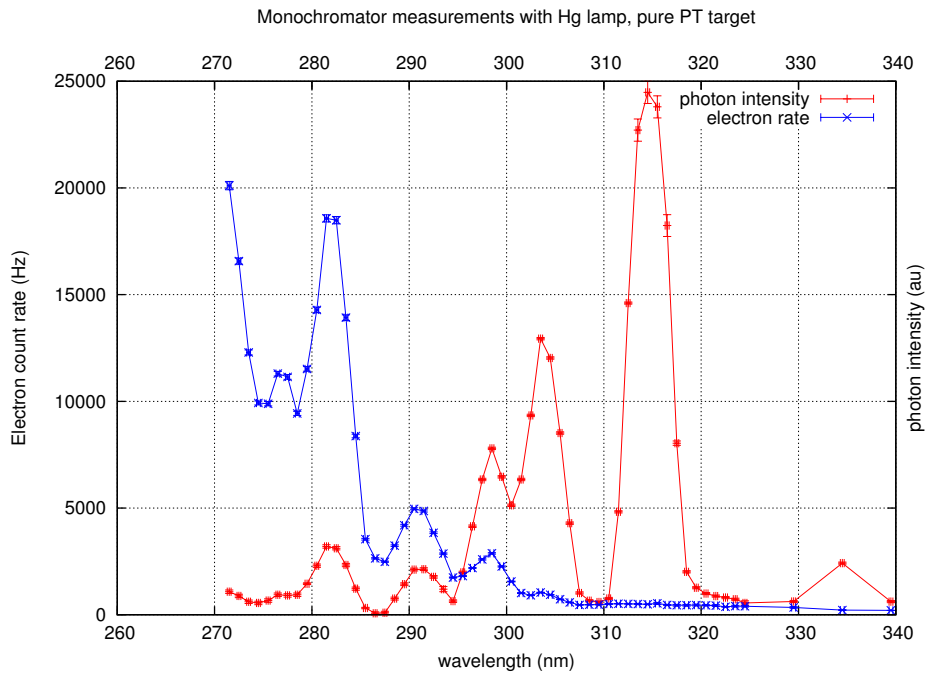
(a) Electron rate measurement (blue) with corresponding photon intensity measurement (red). The data points are connected for better visibility.



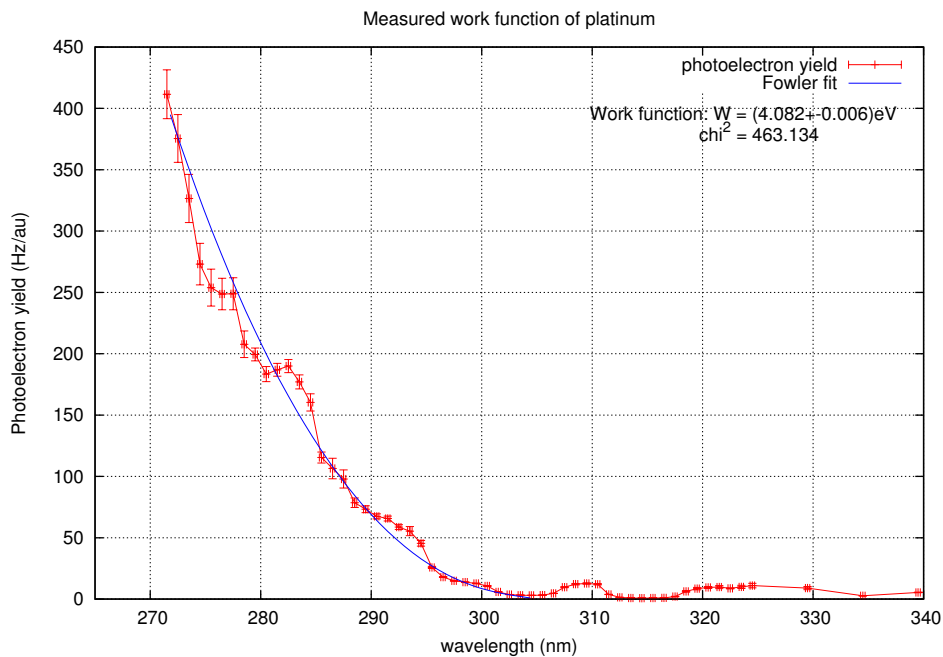
(b) Photoelectron yield with Fowler fit. The measured work function of the Cu(100) single crystal is $W_{\text{Cu}} = (4.100 \pm 0.008) \text{ eV}$

Figure 7.8: Work function measurement for Cu(100)

7.2 Test measurements with front illuminated cathode



(a) Electron rate measurement (blue) with corresponding photon intensity measurement (red). The data points are connected for better visibility.



(b) Photoelectron yield with Fowler fit. The measured work function of the Pt is $W_{\text{Pt}} = (4.082 \pm 0.006) \text{ eV}$

Figure 7.9: Work function measurement for Pt

7.2.4 Transmission function measurements

First transmission function tests have been conducted with pure Pt as cathode material. The settings for the measurements are shown in table 7.4. For the measurements

U_{start}	ΔU	I_{det}	I_{egun}	I_{diode}	f_{rep}
-15 kV	5 kV	120 A	25 A	6 A	100 kHz

Table 7.4: **Electron gun settings for the transmission function measurements with platinum**

the retarding potential U_{ret} was scanned from high voltages (no transmission) into full transmission. The transmission function for the electron gun angle $\alpha = 0^\circ$ is shown in figure 7.10. The transmission functions are fitted with a Gaussian error-function. The

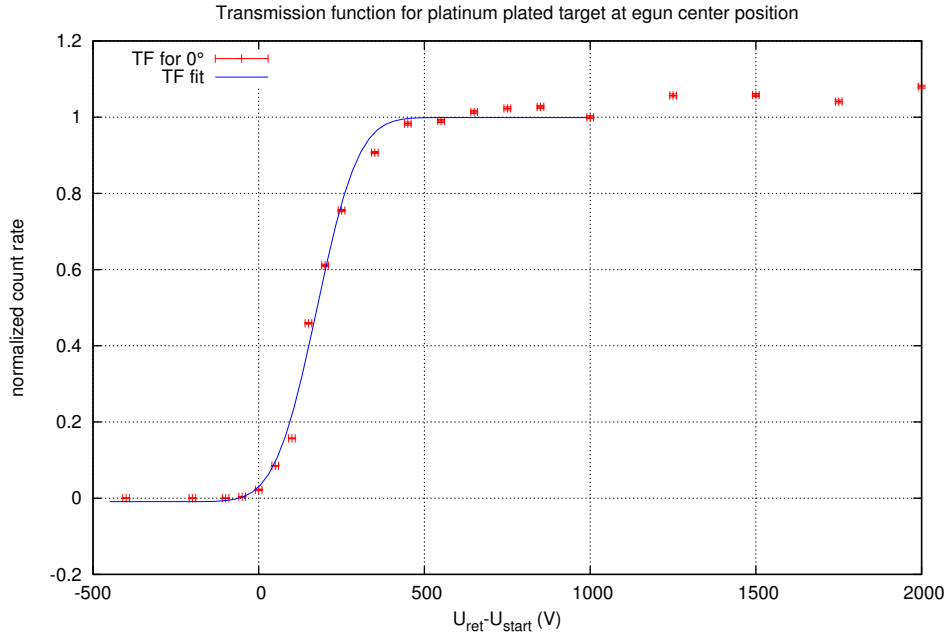


Figure 7.10: **Transmission function for $\alpha = 0^\circ$** : The transmission function width is $\sigma_E = (99.1 \pm 7.9)$ eV

error-function is a step function convoluted with a Gaussian and can describe transmission functions broadened by energy smearing. For all measurements the electron rate has been normalized for better comparability. The fit parameters are:

amplitude:	a
Gaussian width:	σ_E
position:	E_0
background (offset):	b

7.2 Test measurements with front illuminated cathode

The fit interval used for the fit in figure 7.10 limited to $[-500 \text{ V}; 1000 \text{ V}]$ since the electron rates for higher voltage differences showed oscillation which is a result of the detector hit pattern for angles $\alpha > 0^\circ$. The width of the transmission function for the center position is $\sigma_{\text{TM}} = (99.1 \pm 7.9) \text{ V}$ which is much broader than the expected transmission function width of $\sigma_{E,\text{sim}} = (1.1 \pm 0.1) \text{ V}$ for $\alpha = 0^\circ$ from simulations by M. Zacher. This difference can not alone be explained with the starting energy spread measured in the previous subsection which is approximately $\Delta E_{\text{start}} \approx 0.56 \text{ eV}$.

In figure 7.11 the transmission functions for different electron gun angles α are shown. The transmission functions widths for higher angles are larger than the width for $\alpha = 0^\circ$

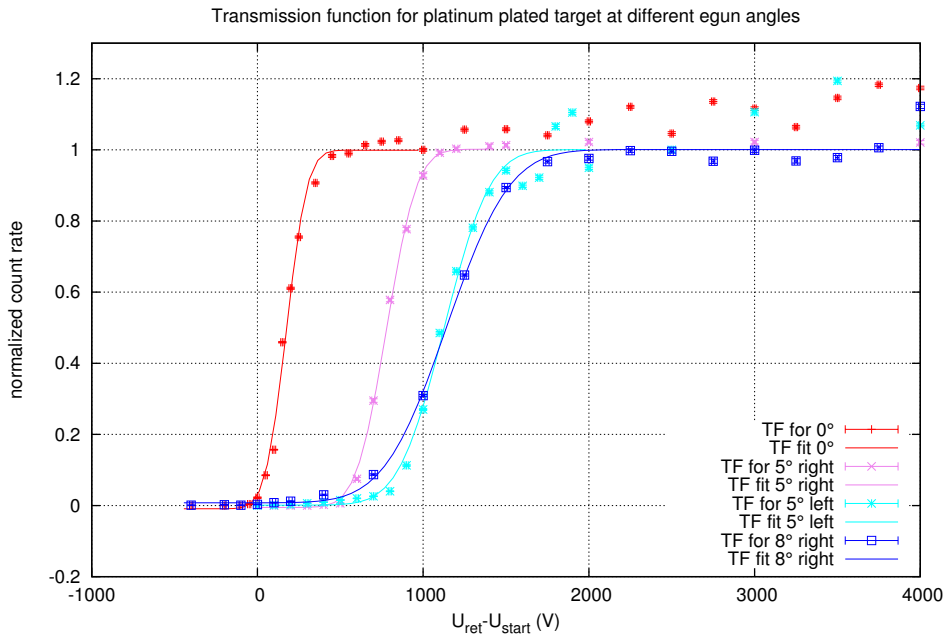


Figure 7.11: **Transmission functions for different electron gun angles α :** The transmission functions show that with the electron gun different angles θ_{ad} can be selected. Due to misalignments in the setup the $\pm 5^\circ$ transmission functions are not identical.

which was expected, since the angular spread of electrons becomes larger for larger angles α .

It is notable that for a perfectly aligned system the transmission functions for adjacent angles $\pm\alpha$ should be identical, which is not the case for the measured transmission functions (table 7.5). This indicates misalignments in the used setup. The center position of these measurements was determined by optically adjusting the e-gun chamber to the 0° position. The magnets were also only optically aligned at that time. Therefore the center position of the electron gun was not identical with the symmetry center position of the test setup. Another effect of the misalignment is the observed oscillation in the transmission signal for full transmission for the electron gun center position $\alpha = 0^\circ$. In a symmetric setup with an angle $\alpha = 0^\circ$ no oscillations should occur. Further details on

$\alpha (\pm 0.01^\circ)$	$\sigma_{\text{TM}} (V)$
0°	99.1 (8.0%)
$+5^\circ$	143.6 (4.1%)
$+8^\circ$	216.72 (10.2%)
-5°	298.6 (9.2%)

Table 7.5: **Transmission function widths for different electron gun angles α**

this topic will be presented in [Zac14]. The difference in width between measured and simulated transmission function for $\alpha = 0^\circ$ can also be explained with the misalignments. The assumed center position therefore has an angle $> 0^\circ$ relative to the magnetic field which then is expected to show a larger width compared to the real center position. Considering the high overlap of the transmission functions for $\alpha = -5^\circ$ and $\alpha = +8^\circ$, the real center is assumed to be at approx. $\alpha_c \approx +1.5^\circ$.

Despite the transmission functions being broader than expected, the angular selectivity could already be proven with the measurements presented. Each transmission function has a distinct position on the $U_{\text{ret}} - U_{\text{start}}$ scale and for higher angles α the transmission functions shift according to figure 4.2 which is a clear sign of angular selectivity.

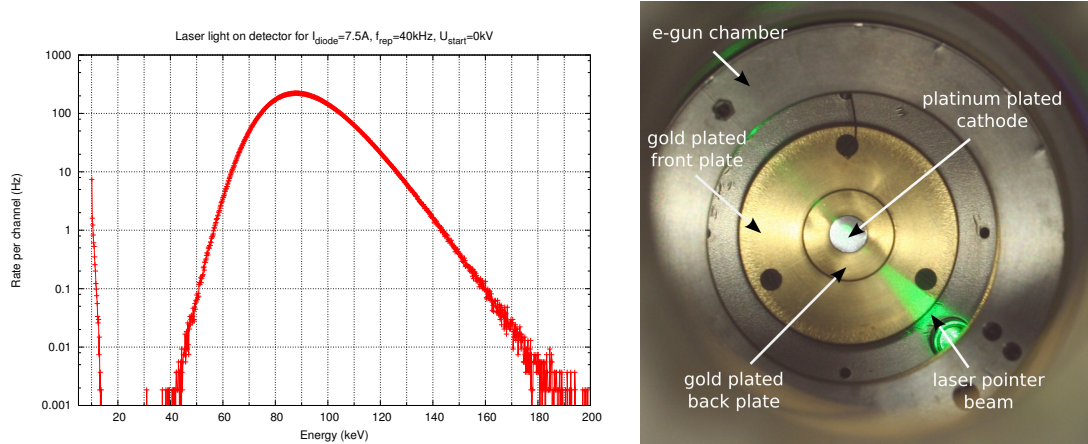
7.2.5 Stray light issues and conclusion

With the front illumination method stray light in the electron gun chamber was expected. All tested cathode materials are metals that reflect incident light. While a beam dump has been installed to absorb the specular reflected light, an unknown amount of light will still be reflected into the electron gun chamber due to diffuse reflection. This light could also be observed with the detector for high laser output powers (figure 7.12). For this measurement the electrodes were grounded so that no electrons could reach the detector. Then spectra with the laser turned on and turned off were compared. Hence the only possible signal source is the stray light in the chamber. When the setup was opened a test beam with a laser pointer was coupled into the fiber. The resulting stray light is shown in the same figure.

The stray light itself does not pose a problem for electron measurements at the main spectrometer, as it will only be detected for high output powers of the laser. Additionally the distance between detector and electron gun at the KATRIN main spectrometer are much larger, which lowers the impact of stray light on the detector signal even further.

The work function measurements showed that with metals that have much higher work function literature values than the laser energy photoelectrons could still be produced. For instance platinum and gold which were also used as electrode materials in the electron gun setup. Therefore stray light in the chamber produces photoelectrons from the electrodes. The spectrum in figure 7.13 a) shows clear evidence of an electron peak for electrons originating on the front plate. The peak can be distinguished from the back-plate peak due to the different electron energies. The energy difference is $\Delta E = 5 \text{ keV}$ which corresponds to the difference of the electrode potentials $\Delta U = 5 \text{ kV}$.

7.2 Test measurements with front illuminated cathode



(a) For high laser output powers (setting: $I_{\text{diode}} = 7.5\text{A}$, $f_{\text{rep}} = 40\text{kHz}$) stray light can be detected. The source can not be electrons since no high voltage was applied ($U_{\text{start}} = 0\text{kV}$, $\Delta U = 0\text{kV}$) (b) Front view of the electron gun in the vacuum chamber

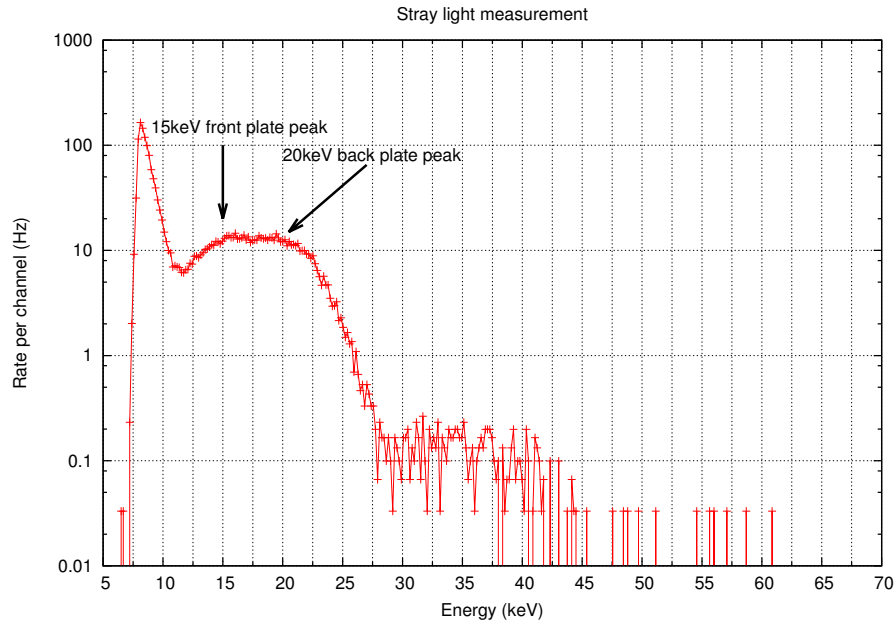
Figure 7.12: Laser stray light detection (left) and visible laser stray light (right)

The peaks could not be observed in the other spectra of the previous sections because different magnetic field settings have been used (fig. 7.13 b)). By changing the relation of the magnetic field strengths between the two magnets, different areas of the electrodes are imaged onto the detector. With the settings used in the previous measurements the front plate electrons did not get imaged onto the detector.

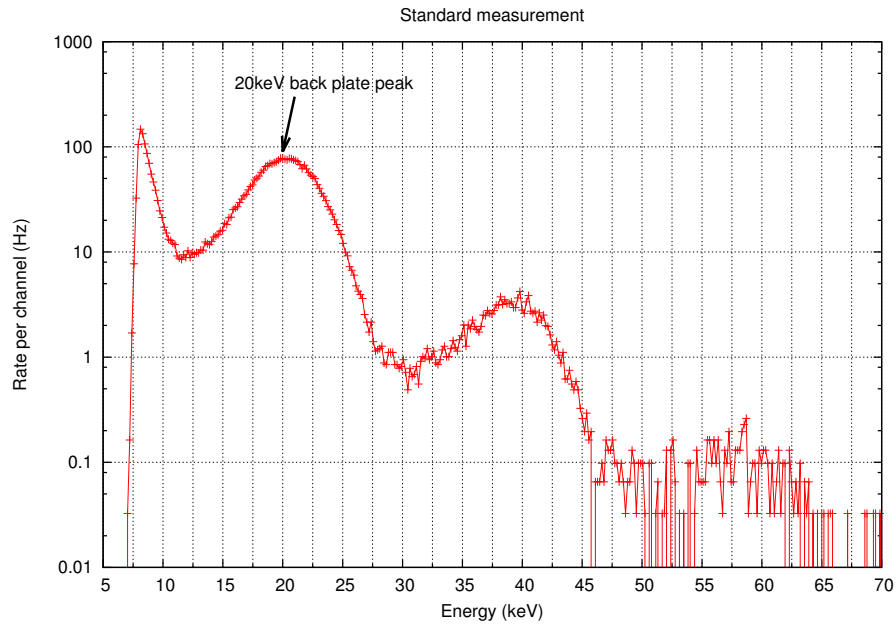
Front plate electrons are easily distinguishable from cathode electrons by the energy difference and would be reflected back into the chamber in transmission function measurements. This is not the case for electrons coming from the electrode material of the back plate. They gain the same energy as the electrons from the cathode material since they start on the same potential and thus can be transmitted in transmission function measurements. This leads to a much higher angular spread (starting point far from cathode center) and energy spread (different starting energy) of the measured electrons. Additionally the amount of angular spread is dependent on the electron gun orientation relative to the magnetic field, since different regions of the electrode are imaged onto the detector for different angles. These effects are very complex to consider in simulations which would be the only possibility to take the stray light effects into account in transmission function measurements.

In conclusion this illumination method had to be abandoned. No electrode material could be found that does not emit photoelectrons in the measurement conditions of the electron gun setup. Even with platinum which has the highest literature work function ($W = 5.64\text{eV}$) it was possible to create photoelectrons with the UV laser. As the final electrode material gold plated stainless steel was chosen.

7 Electron gun test measurements



(a) Spectrum settings $B_{\text{det}} = 40 \text{ A}$, $B_{\text{egun}} = 0 \text{ A}$, $U_{\text{back}} = 20 \text{ kV}$, $\Delta U = 5 \text{ kV}$ at e-gun center position. A 15 keV front plate peak can be observed.



(b) Spectrum for standard settings $B_{\text{det}} = 120 \text{ A}$, $B_{\text{egun}} = 25 \text{ A}$, $U_{\text{back}} = 20 \text{ kV}$, $\Delta U = 5 \text{ kV}$ at e-gun center position. No 15 keV front plate peak can be observed.

Figure 7.13: Detected stray light for e-gun angle $\alpha = 0^\circ$

7.3 Test measurements with back illuminated silver substrate

The first tests with a back illuminated silver evaporated fiber were conducted for a silver layer thickness of $d_{\text{Ag}} = 80$ nm. The layer proved to be too thick so that no photoelectrons could be produced. Therefore a fiber with a layer thickness of $d_{\text{Ag}} = 40$ nm has been prepared. All of the following measurements were conducted with this fiber. In conclusion to the transmission function measurements with the front illumination method, a much more precise alignment of the setup magnets has been conducted. Furthermore was the electron gun center position determined. The center position is the position where created photoelectrons have a minimum transverse energy component. The electron gun was set to a fixed value on the edge of the transmission function close to the setting of the assumed center position. Then the electron gun position was varied in an interval around this setting. The center position was then obtained by maximizing the electron rate on the detector.

7.3.1 Electron rate measurements

The achievable electron rates and the stability of the electron rates for the back illumination of silver are subject of this subsection. To extrapolate the maximum achievable rate the electron rates for different diode currents I_{diode} and a fixed repetition frequency $f_{\text{rep}} = 40$ kHz have been measured for a laser $\frac{\lambda}{2}$ -plate angle of 40° (corresponds to approx. 2% of the maximum power for the used laser settings). All of the fixed settings are presented in table 7.6. A direct measurement with the maximum output power was

U_{start}	ΔU	U_{ret}	I_{det}	I_{egun}	α	f_{rep}	$\frac{\lambda}{2}$ -plate
-20 kV	5 kV	0 kV	120 A	25 A	0°	100 kHz	40°

Table 7.6: **Electron gun settings for electron rate measurements with the silver vaporized fiber**

not possible since the detector can not handle the high resulting electron rates. Electron rates up to 100 kHz were achieved using these settings. Even higher rates are possible by varying the angle of the $\frac{\lambda}{2}$ -plate. However rates of up to 100 kHz are already sufficient for the purpose of a calibration source for the KATRIN main spectrometer.

Another subject of the electron rate measurements was to test the long term stability of the electron rate which directly depends on the fiber substrate integrity. Due to the negative potential on the backplate and the silver substrate, the surface of the silver is subject to bombardment by positive ions produced by ionization of restgas molecules in the vacuum chamber. This leads to a change in the thickness of the silver over time. Additionally the surface composition of the adsorbates on the silver surface changes over time after installing the electron gun in the vacuum chamber. At the beginning of a measurement phase the surface composition will still be dominated by adsorbates adsorbed under atmospheric conditions, whereas after some time in the vacuum chamber the surface composition will change. In order to investigate these effects, a standard

7 Electron gun test measurements

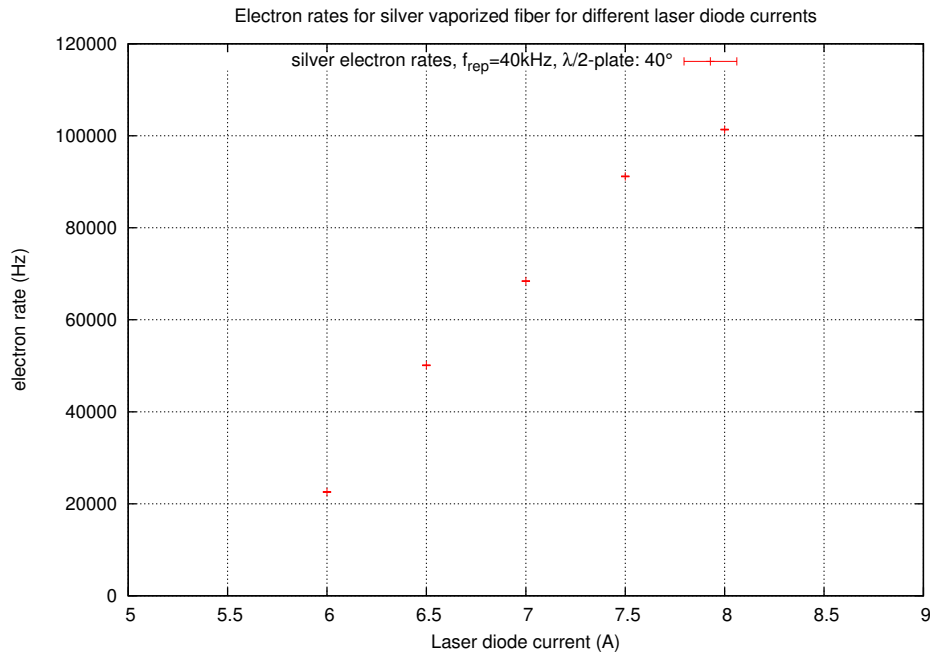


Figure 7.14: **Electron rate measurement with silver vaporized fiber:** A maximum rate of approx. 100 kHz can be achieved with $I_{\text{diode}} = 8$ A, $f_{\text{rep}} = 40$ kHz and $\frac{\lambda}{2}$ -plate set to 40° .

measurement has been conducted at the beginning of every measurement day. For every standard measurement the same electron gun settings were used to be able to compare the electron rates (table 7.7). It has to be noted that the standard runs were not

U_{start}	ΔU	U_{ret}	I_{det}	I_{egun}	I_{diode}	f_{rep}	$\frac{\lambda}{2}$ -plate	t
-20 kV	5 kV	0 kV	120 A	25 A	7 A	100 kHz	30°	60 s

Table 7.7: **Electron gun settings for the standard measurements**

conducted for the electron gun center position determined with the transmission function scan measurements for the reason that the center position was determined after the first standard runs were conducted. To keep the standard runs comparable, the electron gun position from the first standard runs was always used for these measurements. The rate change over 28 days is shown in figure 7.15. The effects described before can be seen in the progression of the electron rate. The first rate measured was (6264 ± 7) Hz at the first day of the measurement phase (after the pressure stabilized at about $p = 3 \cdot 10^{-7}$ mbar). After the second standard measurement on day two the setup was not used in a measurement downtime for 18 days. The first measurement after the downtime resulted in the maximum measured electron rate of (15762 ± 14) Hz for the standard measurements on day 20. The days after that the setup was in use almost every day. The rate drops with the resumption of the measurements to a rate of (6388 ± 7) Hz on the last day. It is not clear which of the effects described before is dominant for the rate

7.3 Test measurements with back illuminated silver substrate

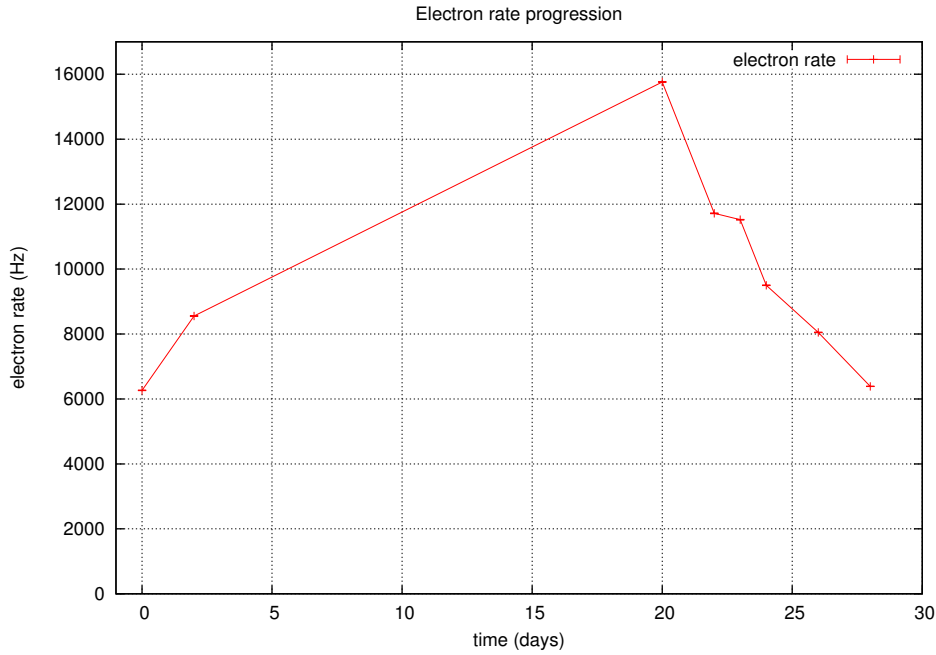


Figure 7.15: **Electron rate progression over the period of 28 days:** The electron rate shows a variation of more than 100 % with respect to the first measurements. The data points are connected for better visibility.

progression that was observed.

In conclusion it was proposed that standard measurements are to be conducted on a regular basis for the commissioning measurements at the KATRIN main spectrometer. Furthermore several fibers were prepared in order to have a replacement, if a fiber in the electron gun does not produce high enough electron rates anymore.

7.3.2 Work function measurements

The work function measurements for the silver fiber were conducted with two UV-LEDs (Roithner: UVTOP290 and UVTOP300) with nominal center wavelength of (295 ± 5) nm and (305 ± 5) nm. The settings for the measurements are shown in table 7.8.

U_{start}	ΔU	U_{ret}	I_{det}	I_{egun}	α	UVTOP290	UVTOP300
-20 kV	5 kV	0 kV	120 A	25 A	0°	$U = 6 \text{ V}, R = 267 \Omega$	$U = 6 \text{ V}, R = 267 \Omega$

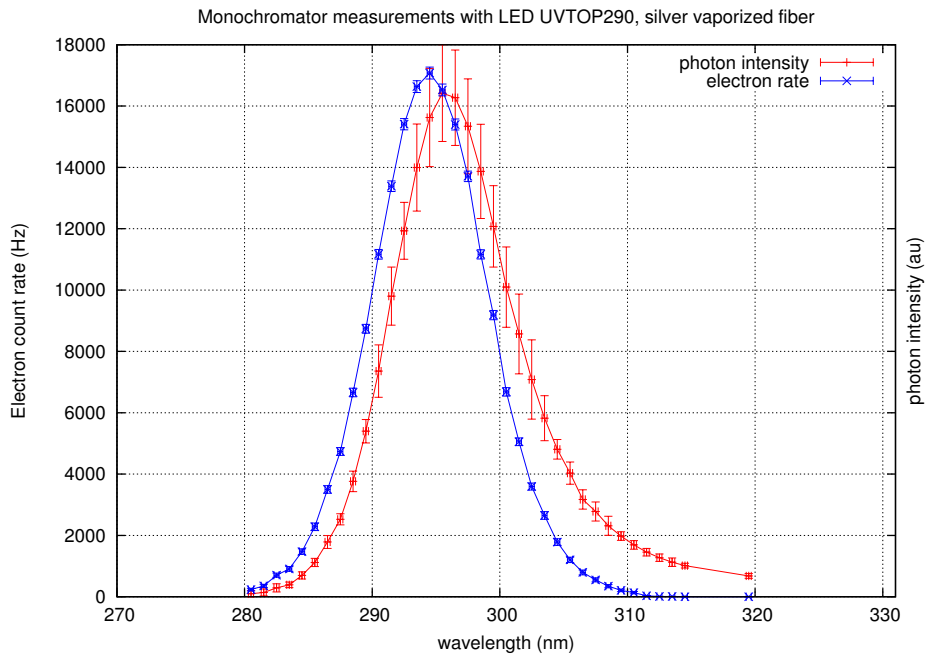
Table 7.8: **Electron gun settings for work function measurements with silver vaporized fiber**

For the measurements with the front illuminated setups the LEDs were not yet available. The LEDs have the advantage that they provide a stable intensity over the whole spectrum, whereas the Hg-lamp showed fluctuations in intensity due to the temperature

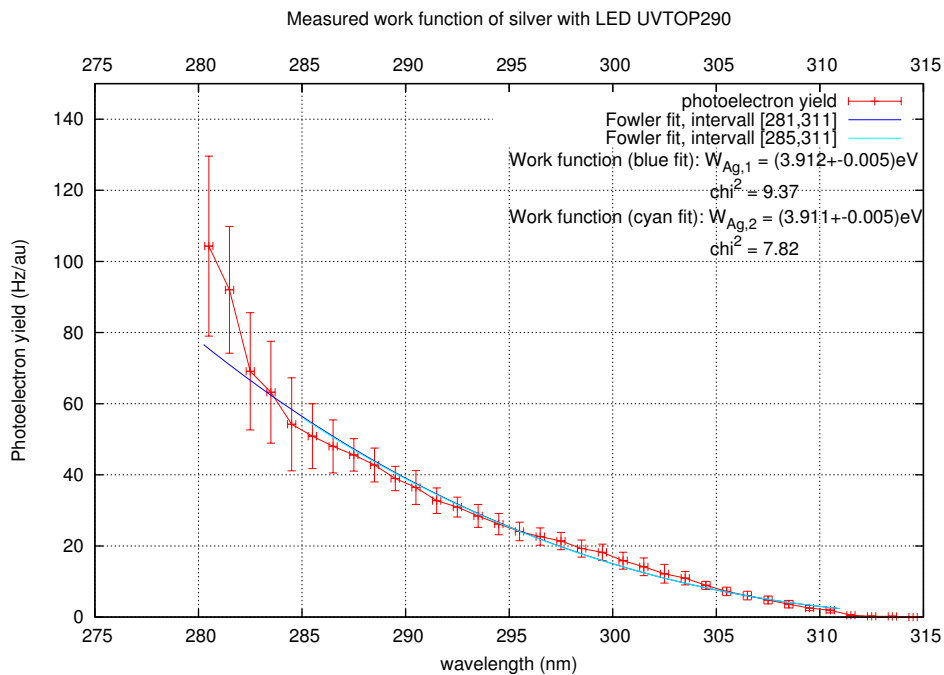
fluctuations. The measurement principle is the same as for the previous work function measurements. The LED intensity was measured first with a subsequent electron rate measurement. With the stable intensity of the LEDs the photoelectron yield did not show the kinks of the previous measurements. However the electron yield for low wavelengths and low photon intensities contains a large error. The measured values for low photon intensities are dominated by amplified noise fluctuations and are therefore not as reliable as the values for higher photon intensities. Hence two fits for each measurement were made. One fit with an interval from lowest measured wavelength up to the wavelength without electron signal and one fit that starts at a higher wavelength. Despite the two different fit intervals used in each measurement the two fits result in the same work function value for each measurement (figures 7.16 and 7.17).

However a work function difference of approx. $\Delta W \approx 0.1 \text{ eV}$ was observed between the two measurements. The measurements have not been conducted on the same day but on two consecutive days. With the laser standard measurements significant rate changes within a day have been observed, indicating that surface changes of the fiber in the time interval between the measurements could be the reason for the observed discrepancy. With this uncertainty the work function of the silver layer could only be determined to be in the region of $3.9 \text{ eV} - 4.0 \text{ eV}$. The maximum electron starting energy spread $\sigma_{E,\text{max}}$ for measurements with the silver vaporized fiber in combination with the laser is to be expected between $0.66 \text{ eV} - 0.76 \text{ eV}$.

7.3 Test measurements with back illuminated silver substrate



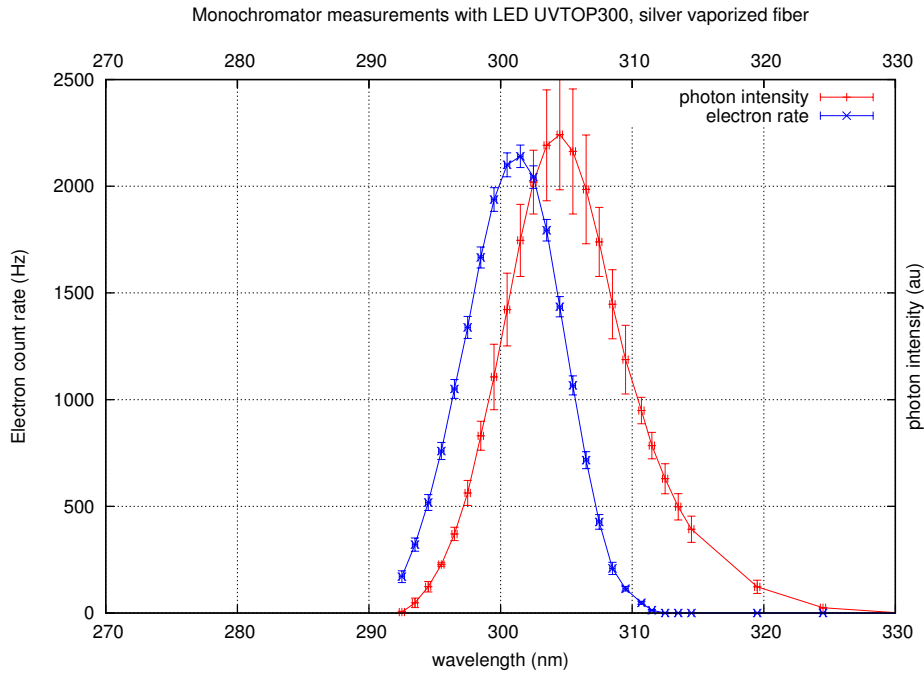
(a) Electron rate measurement (blue) with corresponding photon intensity measurement (red). The data points are connected for better visibility.



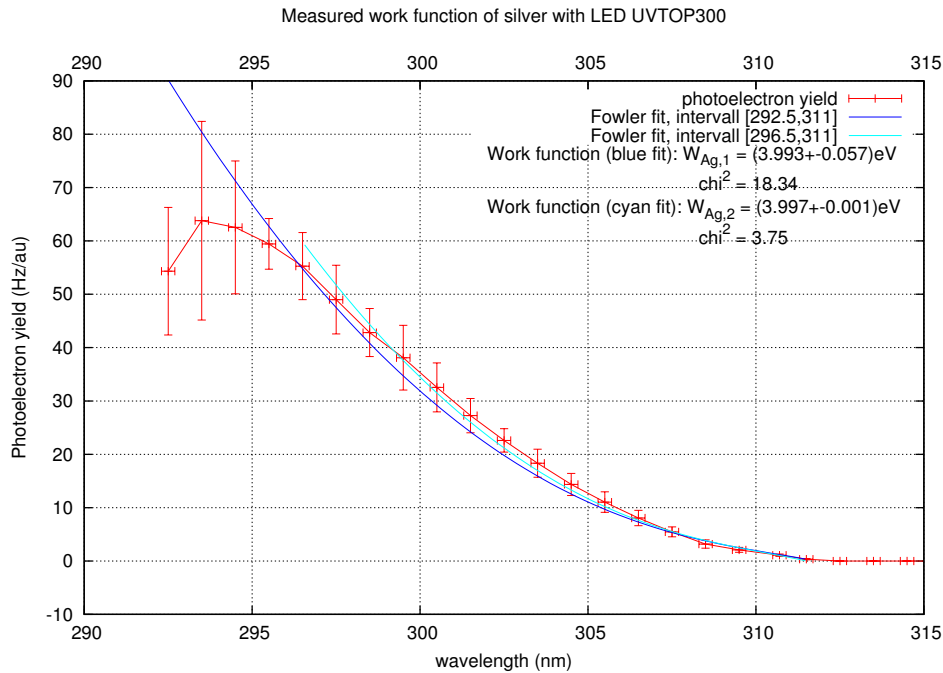
(b) Photoelectron yield with two Fowler fits for different intervals. The fit results for the work function are: $W_{Ag,1} = (3.912 \pm 0.005) \text{ eV}$ and $W_{Ag,2} = (3.911 \pm 0.005) \text{ eV}$

Figure 7.16: **Work function measurement for silver and LED UVTOP290**

7 Electron gun test measurements



(a) Electron rate measurement (blue) with corresponding photon intensity measurement (red). The data points are connected for better visibility.



(b) Photoelectron yield with two Fowler fits for different interval. The fit results for the work function are: $W_{Ag,1} = (3.993 \pm 0.003) \text{ eV}$ and $W_{Ag,2} = (3.997 \pm 0.001) \text{ eV}$

Figure 7.17: Work function measurement for silver and LED UVTOP300

7.3.3 Transmission function measurements

For the transmission function measurements with the silver evaporated fiber a much more precise alignment of the setup magnets has been conducted with the addition of determining the center position for the electron gun.

In consequence of the improved alignments a smaller transmission function width σ_E is to be expected for the center position. Only preliminary results of the transmission functions measured with the silver layer fiber are presented in this thesis, as the analysis conducted by M. Zacher was still in process at the time this thesis was finished. Figure 7.18 shows four transmission function measurement results with the preliminary fits provided by M. Zacher. The detailed analysis will be published as part of his doctoral thesis [Zac14].

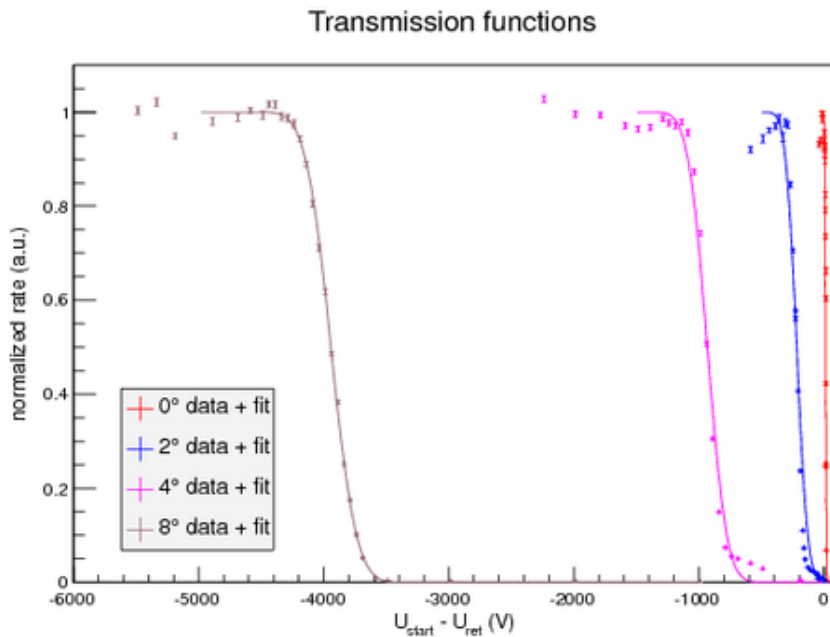


Figure 7.18: **Preliminary result of the transmission function measurements with the silver evaporated fiber:** Four selected transmission functions for different angles α are shown with their corresponding fits.

As a result of the electron gun center determination, the transmission function width σ_E for the electron gun center position $\alpha = 0^\circ$ is much smaller than in the platinum transmission function measurements. The shape of the transmission function proves that the electron gun also shows angular selectivity with the back illumination method.

7.3.4 Conclusion

In conclusion the electron gun with the back illumination method meets the requirements for a calibration source for the KATRIN main spectrometer. The rate capability of up

7 *Electron gun test measurements*

to 100 kHz is sufficient for the commissioning measurements.

The transmission function measurements for both investigated cathode materials (Pt and Ag) showed clear evidence of angular selectivity. It has to be noted that the transmission function measurements were limited to the presented angular range due to severe problems with the Attocube rotators. Under atmospheric conditions the rotators were able to rotate the electron gun chamber, while under vacuum conditions the rotators often got stuck and were then unable to move any further. Based on the slip stick motion principle described in chapter 5.4 the dynamic torque that the rotators can provide is dependent on the static friction between the guiding rod and the table. Under atmospheric conditions a small air buffer is always present between the guiding rod and the table, while this is not the case in high vacuum environments. Since the buffer is missing the static friction between rod and table becomes lower which causes the table to lose grip and thus can not be moved any further.

Therefore an alternative rotation mechanism had to be integrated in the electron gun setup before setting the electron gun up at the KATRIN main spectrometer. The new rotation mechanism uses an extension pin on the electrode assembly that is moved in two axes by linear motors through a vacuum feedthrough. The piezo rotators are still in place, used as a high precision readout.

In conclusion of the electron rate drift over time it is advised to conduct regular standard measurements to monitor the integrity of the silver surface.

8 Summary

A calibration source for the KATRIN main spectrometer has been successfully developed. After unsuccessful tests with a front-illuminated Cu(100) single crystal setup, the final setup with a back-illuminated silver layer evaporated onto a fiber has been tested.

For this setup configuration event rates up to 100 kHz have been measured at the test stand in Münster which is sufficient for the proposed main spectrometer commissioning measurements.

The energy distribution of the electron gun could not be measured at the test setup at Münster. Only an upper limit for the electron starting energy of $E_{\text{start}} = 0.76 \text{ eV}$ can be estimated as a result of the work function measurements for the final silver fiber setup.

Transmission function measurements proved the angular selectivity of the developed electron gun. However the piezo rotators often failed to move the electron gun under vacuum conditions which is why transmission function measurements were limited to one axis. Therefore a provisional rotation mechanism had to be applied to the electron gun before setting it up at KIT in order to be able to measure the transmission function of the main spectrometer for the full angular range.

After the test measurements at Münster with the final electron gun setup the electron gun was installed at the main spectrometer of the KATRIN experiment at KIT in preparation for the commissioning measurements (fig. 8.1). The electron gun was successfully flanged and aligned to the KATRIN main spectrometer as the final part for the work of this thesis.

First preliminary results of the commissioning measurements at the KATRIN main spectrometer indicate an energy distribution of $\sigma_E = 0.15 \text{ eV}$ for operation with the laser system. Using an UV LED in combination with the monochromator resulted in an energy distribution of $\sigma_E = 0.05 \text{ eV}$. Although the electron gun showed angular selectivity as expected, the transmission functions in addition showed a fraction of electrons with small emission angles even for high e-gun angles. This effect is currently under investigation and will be analyzed in the upcoming thesis of M. Zacher [Zac14].

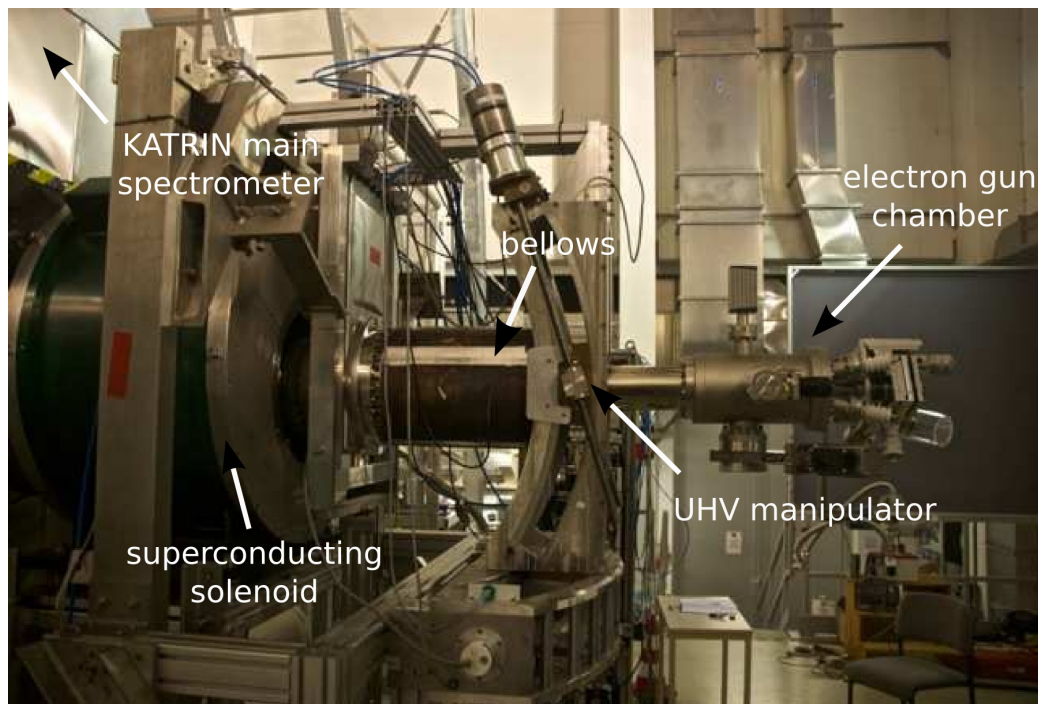


Figure 8.1: Final electron gun setup at KIT

A Monochromator Calibration

In order to calibrate the monochromator the Nd:YVO4-laser was used as standard with the precisely known wavelength of $\lambda = 266 \text{ nm}$. Therefore the laser light was coupled into the monochromator and the outgoing light intensity was measured by a photodiode in dependence of the wavelength setting of the monochromator. The measured data is shown in figure A.1. The center position of the peak deviates with $(5.5 \pm 0.2) \text{ nm}$ from the actual laser wavelength which had to be accounted for in the measurements. The spectral bandwidth of the monochromator could also be derived from this measurement and amounts to $\Delta\lambda = (4.1 \pm 0.2) \text{ nm}$ assuming the actual laser wavelength to have an approximate delta-distributed peak shape.

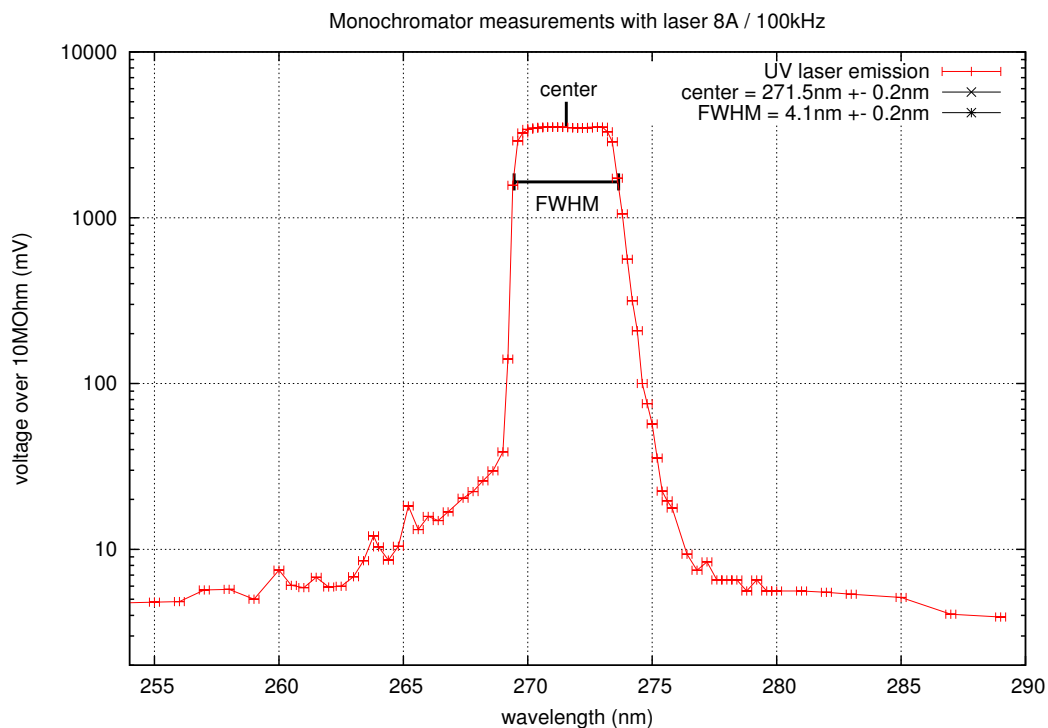



Figure A.1: **Monochromator calibration with the Nd:YVO4-laser:** The data points are connected for better visibility

B Data Sheets



UVTOP260

- Deep Ultraviolet Light Emission Source
- 265 nm, 150-300 μ W
- TO metal can with SiO₂ glass lens
-  Forensic Analysis, Disinfection



Description

UVTOP260 is a series of **AlGaIn** based deep UV-LEDs with a typical peak wavelength of **265nm** and optical output power of **150-300 μ W**. It comes in hermetically sealed TO39 or TO18 metal can package with ball lens, hemispherical lens, or flat glass window configuration. **UVTOP260** is widely used for forensic analysis, disinfection, optical sensing, and imaging applications

Maximum Ratings ($T_{CASE} = 25^{\circ}C$)

Parameter	Symbol	Values		Unit
		Min.	Max.	
Power Dissipation, DC	P_D		150	mW
Forward Current, DC	I_F		30	mA
Pulsed Current (1% duty cycle, 1kHz)	I_{FP}		200	mA
Reverse Voltage	U_R	-6		V
Operating Temperature	T_{opr}	-30	+55	$^{\circ}C$
Storage Temperature	T_{stg}	-30	+100	$^{\circ}C$
Soldering Temperature (max. 5s)	T_{sol}		+190	$^{\circ}C$

General Characteristics ($T_{CASE} = 25^{\circ}C$, $I_F = 20mA$)

Parameter	Symbol	Values			Unit
		Min.*	Typ.*	Max.*	
Peak Wavelength	λ_P	260	265	270	nm
Half Width (FWHM)	$\Delta\lambda$		12	15	nm
Forward Voltage	U_F		6.5	8.0	V

*wavelength measurement tolerance: ± 2 nm, forward voltage measurement tolerance: ± 2 %

Electro-Optical Characteristics ($T_{CASE} = 25^{\circ}C$, $I_F = 20mA$)

Part Number	Package	Window	Optical Power P_{OUT} (μ W)		View. Angle $2\theta_{1/2}$ ($^{\circ}$) Typ.
			Min.*	Typ.*	
UVTOP260-FW-TO39	TO-39	Flat Window	180	300	120
UVTOP260-TFW-TO39		Flat Window	80	150	120
UVTOP260-TFWR-TO39		Flat Window	120	200	120
UVTOP260-HL-TO39		Hemisp. Lens	120	250	7
UVTOP260-BL-TO39		Ball Lens	180	300	7
UVTOP260-FW-TO18	TO-18	Flat Window	150	250	120
UVTOP260-BL-TO18		Ball Lens	150	250	10

*output power measurement tolerance: ± 10 %

 **Open Can version (TO18 or TO39, no cap, no window) available on request**

Optran® UV, Optran® WF

(Silica/Silica Fiber with Optional Buffers)



CeramOptec's® high quality Optran UV and Optran WF fiber exhibits exceptional performance and transmission from the deep UV to the IR. With a wide range of core sizes and NA's, Optran UV and Optran WF are ideal for applications including spectroscopy, medical diagnostics and devices, laser delivery and instrumentation. We offer a variety of jacket types – as well as custom-designed products and sizes to meet your specifications.

Features

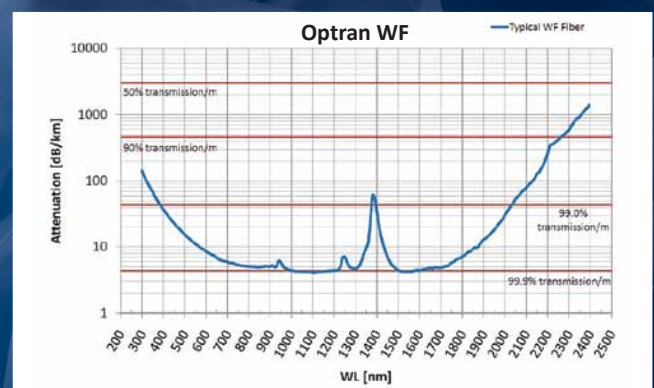
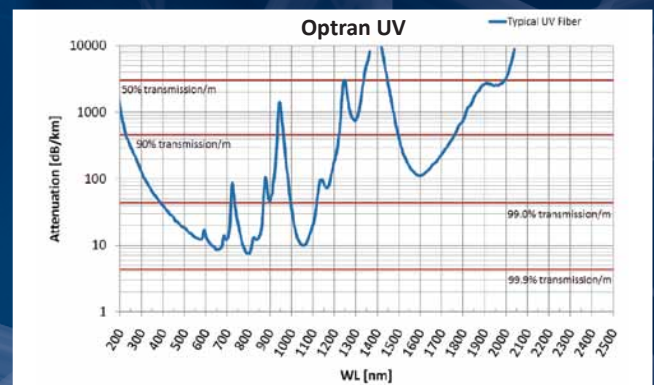
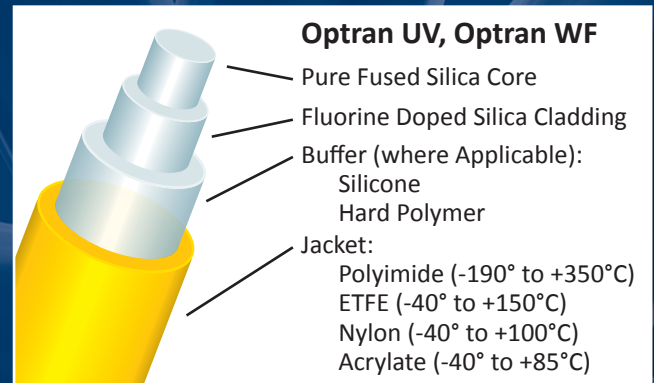
- Broad UV / VIS / NIR spectral range
Optran UV: 190 – 1200 nm
Optran WF: 300 – 2400 nm
- High laser damage resistance
- Broad temperature range (-190° to +350°C)
- Core diameters available from 50 µm to 2000 µm
- Specialty coatings available for high temperatures, high vacuum and harsh chemicals
- Superior Focal Ratio Degradation Characteristics
- Biocompatible materials
- Sterilizable by ETO and other methods
- Manufactured at GMP and ISO 9001 compliant facility
- RoHS compliant

Properties

- Step index profile
- Pure synthetic fused silica core
Optran UV: high OH- content > 700 ppm
Optran WF: low OH- content < 1 ppm
OH- content < 0.25 ppm and < 0.1 ppm available upon request
- Available NA:
Low NA: 0.12 ± 0.02
Standard NA: 0.22 ± 0.02
High NA: 0.30 ± 0.02 (Optran Plus®)
- Standard proof test:
100 kpsi (Nylon, ETFE, Acrylate jackets)
70 kpsi (Polyimide jacket)
- Core/clad ratios available:
1:1.04, 1:1.06, 1:1.1, 1:1.15, 1:1.2, 1:1.25, 1:1.4
- Minimum bend radius:
50 x clad diameter (momentary mechanical stress)
150 x clad diameter (during usage with high laser powers)

Note

CeramOptec strives to ensure the accuracy of all information provided; however, we imply no warranties and disclaim any liability in connection with the use of this information.



Contact us:

North America

CeramOptec Industries, Inc. Phone: 800-934-2377
515A Shaker Rd. 413-525-0600
East Longmeadow, MA 01028 Fax: 413-525-1112
Email: salesengineering@ceramoptec.com

Europe

CeramOptec GmbH Tel.: +49-228-97967-0
Siemensstrasse 44 Fax: +49-228-97967-99
53121 Bonn Email: info@ceramoptec.de
Germany

Please visit www.ceramoptec.com for more information.

CeramOptec is a registered trademark of biolitec group. Optran is a registered trademark of biolitec group. Optran Plus is a registered trademark of biolitec group. CeramOptec GmbH is a subsidiary of biolitec AG. For more information please visit www.biolitec.com



H10 series Monochromators

A Compact 10 cm Monochromator

In spite of its small size, the H10 monochromator offers performances equal to those of more sophisticated instruments. The H10 monochromator is a versatile and low cost device that can be used in several applications such as lower resolution transmission/absorption and fluorescence or as a variable filter, for selecting a range of wavelengths from continuous light source.

An Unique Optical Configuration

The H10 series Monochromators are built around an aberration-corrected concave holographic diffraction grating. This element plays a triple role: collimating, dispersing and focusing functions.

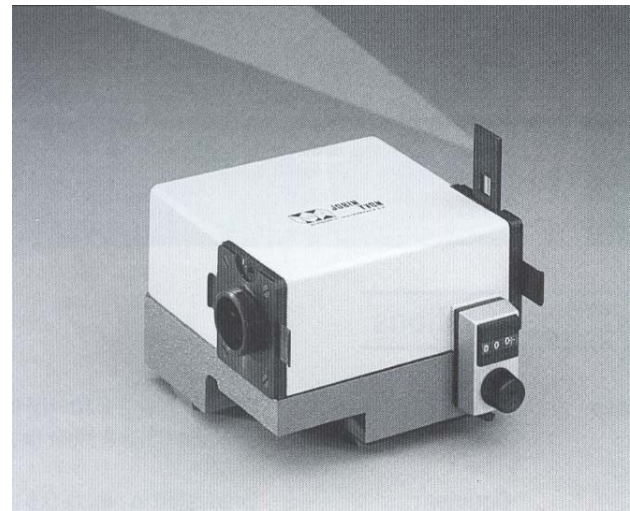
This optical design minimizes the number of optics for a higher throughput and offers a unique On-Axis entrance/exit port configuration.

The H10 features High Spectral Purity: High stray light level rejection of 10^{-5} at 8 nm from 632.8 nm laser line with a 1200 gr/mm grating.

A manual mechanical wavelength counter (motorization with RS232 or IEEE interface in option) and manual slits make the H10 extremely easy to use.

Several interchangeable fixed width slit inserts are available. Each slit is supplied with a height limiter (continuously adjustable from 1 to 8 mm).

With its M28 thread attachment, the H10 can be easily equipped with a full range of accessories including light sources, detectors, fiber adapters, filter wheels and choppers.



H10 Monochromator

Specifications

Focal length	100 mm
Aperture	f/3.5
Resolution	Typically 1nm at 500 nm with 0.1 mm slit, 1200 gr/mm grating
Stray light	10 E-5 at 8 bandpass from 632.8 nm laser line
Wavelength counter	Digital, direct reading in nm with 1200 gr/mm grating, graduated in 0.2 nm intervals
Reproducibility	+/- 0.25 nm with 1200 gr/mm grating
Entrance/Exit slits	Fixed: 0.5, 1, 2 mm; other sizes available as options

Available Models

Model	Spectral range	Dispersion	Grating groove density
H10 UV	200 – 750 nm	8 nm/mm	1200 gr/mm
H10 Vis	350 – 800 nm	8 nm/mm	1200 gr/mm
H10 IR	400 – 1600 nm	16 nm/mm	600 gr/mm

Features

- Only Three internal optics
- On-Axis port configuration
- Fully Manual (Optional motorized drive)
- Low cost
- Compact and Robust

In the USA:

Jobin Yvon Inc
3880 Park Ave,
Edison, New Jersey,
08820 USA
Tel: (732)-494-8660
Fax: (732)-549-9309
Email: OSD@jyhoriba.com

In France:

Jobin Yvon SA
16-18 rue du Canal
91165 Longjumeau cedex
France
Tel: (33) (0) 1 64.54.13.00
Fax: (33) (0) 1 69.09.93.19

1-877-JYHoriba

China: 86-10-68313388
Germany: 89/46.23.17-0
Italy: 2/57.60.30.50
Japan: (81)3-5823-0140
U.K.: 020-8204-8142

PIN : OSD-0017 REV.A

Bibliography

- [And59] P. A. Anderson et al., *Work function of gold*. Phys. Rev., 115:553 554 (1959)
- [Arl09] H. Arlinghaus, *Diploma thesis*, Institut für Kernphysik, Westfälische Wilhelms-Universität Münster (2009)
- [Ash13] N. W. Ashcroft, D. N. Mermin, *Festkörperphysik*, Oldenbourg Verlag, 4. Auflage (2013)
- [Att] Attocube GmbH, www.attocube.com
- [Avi07] F.T. Avignone III et al., *Double Beta Decay, Majorana Neutrinos, and Neutrino Mass*, arxiv:0708.1033v2 [nucl-ex] (2007)
- [Bec13] M. Beck et al., *An angular selective electron source for the KATRIN experiment*, to be published (2012)
- [Beh12] J. Behrens, *Diploma thesis*, Institut für Kernphysik, Westfälische Wilhelms-Universität Münster (2012)
- [Bok13] K. A. Bokeloh, *PhD thesis*, Westfälische Wilhelms-Universität Münster (2013)
- [Che82] M. Chelvayohan et al., *Work function measurements on (110), (100) and (111) surfaces of silver*. J. Phys. C, 15:23052312 (1982)
- [Cer] www.ceramoptec.com
- [Eas17] D. E. Eastman, *Photoelectric Work Functions of Transition, Rare- Earth, and Noble Metals*. Phys. Rev. B **2** (1970)
- [Fer34] E. Fermi, Z. Phys. 88 (1934) 161 - 177
- [Fow31] R. H. Fowler, *The analysis of photoelectric sensitivity curves for clean metals at various temperatures*, Phys. Rev. **38**, 45 (1931)
- [Hei10] J. H. Hein, *Diploma thesis*, Westfälische Wilhelms-Universität Münster (2010)
- [Hen94] M. Henzler and W. Göpel, *Oberflächenphysik des Festkörpers*, B. G. Teubner. 2. Auflage, (1994)
- [Hub66] E. E. Huber et al., *The effect of mercury contamination on the work function of gold*. Appl. Phys. Lett., **8**:169171 (1966)
- [Hug08] K. A. Hugenberg, *Diploma thesis*, Westfälische Wilhelms-Universität Münster (2008)
- [Jos13] L. Josten, *Bachelor thesis*, Westfälische Wilhelms-Universität Münster (2013)

Bibliography

- [Kam] The Super-Kamiokande Collaboration, Evidence for oscillation of atmospheric neutrinos, *Phys. Rev. Lett.* **81** 1562-1567 (1998)
- [KAT] The KATRIN homepage, <http://www.katrin.kit.edu/>
- [KAT04] The KATRIN collaboration, *KATRIN Design Report 2004*, FZKA Scientific Report 7090
- [KAT06] Komitee für Astroteilchenphysik (KAT), *Kosmische Spurensuche - Astroteilchenphysik in Deutschland* (2006)
- [Les06] J. Lesgourgues and S. Pastor, *Massive neutrinos and cosmology*, *Phys. Rep.* **429** (2006) 307
- [Nak10] K. Nakamura et al., *Review of Particle Physics*, *Journal of Physics G* **37**: 1. (2010)
- [Pau30] W. Pauli, *Collected Scientific Papers*, Eds. Kronig & Weisskopf, Vol. 2, 1316–1317
- [Pic92] A. Picard, *A solenoid retarding spectrometer with high resolution and transmission for keV electrons*. *Nuc. Instr. Meth. B* **63**, 3:345.358 (1992)
- [Pot13] A. Potthoff, *Bachelor thesis*, Institut für Kernphysik, Westfälische Wilhelms-Universität Münster (2013)
- [Rab97] S. Raby and R. Slansky, *Neutrino Masses: How to add them to the Standard Model*, Los Alamos Science No. 25 (1997)
- [Rei59] R. Reines & C.L. Cowan, *Free Antineutrino Absorption Cross Section. I. Measurement of the Free Antineutrino Absorption Cross Section by Protons*, *Phys. Rev.* **113**, 273 (1959), doi:10.1103/PhysRev.113.273
- [She92] C.S. Shern, *Changes in Work Function of Hydrogen and Oxygen Adsorption on Pt(110) Surface Measured by Mirror Electron Microscope-LEED*, *Chinese Journal of Physics*, Vol. 30, No. 6, 841-850 (1992)
- [Ste12a] N. Steinbrink, *Diploma thesis*, Institut für Kernphysik, Westfälische Wilhelms-Universität Münster (2012)
- [Ste12b] N. Steinbrink, *Internal group meeting* (2012)
- [Val04] K. Valerius, *Diploma thesis*, Institut für Kernphysik, Westfälische Wilhelms-Universität Münster (2004)
- [Val09] K. Valerius, *PhD thesis*, Institut für Kernphysik, Westfälische Wilhelms-Universität Münster (2009)
- [Vöc08] S. Vöcking, *Diploma thesis*, Institut für Kernphysik, Wilhelms-Universität Münster (2008)
- [Wal09] S. G. Walton et al., *Low energy, ion-induced electron and ion emission from stainless steel: The effect of oxygen coverage and the implications for discharge modelling*. *J. Appl. Phys.* **85**:1832 (1999)

- [Wig12] The WiggleZ Dark Energy Survey, *Cosmological neutrino mass constraint from blue-redshift galaxies*, Phys. Rev. D **85**:081101 (2012)
- [Wea81] R. C. Weast, editor. *Handbook of Chemistry and Physics*. CRC Press (1981)
- [Wik] en.wikipedia.org
- [Wol08] I. Wolff, *Diploma thesis*, Institut für Kernphysik, Westfälische Wilhelms-Universität Münster (2008)
- [Zac09] M. Zacher, *Diploma thesis*, Institut für Kernphysik, Westfälische Wilhelms-Universität Münster (2009)
- [Zac13] M. Zacher, *Electron gun tests and characteristics*, 24th KATRIN collaboration meeting (2013)
- [Zac14] M. Zacher, *PhD thesis*, Institut für Kernphysik, Westfälische Wilhelms-Universität Münster, to be published
- [Zub04] K. Zuber, Neutrino Physics Institute of Physics Publishing Bristol and Philadelphia, 2004